

1

UNIVERSITY OF BRISTOL

2

DOCTORAL THESIS

3

4

Investigating, implementing, and creating methods for analysing large neuronal ensembles

5

6

Author:

Thomas J. DELANEY

Supervisors:

Dr. Cian O'DONNELL

Dr. Michael C. ASHBY

9

*A thesis submitted in fulfillment of the requirements
for the degree of Doctor of Philosophy*

10

in the

11

Biological Intelligence & Machine Learning Unit
Department of Computer Science

12

July 5, 2020

¹⁵ Declaration of Authorship

¹⁶ I, Thomas J. DELANEY, declare that this thesis titled, "Investigating, implementing, and
¹⁷ creating methods for analysing large neuronal ensembles" and the work presented in it are
¹⁸ my own. I confirm that:

- ¹⁹ • This work was done wholly or mainly while in candidature for a research degree at this
²⁰ University.
- ²¹ • Where any part of this thesis has previously been submitted for a degree or any other
²² qualification at this University or any other institution, this has been clearly stated.
- ²³ • Where I have consulted the published work of others, this is always clearly attributed.
- ²⁴ • Where I have quoted from the work of others, the source is always given. With the
²⁵ exception of such quotations, this thesis is entirely my own work.
- ²⁶ • I have acknowledged all main sources of help.
- ²⁷ • Where the thesis is based on work done by myself jointly with others, I have made
²⁸ clear exactly what was done by others and what I have contributed myself.

²⁹

³⁰ Signed:

³¹ _____

³² Date:

³³ _____

34

UNIVERSITY OF BRISTOL

35

Abstract

36

Engineering

37

Department of Computer Science

38

Doctor of Philosophy

39

**Investigating, implementing, and creating methods for analysing large neuronal
ensembles**

41

by Thomas J. DELANEY

42

The Thesis Abstract is written here (and usually kept to just this page). The page is kept centered vertically so can expand into the blank space above the title too...

44

Acknowledgements

45 The acknowledgments and the people to thank go here, don't forget to include your project

46 advisor...

⁴⁷ Contents

⁴⁸	Declaration of Authorship	iii
⁴⁹	Abstract	v
⁵⁰	Acknowledgements	vii
⁵¹	0.1 Introduction	1
⁵²	1 Sensitivity of the spikes-to-fluorescence transform to calcium indicator and neu-	
⁵³	ron properties	3
⁵⁴	1.1 Introduction	6
⁵⁵	1.2 Results	8
⁵⁶	1.2.1 A biophysical computational model can generate accurate fluores-	
⁵⁷	cence traces from spike trains	8
⁵⁸	1.2.2 Spike inference algorithms perform similarly on real data compared	
⁵⁹	with time series simulated from the model	9
⁶⁰	1.2.3 Relative effects of various buffers to the fluorescence signal	10
⁶¹	1.2.4 Spike inference accuracy is sensitive to indicator properties, and likely	
⁶²	varies within and between cells	12
⁶³	1.2.5 Single spike inference accuracy drops for high firing rates, but firing	
⁶⁴	rate itself can be estimated from mean fluorescence amplitude	16
⁶⁵	1.3 Discussion	18
⁶⁶	1.4 Methods	20
⁶⁷	1.4.1 Calcium dynamics model	20
⁶⁸	Photon release & capture	23
⁶⁹	1.4.2 Parameter optimisation	23
⁷⁰	Fixed parameters	25
⁷¹	1.4.3 Julia	26
⁷²	1.4.4 Spike inference	26
⁷³	Comparing spike inference quality	28

74	1.4.5	Perturbation analysis	28
75	1.4.6	Signal-to-noise ratio	29
76	1.4.7	Data sources	29
77	2	Functional networks expand across anatomical boundaries as correlation time-scale increases	31
78	2.1	Introduction	34
79	2.2	Results	35
80	2.2.1	Average correlation size increases with increasing time bin width . .	35
81	2.2.2	Goodness-of-fit for Poisson and Gaussian distributions across increasing time bin widths	36
82	2.2.3	Differences between and inter- and intra- regional correlations decrease with increasing bin width	38
83	2.2.4	Connected and divided structure in correlation based networks reduces in dimension with increasing bin width	41
84	2.2.5	Detecting communities in correlation based networks	42
85	2.2.6	Functional communities resemble anatomical division at short timescales	42
86	2.2.7	Conditional correlations & signal correlations	46
87	2.2.8	Absolute correlations and negative rectified correlations	50
88	2.3	Discussion	53
89	2.4	Data	56
90	2.4.1	Brain regions	56
91	2.4.2	Video recordings	57
92	2.5	Methods	57
93	2.5.1	Binning data	57
94	2.5.2	Correlation coefficients	57
95		Total correlations, r_{SC}	58
96		Shuffled total correlations	58
97		Separating Correlations & Anti-correlations	58
98	2.5.3	Conditioning on behavioural data	59
99		Linear regression	59
100		Elastic net regularisation	59
101		Conditional covariance	60
102		Measures of conditional correlation	61

107	2.5.4	Information Theory	61
108		Entropy $H(X)$	61
109		Maximum entropy limit	62
110		Mutual Information $I(X; Y)$	63
111		Variation of Information $VI(X, Y)$	64
112		Measuring entropies & mutual information	65
113	2.5.5	Network analysis	65
114		Correlation networks	65
115		Rectified correlations	65
116		Sparsifying data networks	66
117		Communities	66
118		Weighted configuration model	66
119		Sparse weighted configuration model	66
120		Spectral rejection	67
121		Node rejection	68
122		Community detection	68
123	2.5.6	Clustering Comparison	69
124		Adjusted Rand Index	69
125		Clusterings as random variables	70
126		Information based similarity measures	70
127		Information based metrics	71
128		Comparing detected communities and anatomical divisions	71
129	3	A simple two parameter distribution for modelling neuronal activity and capturing neuronal association	73
130	3.1	Introduction	76
131	3.2	Data	77
132	3.2.1	Experimental protocol	77
133	3.3	Methods	78
134	3.3.1	Binning data	78
135	3.3.2	Number of <i>active</i> neurons	78
136	3.3.3	Moving windows for measurements	78
137	3.3.4	Fano factor	80
138	3.3.5	Probability Distributions suitable for modelling ensemble activity	80

140	Association	80
141	Binomial distribution	81
142	Beta-binomial distribution	81
143	Conway-Maxwell-binomial distribution	82
144	3.3.6 Fitting	84
145	3.3.7 Goodness-of-fit	86
146	3.4 Results	86
147	3.4.1 Increases in mean number of active neurons and variance in number of active neurons at stimulus onset in some regions	86
148	Primary visual cortex	87
149	Hippocampus	87
150	Thalamus	87
151	3.4.2 Conway-Maxwell-binomial distribution is usually a better fit than bi- nomial or beta-binomial	87
152	3.4.3 Conway-Maxwell-binomial distribution captures changes in associa- tion at stimulus onset	92
153	3.4.4 Replicating stimulus related quenching of neural variability	92
154	3.5 Discussion	94
158	4 Studies with practical limitations & negative results	97
159	4.1 Dynamic state space model of pairwise and higher order neuronal correlations	100
160	4.2 A multiscale model for hierarchical data applied to neuronal data	100
161	4.3 Discussion	102
163	Bibliography	103

164 List of Figures

165 1.1	A: Example spike train (blue) and the corresponding GCaMP6s fluorescence 166 trace (green), data replotted from (Berens et al., 2018). Inset shows zoomed 167 section of traces to highlight slow decay of GCaMP6s fluorescence relative 168 to spike time intervals. B: Schematic diagram of the neuron calcium and 169 GCaMP computational model. C: Good visual match of data fluorescence 170 trace (green) and model simulated fluorescence (orange) in response to an 171 identical spike train (blue).	7
172 1.2	A: Workflow to compare spike inference for real versus simulated fluores- 173 cence data. B: True positive rates achieved by three different spike inference 174 algorithms when applied to observed spike trains, and simulated spike trains. 175 Data points overlaid as blue circles. The performance is similar from real 176 and simulated data for each of the algorithms.	10
177 1.3	Calcium Buffering Dynamics (a) The proportions of bound and free cal- 178 cium concentrations within a cell, with the associated spike train. (b)-(f) The 179 dynamics of the concentration of (b) excited indicator bound calcium, (c) in- 180 dicator bound calcium, (d) immobile endogenous buffer bound calcium, (e) 181 mobile endogenous buffer bound calcium, and (f) free calcium in response to 182 an action potential at $\sim 23.2\text{s}$	11
183 1.4	(a) An example trace for each of the five pairs of values used for the binding 184 and unbinding rates of the fluorescent calcium indicator. (b) The signal-to- 185 noise ratio of the modelled fluorescence traces using each of the four per- 186 turbed values, and the experimental value. The SNRs for the two pairs with 187 values lower than the experimental value are lower than the experimental pair 188 or the higher value pairs. (c) The true-positive rates of the deconvolution al- 189 gorithm's predictions when inferring from the observed data, and inferring 190 from modelled traces using the perturbed and experimental values.	14

191	1.5 (a) An example trace for each of the five perturbed values for the concentration of fluorescent calcium indicator. The top two traces are produced by the lower perturbed values, the middle trace is produced by the experimental value, and the lowest two traces are produced when using the higher perturbed values. (b) The signal-to-noise ratio of the modelled fluorescence traces using each of the four perturbed values, and the experimental value. Extreme perturbations of the concentration either above or below the experimental level lowered the SNR. (c) The true-positive rates of the deconvolution algorithm's predictions when inferring from the observed data, and inferring from modelled traces using the perturbed and experimental values. We found that the algorithms performs equally badly on the two most extreme values, and performs equally well on the experimental value, and the next higher perturbed value.	15
204	1.6 (a) An example trace for each of the five perturbed values for the concentration of immobile endogenous buffer. (b) The signal-to-noise ratio of the modelled fluorescence traces using each of the four perturbed values, and the experimental value. The lower values for the immobile buffer produce the same SNR as the experimental value. But the higher perturbed values produce fluorescence traces with a lower SNR. (c) The true-positive rates of the deconvolution algorithm's predictions when inferring from the observed data, and inferring from modelled traces using the perturbed and experimental values.	17
213	1.7 Simulating fluorescence traces at different firing rates Example modelled traces created using simulated spike trains with a mean firing rate of 1Hz (left column), 5Hz (middle column), and 10Hz (right column). Note the difference in amplitude with different mean firing rates.	18
217	1.8 Inference quality and $\Delta F/F_0$ vs Firing rate (left) The spike inference accuracy when applied to 30 traces created using simulated spike trains with mean firing rates of 1, 5, and 10 Hz. (right) The mean $\Delta F/F_0$ across those 30 traces for each frequency.	18

221	2.1 (A) An example of the correlation coefficients between two different pairs 222 of cells, one where both cells are in the same brain region (intra-regional 223 pair), and one where both cells are in different brain regions (inter-regional 224 pair). The correlation coefficients have been measured using different time 225 bin widths, ranging from 5ms to 3s. Note the increasing amplitude of the 226 correlations with increasing bin width. (B) A raster plot showing the spike 227 times of each pair of cells.	36
228	2.2 Mean correlation coefficients measured from pairs of 50 randomly chosen 229 neurons. (A) All possible pairs, (B) positively correlated pairs, and (C) neg- 230 atively correlated pairs. (D) Mean and standard error of χ^2 test statistics for 231 Poisson and Gaussian distributions fitted to neuron spike counts.	37
232	2.3 (Left)The mean intra-region and inter-region correlations using all possible 233 pairs of \sim 500 neurons, spread across 9 different brain regions. (Right) 234 Courtesy of Stringer et al. (2019), mean inter-regional (out-of-area) correla- 235 tion coefficients vs mean intra-regional (within-area) correlation coefficients 236 for a bin width of 1.2s. Note that the intra-regional coefficients are higher in 237 each case.	39
238	2.4 The mean intra-regional correlations (coloured dots) and mean inter-regional 239 correlations (black dots) for a given region, indicated on the x-axis, for dif- 240 ferent time bin widths. Each black dot represents the mean inter-regional 241 correations between the region indicated on the x-axis and one other re- 242 gion. (A) shows these measurements when we used a time bin width of 5ms. 243 (B) shows these measurements when we used a time bin width of 1s. Note 244 that the difference between the mean inter-regional correlations and mean 245 intra-regional correlations is smaller for 1s bins.	40
246	2.5 Mean inter-regional (main diagonal) and intra-regional (off diagonal) corre- 247 lation coefficients. (A) Shows these measurements when spike times were 248 binned using 5ms time bins. (B) Shows the same, using 1s time bins. Note 249 that the matrices are ordered according to the main diagonal values, therefore 250 the ordering is different in each subfigure.	41

251	2.6 The number of dimensions in the k -partite and connected structure in the cor-	
252	relation based networks beyond the structure captured by a sparse weighted	
253	configuration null network model (see section 2.5.5), shown for different time	
254	bin widths. Note that the k -partite structure disappears for time bin width	
255	greater than 200ms for all three subjects. The dimension of the connected	
256	structure reduces with increasing bin width for 2 of the 3 subjects (top row).	43
257	2.7 (A-B) Correlation matrices with detected communities indicated by white	
258	lines. Each off main diagonal entry in the matrix represents a pair of neu-	
259	rons. Those entries within a white square indicate that both of those neurons	
260	are in the same community as detected by our community detection proce-	
261	dure. Matrices shown are for 5ms and 1s time bin widths respectively. Main	
262	diagonal entries were set to 0. (C-D) Matrices showing the anatomical dis-	
263	tribution of pairs along with their community membership. Entries where	
264	both cells are in the same region are given a colour indicated by the colour	
265	bar. Entries where cells are in different regions are given the grey colour also	
266	indicated by the colour bar.	44
267	2.8 (A) The variation of information is a measure of distance between cluster-	
268	ings. The distance between the anatomical ‘clustering’ and community de-	
269	detection ‘clustering’ increases with increasing time bin width. (B) The ad-	
270	justed Rand index is a normalised similarity measure between clusterings.	
271	The anatomical and community detection clusterings become less similar as	
272	the time bin width increases.	45
273	2.9 Comparing the components of the total covariance across different values for	
274	the time bin width. We observed a consistent increase in $E[\text{cov}(X, Y Z)]$ as	
275	the time bin width increased. But we saw different trends for $\text{cov}(E[X Z], E[Y Z])$	
276	for each mouse.	46
277	2.10 Comparing the components of the total covariance across different values for	
278	the time bin width. We saw a consistent increase in $\rho_{X,Y Z}$ as the time bin	
279	width increased in all three subjects. But we saw different trends in ρ_{signal} for	
280	each of the subjects.	47

281	2.11 Matrices showing the regional membership of pairs by colour, and the com-	
282	munities in which those pairs lie. (A-B) Detected communities and regional	
283	membership matrix for network based on rectified spike count correlation	
284	$\rho_{X,Y Z}$, using time bin widths of 0.005s and 1s respectively. (C-D) Detected	
285	communities and regional membership matrix for network based on rectified	
286	signal correlation ρ_{signal} , using time bin widths of 0.005s and 1s respectively.	48
287	2.12 Distance and similarity measures between the anatomical division of the neu-	
288	rons, and the communities detected in the network based on the spike count	
289	correlations $\rho_{X,Y Z}$. (A) The variation of information is a ‘distance’ mea-	
290	sure between clusterings. The distance between the anatomical ‘clustering’	
291	and the community clustering increases as the time bin width increases. (B)	
292	The adjusted Rand index is a similarity measure between clusterings. The	
293	detected communities become less similar to the anatomical division of the	
294	cells as the time bin width increases.	49
295	2.13 Distance and similarity measures between the anatomical division of the neu-	
296	rons, and the communities detected in the network based on the signal cor-	
297	relations ρ_{signal} . (A) The variation of information is a ‘distance’ measure be-	
298	tween clusterings. The distance between the anatomical ‘clustering’ and the	
299	community clustering increases as the time bin width increases. (B) The ad-	
300	justed Rand index is a similarity measure between clusterings. The detected	
301	communities become less similar to the anatomical division of the cells as	
302	the time bin width increases.	50
303	2.14 (A-B) Absolute correlation matrices with detected communities indicated by	
304	white lines. These communities are based on the absolute value of the total	
305	correlation between each pair of cells. Those entries within a white square in-	
306	dicate that both of those neurons are in the same community. Matrices shown	
307	are for 5ms and 1s time bin widths respectively. Main diagonal entries were	
308	set to 0. (C-D) Matrices showing the anatomical distribution of pairs along	
309	with their community membership. Regional membership is indicated by the	
310	colour bar. (E) Variation of information between the anatomical division of	
311	the cells, and the detected communities. (F) Adjusted Rand index between	
312	the anatomical division, and the detected communities.	51

313	2.15 (A-B) Sign reversed rectified correlation matrices with detected communities indicated by white lines. Those entries within a white square indicate that both of those neurons are in the same community. Matrices shown are for 5ms and 1s time bin widths respectively. Main diagonal entries were set to 0. (C-D) Matrices showing the anatomical distribution of pairs along with their community membership. Regional membership is indicated by the colour bar. (E) Variation of information between the anatomical division of the cells, and the detected communities. (F) Adjusted Rand index between the anatomical division, and the detected communities.	52
322	2.16 Probe Locations: The locations of the probes in each of the three mouse brains (Stringer et al., 2019).	57
324	2.17 Entropy Limit: The upper limit on entropy of binned spike count data as a function of the maximum observed spike count. The orange line is the analytical maximum. The blue line is the entropy of samples with $N = 1000$ data points taken from the discrete uniform distribution.	63
328	3.1 Figures showing the over-dispersion possible for a beta-binomial distribution relative to a binomial distribution. Parameters are shown in the captions.	82
330	3.2 Figures showing (A) the under-dispersion and (B) over-dispersion permitted by the COMb distribution relative to a binomial distribution. (C) illustrates that the p parameter of the COMb distribution does not correspond to the mean of the distribution, as it does for the binomial and beta-binomial distributions. (D) shows a heatmap for the value of the Kullback-Liebler divergence between the COMb distribution and the standard binomial distribution with same value for n , as a function of p and ν . Parameters are shown in the captions.	85

338	3.3 (A) Raster plot showing the spikes fired by 33 randomly chosen neurons in 339 the primary visual cortex. (B-C) (B) average and (C) variance of the number 340 of active neurons, measured using a sliding window 100ms wide, split into 341 100 bins. The midpoint of the time interval for each window is used as the 342 timepoint (x-axis point) for the measurements using that window. The grey 343 shaded area indicates the presence of a visual stimulus. The opaque line is 344 an average across the 160 trials that included a visual stimulus of any kind. 345 We can see a transient increase in the average number of active neurons and 346 the variance of this number, followed by a fluctuation and another increase. 88
347	3.4 (A) Raster plot showing the spikes fired by 33 randomly chosen neurons in 348 the hippocampus. (B-C) (B) average and (C) variance of the number of active 349 neurons, measured using a sliding window 100ms wide, split into 100 bins. 350 The midpoint of the time interval for each window is used as the timepoint (x- 351 axis point) for the measurements using that window. The grey shaded area 352 indicates the presence of a visual stimulus. The opaque line is an average 353 across the 160 trials that included a visual stimulus of any kind. We can see 354 a transient increase in the average number of active neurons and the variance 355 of this number at stimulus onset. 89
356	3.5 (A) Raster plot showing the spikes fired by 33 randomly chosen neurons in 357 the thalamus. (B-C) (B) average and (C) variance of the number of active 358 neurons, measured using a sliding window 100ms wide, split into 100 bins. 359 The midpoint of the time interval for each window is used as the timepoint (x- 360 axis point) for the measurements using that window. The grey shaded area 361 indicates the presence of a visual stimulus. The opaque line is an average 362 across the 160 trials that included a visual stimulus of any kind. We can 363 see in immediate increase at stimulus onset, a subsequent fall, and another 364 sustained increased until the stimulus presentation ends. 90

- 365 3.6 (A) An example of the binomial, beta-binomial, and Conway-Maxwell-binomial
366 distributions fitted to a sample of neural activity. The Conway-Maxwell-
367 binomial distribution is the best fit in this case. The histogram shows the
368 empirical distribution of the sample. The probability mass function of each
369 distribution is indicated by a different coloured line. (B) Across all samples
370 in all trials, the proportion of samples for which each fitted distribution was
371 the the best fit. The Conway-Maxwell-binomial distribution was the best fit
372 for 93% of the samples taken from V1 using a bin width of 1ms. 91
- 373 3.7 (A) We fit a Conway-Maxwell-binomial distribution to the number of active
374 neurons in 1ms time bins of a 100ms sliding window. We did this for all
375 trials with a visual stimulus and took the average across those trials. We
376 see a transient drop in value for the distribution's ν parameter at stimulus
377 onset. This shows an increase in association between the neurons. (B) We
378 measured the correlation coefficient between the spike counts of all possible
379 pairs of neurons in the same sliding window. The took the average of those
380 coefficients. We also did this for every visually stimulated trial, and took
381 the average across trials. The increase in association is not reflected with an
382 increase in average correlation. 93
- 383 3.8 (A) The mean Fano factor of the spike counts of the cells in the primary visual
384 cortex. Means were taken across cells first, then across trials. There was a
385 significant decrease in the Fano factors immediately after stimulus onset. (B)
386 The mean Fano factor of the spike counts of the cells in the motor cortex. No
387 significant change in measurements at any point. 94

388 List of Tables

389	1.1	388 Fixed parameters A table of the parameters fixed before optimising the model. The values of these parameters could be changed to model different fluorescent calcium indicators.	25
390	3.1	392 Details of the different bin width and analysis window sizes used when binning spike times, and analysing those data.	79
391	3.2	394 Relative dispersion of the COMb distribution, and association between Bernoulli variables as represented by the value of the ν parameter.	84
392	3.3	396 Proportion of samples for which each distribution was the best fit, grouped by bin width. The COMb distribution is the best fit most of the time.	92
397			

For/Dedicated to/To my. . .

399 0.1 Introduction

400 Ideas (not in order):

- 401 ● From small for big datasets (in terms of number of neurons)
- 402 ● Big datasets mean statistical methods are more necessary (curse of dimensionality)
- 403 ● Big datasets mean higher order correlations are more meaningful (schneidman)
- 404 ● Exploit pairwise correlations in different way (eight probe)
- 405 ● abandon correlations embrace association (COMB)
- 406 ● electrophysiology drawbacks vs calcium benefits
- 407 ● calcium drawbacks (fluorescence modelling)

⁴⁰⁸ **Chapter 1**

⁴⁰⁹ **Sensitivity of the**
⁴¹⁰ **spikes-to-fluorescence transform to**
⁴¹¹ **calcium indicator and neuron**
⁴¹² **properties**

413

UNIVERSITY OF BRISTOL

414

Abstract

415

Engineering

416

Department of Computer Science

417

Doctor of Philosophy

418

Investigating, implementing, and creating methods for analysing large neuronal ensembles

420

by Thomas J. DELANEY

421

Fluorescent calcium indicators such as GCaMP are widely used to monitor neuronal activity.

422

However the relationship between the fluorescence signal and the underlying action potential

423

firing is poorly understood. This lack of knowledge makes it difficult for experimenters

424

to decide between different indicator variants for a given application. We addressed this

425

problem by studying a basic biophysical model of calcium dynamics in neuronal soma. We

426

fit the model parameters to publicly available data where GCaMP6s fluorescence and whole-

427

cell electrophysiological recordings were made simultaneously in the same single neurons.

428

We systematically varied the model's parameters to characterise the sensitivity of spike train

429

inference algorithms to the calcium indicator's main biophysical properties: binding rate,

430

dissociation rate, and molecular concentration. This model should have two potential uses:

431

experimental researchers may use it to help them select the optimal indicator for their desired

432

experiment; and computational researchers may use it to generate simulated data to aid design

433

of spike inference algorithms.

434

1.1 Introduction

435 Although fluorescent calcium indicators such as GCaMP are widely used to monitor neuronal
436 activity, the relationship between the fluorescence signal and the underlying action potential
437 firing is imperfect. The fluorescence signal has a low signal-to-noise ratio, and most indi-
438 cators' kinetics are slow relative to the millisecond-timescale dynamics of the membrane
439 voltage (example in Figure 1). This makes spike inference difficult. Furthermore, the effects
440 of the indicator and cell properties on the fluorescence signal are unknown. For example,
441 genetically encoded indicators can accumulate within neurons over weeks and months (Chen
442 et al., 2013). Studies using calcium-sensitive fluorescent dyes have shown that indicator con-
443 centration has substantial effects on the spike-to-fluorescence relationship (Maravall et al.,
444 2000). Therefore spike rates inferred from GCaMP fluorescence signals may give mislead-
445 ing results if comparing across imaging sessions. More generally, the poor understanding of
446 the spike-to-fluorescence transform means experimenters may not know whether to trust the
447 outputs of spike train inference methods in any given application.

448 Spike trains are usually inferred from the time series of intensity values of one pixel of the
449 fluorescence image, where the pixel is located at the cell's soma. The problems of identifying
450 these pixels, and inferring spikes from their time series can solved separately or together.
451 When attempting to infer spikes, the fluorescence trace is modelled as a linear combination of
452 calcium concentration dynamics, a baseline calcium concentration, and some Gaussian noise.
453 The calcium concentration dynamics are modelled as an autoregressive process of degree 1
454 or 2 with a pulse input corresponding to the spike train, or the number of spikes fired in a
455 time step. The model includes no dynamics for the fluorescent indicator itself. Furthermore,
456 in order to make this model into an easily solvable linear programming problem the number
457 of spikes fired in a timestep is not restricted to non-negative integers but to arbitrary non-
458 negative values (Vogelstein et al., 2010; Pnevmatikakis et al., 2016; Friedrich and Paninski,
459 2016; Pnevmatikakis et al., 2013; Pnevmatikakis et al., 2014). More biologically inspired
460 spike inference models do exist (Deneux et al., 2016), but their fundamentals are very similar.
461 In this work, we investigated the effect of changing dynamics and buffer concentrations on
462 the accuracy of the inference algorithms based on these models.

463 The aim of this project was to model the fluorescence traces produced by a fluorescent
464 calcium indicator in a neuron soma resulting from a specific spike train, given calcium indi-
465 cator parameters such as binding rate, dissociation rate, and molecular concentration. Such

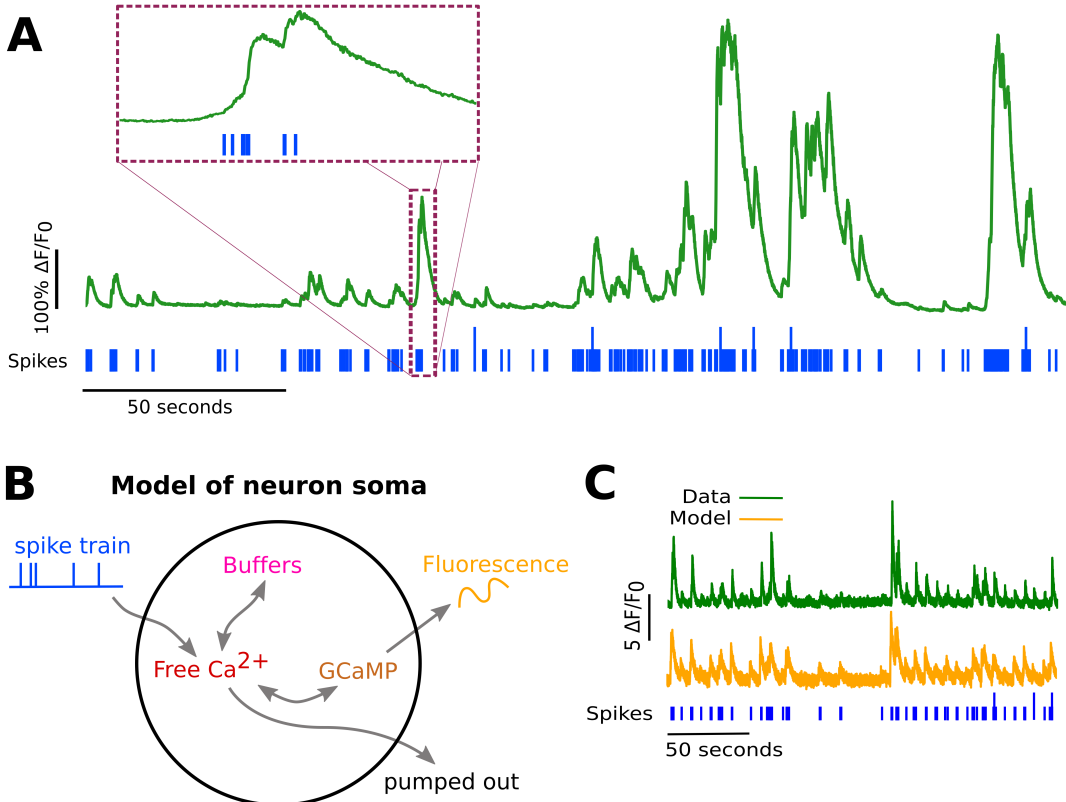


FIGURE 1.1:

A: Example spike train (blue) and the corresponding GCaMP6s fluorescence trace (green), data replotted from (Berens et al., 2018). Inset shows zoomed section of traces to highlight slow decay of GCaMP6s fluorescence relative to spike time intervals.

B: Schematic diagram of the neuron calcium and GCaMP computational model.

C: Good visual match of data fluorescence trace (green) and model simulated fluorescence (orange) in response to an identical spike train (blue).

466 a model would allow benchmarking of various spike inference algorithms, and enable under-
 467 standing of how indicator characteristics affect the quality of spike train inference.

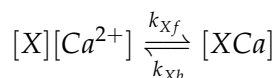
468 The model we developed consisted of free calcium, fluorescent indicator molecules, and
 469 mobile and immobile endogenous calcium buffers. The indicator molecules which were
 470 bound to a calcium molecule could be either excited, i.e. able to release a photon, or relaxed.
 471 In order to reproduce the noise inherent in the data collection, we modelled the release of
 472 photons from the excited indicator bound calcium as a stochastic process.

473 The fluorescence traces produced by the simulation were calibrated to reproduce the
 474 signal-to-noise ratio observed in experimental data. Previously published spike inference
 475 algorithms were then used to infer spike trains from the experimental fluorescence traces and
 476 the modelled fluorescence traces. The parameters of the model were then varied in order to
 477 determine the effect on the system dynamics and the effects on spike inference.

478 1.2 Results

479 1.2.1 A biophysical computational model can generate accurate fluorescence
480 traces from spike trains

To study the relationship between action potential firing and calcium fluorescence, we built a computational model of calcium dynamics in a neuronal soma. The model consisted of four dynamic variables: the concentration of free calcium, two types of endogenous buffer, and the calcium-sensitive fluorescent indicator. Each of the buffers and the indicator could independently bind and unbind with calcium. These reactions were modelled as



481 where X is the buffer concentration and Ca^{2+} is the calcium concentration. Each species
482 could therefore exist in two states: either bound with calcium or unbound. To model the
483 imaging process, we also added a third, excited state to the indicator. When in the calcium-
484 bound state, the indicator could be converted to an excited state, corresponding to the absorp-
485 tion of a photon. The rate of this excitation process could be interpreted as the intensity of
486 the light illuminating the sample. Once excited, the species decayed back to the unexcited
487 state at a fixed rate, corresponding to the spontaneous emission of photons. The total emitted
488 fluorescence signal was interpreted as proportional to this de-excitation flux. To represent
489 experimental noise in the photon capture process, we drew a random number of captured
490 photons at each time step from a binomial distribution, parameterised by a number p that
491 corresponds to the mean fraction of released photons that are captured.

492 The model had 17 parameters in total describing the molecules' concentrations and re-
493 action rates (Methods). We set 13 of these parameters to values from the literature. The
494 remaining 4 parameter values we fit to publicly-available data (Berens et al., 2018), briefly
495 explained as follows (see Methods for full details). Single neurons from acute rat cortical
496 slices expressing GCaMP6f were imaged with two-photon microscopy while the membrane
497 potentials of the somata of the same neurons were simultaneously recorded via whole-cell
498 patch clamp electrophysiology. In this dataset, the electrical recordings give unambiguous
499 information about neurons' spike times. To do the parameter fitting, we feed these spike
500 trains as inputs to the computational model. After running, the model returns a simulated
501 fluorescence trace. We aimed to find the model parameter values that give the best match
502 between this simulated fluorescence trace and the real fluorescence time series recorded in

503 the corresponding neuron. To do this we used a suite of optimisation procedures to jointly
504 fit both the real neuron's fluorescence time series and power spectrum, which capture com-
505 plementary information about the spikes-to-fluorescence mapping (Methods). We performed
506 the fitting procedure independently for each of the 20 neurons in the spikefinder dataset
507 (<http://spikefinder.org>). After fitting, the model produced realistic-looking fluorescence time
508 series (Figure 1.1).

509 **1.2.2 Spike inference algorithms perform similarly on real data compared with**
510 **time series simulated from the model**

511 Researchers often pass the fluorescence time series through a spike inference tool before per-
512 forming further statistical analyses. These spike inference algorithms take the fluorescence
513 trace as input and attempt to estimate the neuronal spike train that triggered them (Vogelstein
514 et al., 2010; Pnevmatikakis et al., 2016; Friedrich and Paninski, 2016; Pnevmatikakis et al.,
515 2013; Pnevmatikakis et al., 2014; Deneux et al., 2016). Part of our motivation for building
516 this model was to allow us to ask the question: how do the properties of the cell and the
517 calcium indicator affect the quality of spike inference? In order to trust the conclusions from
518 our model, we should first be confident that spike inference from our simulated fluores-
519 cence traces is similar to that from the real data. To test this we passed each of the simulated fluores-
520 cence traces through three previously published spike inference algorithms, quantified their
521 performance against the ground-truth electrophysiology data, repeated the procedure for the
522 real calcium fluorescence time series, and compared the accuracy of the inference processes
523 in all cases. The *true positive rate*, also known as the *recall*, the *sensitivity*, or the *probabi-*
524 *lity of detection* of spike inference varied across the three inference algorithms we tried (*p*
525 value and statistical test here). The constrained non-negative matrix deconvolution algorithm
526 (Pnevmatikakis et al., 2016) (CNMD algorithm) correctly detected approximately 45% of the
527 true spikes, the OASIS algorithm (Friedrich and Paninski, 2016) correctly detected approx-
528 imately 35% of the true spikes, and the ML spike algorithm (Deneux et al., 2016) correctly
529 detected approximately 15% of the true spikes (see figure 1.2). Notably, for two of the three
530 inference algorithms, the quality of inference was also fairly consistent for individual spike
531 trains, not just the group means ($p > 0.05$, paired t-test). This demonstrates that the models
532 were generating fluorescence time series that were similarly difficult to decode as the real
533 data, in ways that were not specific to any one inference algorithm. This is evidence that the
534 models captured real aspects of the spikes-to-fluorescence transform.

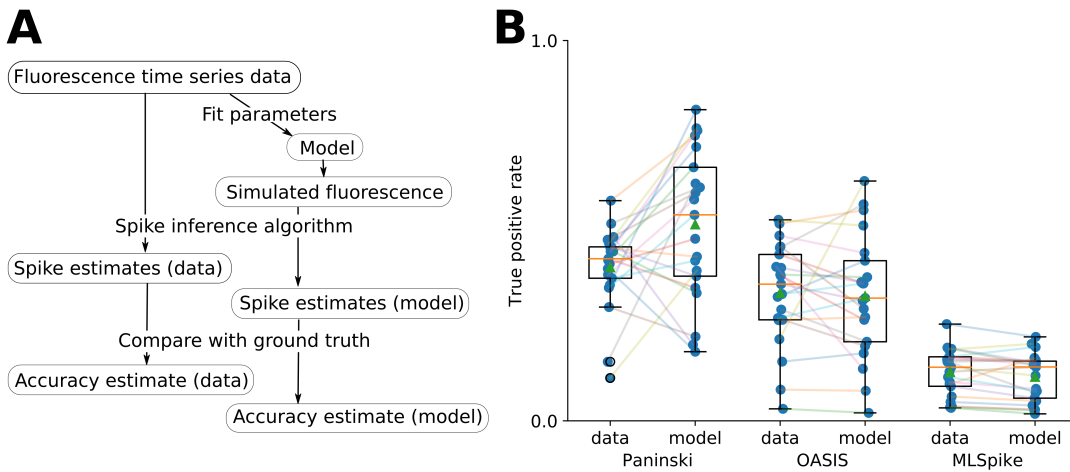


FIGURE 1.2:
A: Workflow to compare spike inference for real versus simulated fluorescence data.

B: True positive rates achieved by three different spike inference algorithms when applied to observed spike trains, and simulated spike trains. Data points overlaid as blue circles. The performance is similar from real and simulated data for each of the algorithms.

535 1.2.3 Relative effects of various buffers to the fluorescence signal

536 One of the benefits of computational models over laboratory experiments is that we can
 537 observe all the variables in the simulation to gain insight into the system's dynamics, which
 538 can be difficult to do in the lab. We plotted the concentrations of the various species over
 539 time for a version of the model fit to one data set, in response to the same train of spikes used
 540 for fitting (figure 1.3). Figure 1.3a shows the absolute values of the species concentrations,
 541 summed. Consistent with experimental estimates (Maravall et al., 2000), only a small fraction
 542 ($\sim 0.1\%$) of calcium is free and unbound to any buffer. Of the bound calcium, the vast
 543 majority, ($\sim 96\%$) is bound to the GCaMP indicator. The two types of endogenous buffer
 544 are bound to the remaining calcium ($\sim 4\%$). An influx of calcium from a single spike adds
 545 very little to the total calcium, in relative terms (red line in Figure 3a).

546 When calcium entered the model neuron it was rapidly buffered (Bartol et al., 2015).
 547 However the relative fractions of which buffer molecules bound to the influxed calcium was
 548 dynamic, and changed over time . Figure 1.3 (b-f) shows the time course of the various
 549 species over time in response to a calcium influx event from a single action potential. Cru-
 550 cially, the indicator $[BCa]$ competed with the endogenous buffers $[ImCa]$ and $[ECa]$ – all
 551 three bind calcium on similar timescales. This implies that the timecourse and amplitude of
 552 the $[BCa]$ variable will also depend on the binding rates and availabilities of the endogenous
 553 buffers. For example if we decreased the concentration of an endogenous buffer, we might

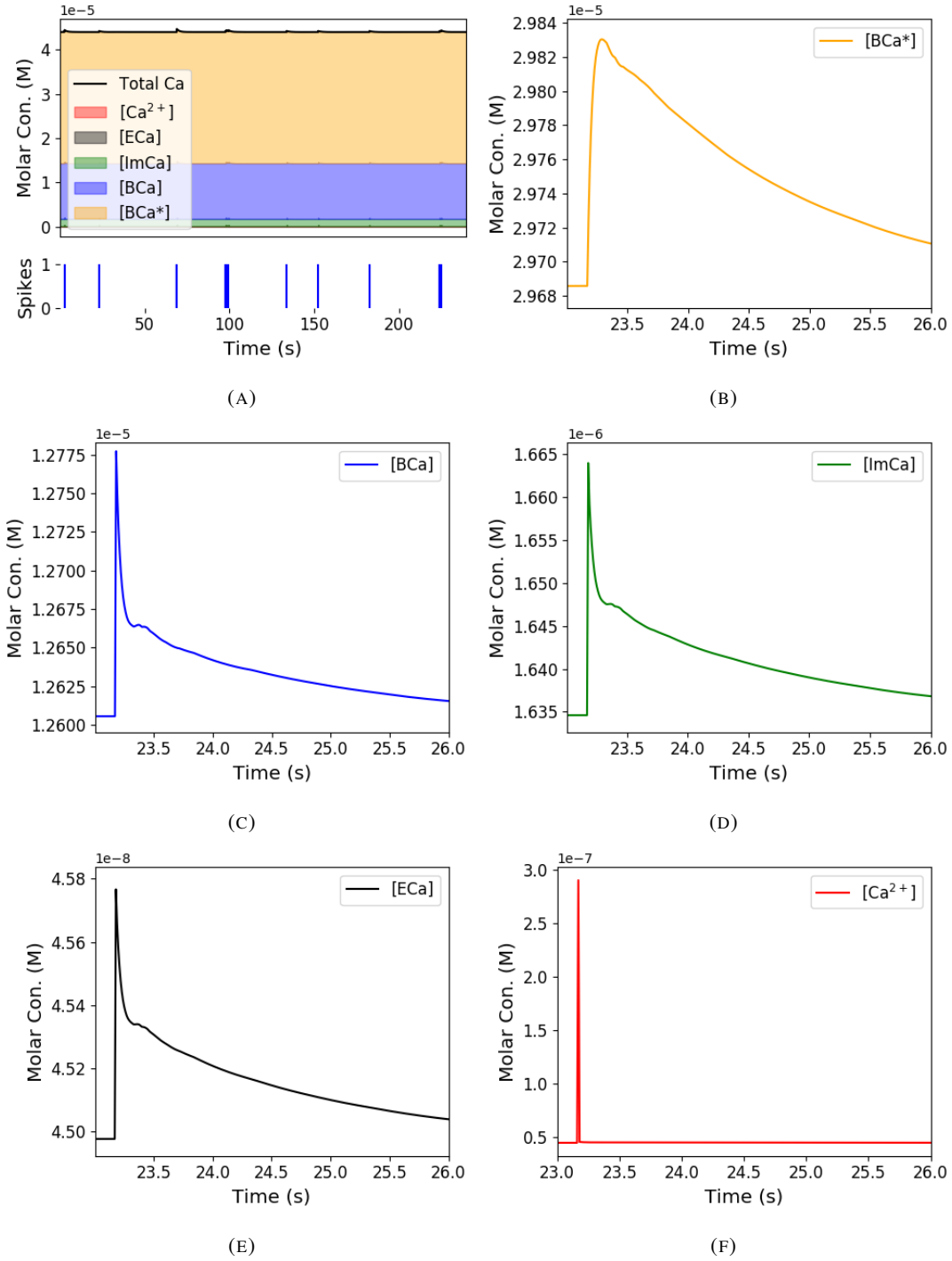


FIGURE 1.3: Calcium Buffering Dynamics (a) The proportions of bound and free calcium concentrations within a cell, with the associated spike train. (b)-(f) The dynamics of the concentration of (b) excited indicator bound calcium, (c) indicator bound calcium, (d) immobile endogenous buffer bound calcium, (e) mobile endogenous buffer bound calcium, and (f) free calcium in response to an action potential at $\sim 23.2\text{s}$.

554 expect both a faster rise time and greater peak amplitude of the $[BCa]$ signal in response to
555 a calcium influx event. The slowest component of the decay had a similar time constant for
556 $[BCa]$, $[ImCa]$ and $[ECa]$, which in turn matched the $[Ca]$ extrusion time constant in our
557 model ($\sim 6.29 \times 10^{-22} \text{Ms}^{-1}$). This implies that the buffers and the indicator had reached
558 a dynamic equilibrium and were jointly tracking the free calcium concentration as calcium
559 was slowly extruded from the cell.

560 Interestingly the excited bound calcium species ($[BCa^*]$) showed a qualitatively different
561 timescale in response to a calcium influx event. This concentration is subject to the added
562 ‘excitation and release’ dynamic, where a certain proportion of the concentration absorbs the
563 energy from an incoming photon and goes into an ‘excited state’ at each time step. A certain
564 proportion of the concentration releases a photon and reverts to a ‘relaxed state’ at each
565 timestep also. This means that the excited bound calcium lags behind the bound calcium
566 trace. We could think of the excited bound calcium trace as a low pass filtered version of the
567 bound calcium trace.

568 **1.2.4 Spike inference accuracy is sensitive to indicator properties, and likely
569 varies within and between cells**

570 The above results imply that the fluorescence signal depends on the relative properties of
571 both GCaMP and the endogenous buffers. We next used the model to directly ask how
572 sensitive spike inference was to these components. We focused on three key parameters that
573 likely vary from cell to cell and experiment to experiment: GCaMP binding kinetics, GCaMP
574 concentration, and endogenous buffer concentration.

575 Several variants of GCaMP itself have been made that differ in calcium binding kinetics,
576 baseline fluorescence, fluorescence efficiency, and other factors. For example, GCaMP6f has
577 a decay time constant of $\sim 1\text{s}$, while GCaMP6s has a decay time constant of $\sim 2\text{s}$ (Chen
578 et al., 2013). Here we asked how these differences in binding kinetics affect spike inference.
579 We jointly varied the calcium binding and unbinding rates of the indicator by the same factor
580 over a range from 100-fold slower to 100-fold faster from the fitted values, and simulated the
581 fluorescence response for each of the parameter settings in response to the same spike trains
582 as before (figure 1.4). Notably this manipulation does not affect the indicators affinity, and
583 therefore would not affect steady-state responses to prolonged changes in calcium. Instead
584 it is likely to affect its sensitivity to the spike train dynamics. We computed two summary
585 measures from the simulated fluorescence traces: the signal-to-noise ratio for a single spike
586 (Methods, section 1.4.6), and the accuracy of spike inference for each of the spike trains. We

587 observed a reduction in the signal-to-noise ratio and the spike inference quality when we set
588 the binding and unbinding rates were set to one hundredth of their fitted values, and to one
589 tenth of their fitted values. When we increased the value of both binding rates, we observed
590 no change in these measurements. The reduction in both rates lead to smaller increases in
591 fluorescence in response to an action potential and a longer decay time (figure 1.4a), this
592 caused the reduction in signal-to-noise ratio. As both rates were increased, the change in
593 $\Delta F/F_0$ in response to an action potential increased and the decay time decreased slightly,
594 but the fluorescence trace created by these values was very similar to the trace created by the
595 fitted values.

596 Second, the overall concentrations of GCaMP often varies from cell to cell. For exam-
597 ple different cells, even of the same type in the same tissue, can express different levels of
598 GCaMP, due to proximity to the infection site, or the cell becoming ‘nuclear-filled’ (Tian et
599 al., 2009; Chen et al., 2013). Also, GCaMP is often used for longitudinal experiments where
600 the same cells are re-imaged across multiple days or weeks. However since GCaMP expres-
601 sion typically ramps up over time (Chen et al., 2013), the accuracy of spike inference may
602 differ across multiple longitudinal recordings in the same cell. We addressed this by varying
603 the concentration of calcium indicator in the model, simulating spike trains and measuring
604 signal-to-noise ratio and spike inference accuracy on the resulting fluorescence traces. Both
605 increasing and decreasing the concentration of the indicator had effects on the fluorescence
606 trace, signal-to-noise ratio, and spike inference. The signal-to-noise ratio and spike infer-
607 ence quality decreased with decreased indicator concentration, and both showed a decrease
608 when the indicator concentration was increased to 100 times it’s fitted value (figure 1.5).
609 The signal-to-noise ratio showed an increase when the indicator concentration was increased
610 to 10 times it’s fitted value, but there was no corresponding change in the spike inference
611 quality. The decrease in indicator concentration caused a reduction in the increase in $\Delta F/F_0$
612 in response to an action potential, and an increase in the decay time of this increase (figure
613 1.5a). The increase in indicator concentration had the opposite effect, it caused an increase
614 in the change in $\Delta F/F_0$ in response to an action potential, and a decrease in the decay time.

615 Third, the concentration and types of endogenous calcium buffers also vary from neuron
616 to neuron, both within and between cell types (Bartol et al., 2015; Maravall et al., 2000;
617 Neher and Augustine, 1992). Since the calcium buffer capacity of neurons is high, around
618 50-70 (Lee et al., 2000) in excitatory hippocampal pyramidal cells, around 100-250 (Lee et
619 al., 2000) in inhibitory hippocampal pyramidal cells, and 900-200 in Purkinje cells (depend-
620 ing on the age of the subject), these endogenous buffers compete with GCaMP for binding

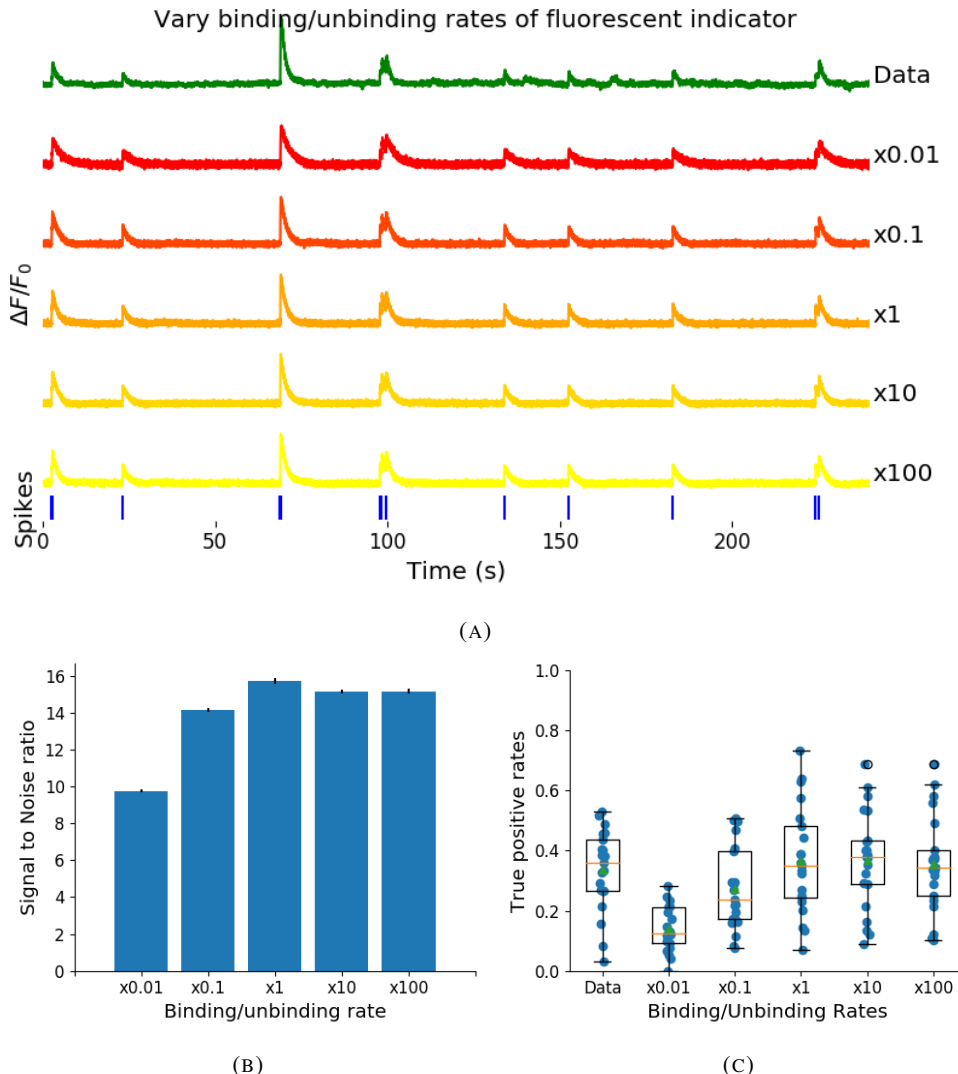


FIGURE 1.4: (a) An example trace for each of the five pairs of values used for the binding and unbinding rates of the fluorescent calcium indicator. (b) The signal-to-noise ratio of the modelled fluorescence traces using each of the four perturbed values, and the experimental value. The SNRs for the two pairs with values lower than the experimental value are lower than the experimental pair or the higher value pairs. (c) The true-positive rates of the deconvolution algorithm's predictions when inferring from the observed data, and inferring from modelled traces using the perturbed and experimental values.

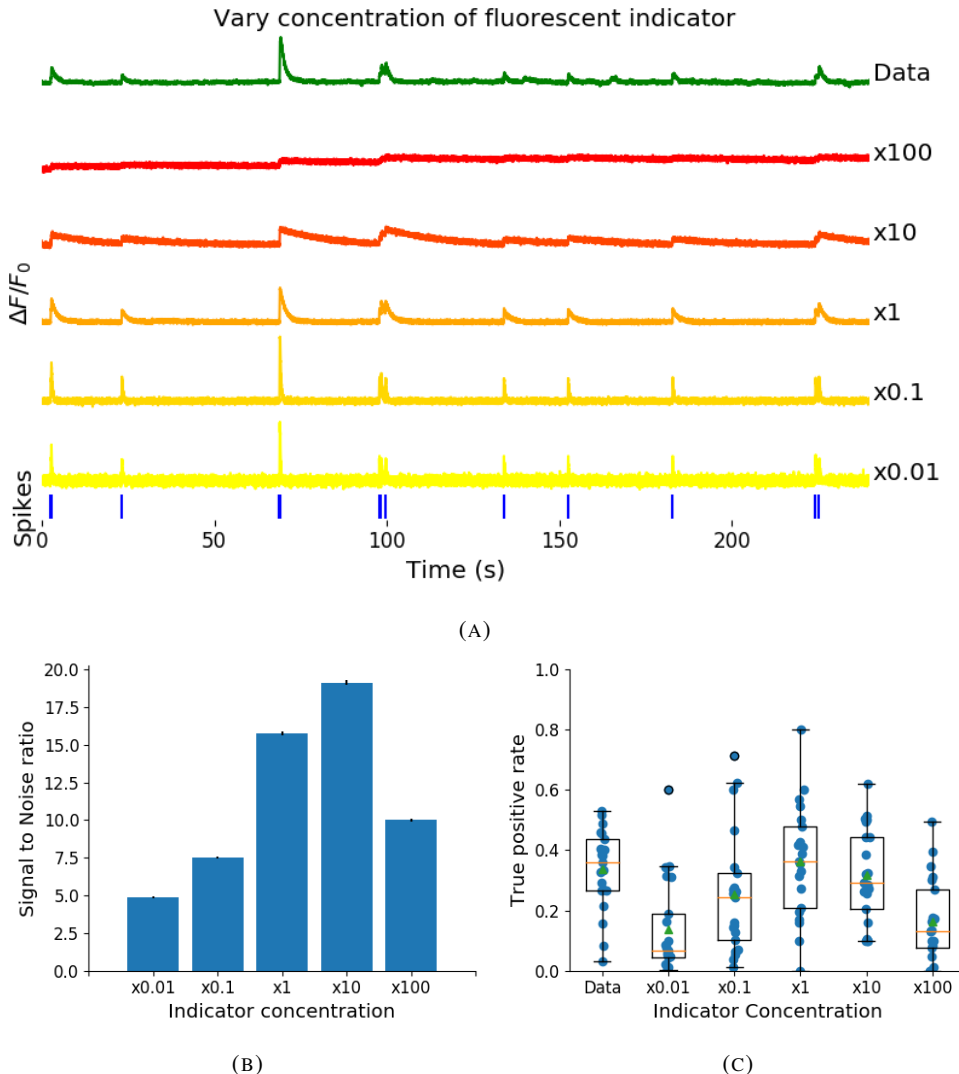


FIGURE 1.5: (a) An example trace for each of the five perturbed values for the concentration of fluorescent calcium indicator. The top two traces are produced by the lower perturbed values, the middle trace is produced by the experimental value, and the lowest two traces are produced when using the higher perturbed values. (b) The signal-to-noise ratio of the modelled fluorescence traces using each of the four perturbed values, and the experimental value. Extreme perturbations of the concentration either above or below the experimental level lowered the SNR. (c) The true-positive rates of the deconvolution algorithm's predictions when inferring from the observed data, and inferring from modelled traces using the perturbed and experimental values. We found that the algorithms performs equally badly on the two most extreme values, and performs equally well on the experimental value, and the next higher perturbed value.

to calcium, and variations in endogenous buffer concentration may affect GCaMP signal and therefore spike inference. To address this we varied the concentration of the endogenous buffer in the model neuron over five orders of magnitude from 0.8 to 8000 μM , simulated calcium fluorescence traces in response to the same set of spike trains, and performed spike inference on the resulting fluorescence time series. Increasing the endogenous buffer concentration had a substantial effect on the GCaMP fluorescence signal, both decreasing its amplitude and slowing its kinetics (figure 1.6(a)). This corresponded with a decrease in both single-spike signal-to-noise ratio (figure 1.6(b)) and spike inference accuracy (figure 1.6(c)). In contrast, decreasing endogenous buffer capacity from the fitted value had little effect on either the GCaMP signal or spike inference (figure 1.6).

1.2.5 Single spike inference accuracy drops for high firing rates, but firing rate itself can be estimated from mean fluorescence amplitude

The fluorescence signal recorded from neurons using calcium indicators is typically much slower than changes in membrane potential for two reasons: first, because the calcium and the indicator have slow binding and unbinding kinetics, the signal is a low-pass filtered version of the membrane potential. Second, neuronal two-photon imaging experiments are often performed in scanning mode, which limits their frame rate to $\sim 10\text{Hz}$ or slower. This implies that multiple spike events that occur close in time might be difficult to resolve from a calcium indicator time series. Many cells, especially several types of inhibitory interneurons, fire tonically at rates higher than 10Hz. We used the model to test whether spike inference accuracy depended on the neuron's firing frequency by driving the cell with spike trains sampled from a Poisson processes of varying frequency. We simulated a variable firing rate using an Ornstein-Uhlenbeck process, and simulated the spike trains using a Poisson distribution with its rate taken from this process. Because of the high frequency firing rate of these spike trains, we using the accuracy as the measure of spike inference quality. We simulated 30 spike trains at average firing rate of 1, 5, and 10Hz, and measured the spike inference quality of all these traces. Spike inference accuracy decreased with increasing firing rate, for up to 10Hz Poisson spike trains (figure 1.8(left)). Although, the accuracy remained above 90% for each of the three frequencies. We also plotted the average $\Delta F / F_0$ as a function of stimulation firing rate. We found that it increased monotonically as a function of firing rate (figure 1.8(right)).

We expected lower spike inference quality as the average spiking frequency increased. Since the fluorescence trace, in some sense, is a low pass filtered version of the spike train, a

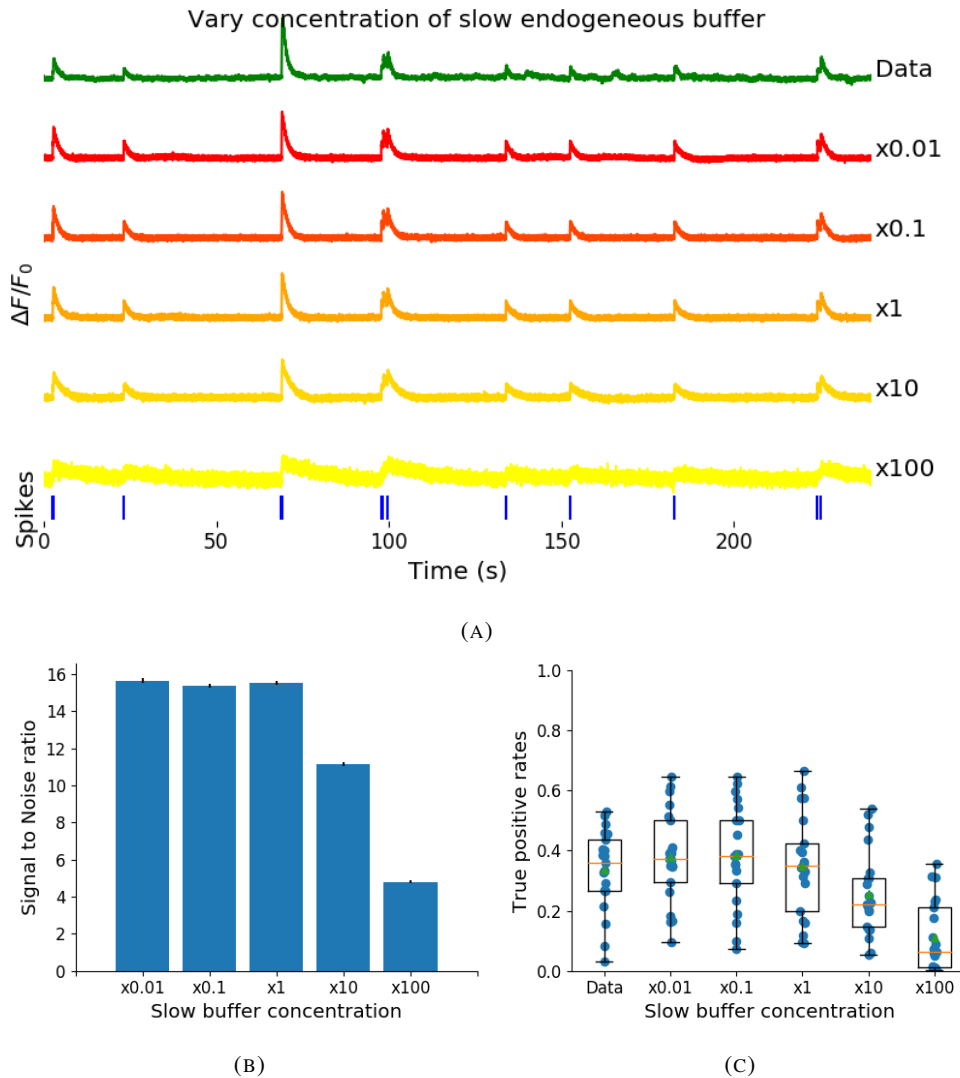


FIGURE 1.6: (a) An example trace for each of the five perturbed values for the concentration of immobile endogenous buffer. (b) The signal-to-noise ratio of the modelled fluorescence traces using each of the four perturbed values, and the experimental value. The lower values for the immobile buffer produce the same SNR as the experimental value. But the higher perturbed values produce fluorescence traces with a lower SNR. (c) The true-positive rates of the deconvolution algorithm's predictions when inferring from the observed data, and inferring from modelled traces using the perturbed and experimental values.

654 tightly packed groups of spikes will be more difficult to infer than isolated spikes. However,
 655 the increasing amplitude of the fluorescence trace with increasing frequency suggests that
 656 some spike inference algorithm could be developed based on this amplitude.

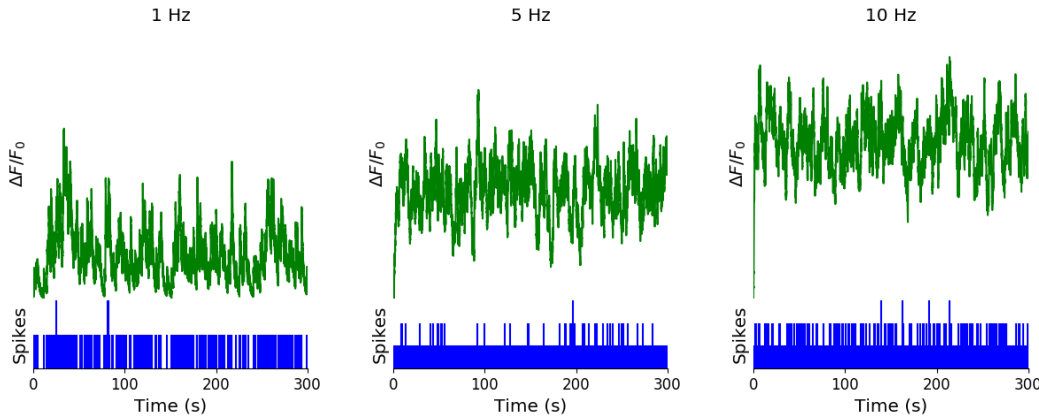


FIGURE 1.7: **Simulating fluorescence traces at different firing rates** Example modelled traces created using simulated spike trains with a mean firing rate of 1Hz (left column), 5Hz (middle column), and 10Hz (right column). Note the difference in amplitude with different mean firing rates.

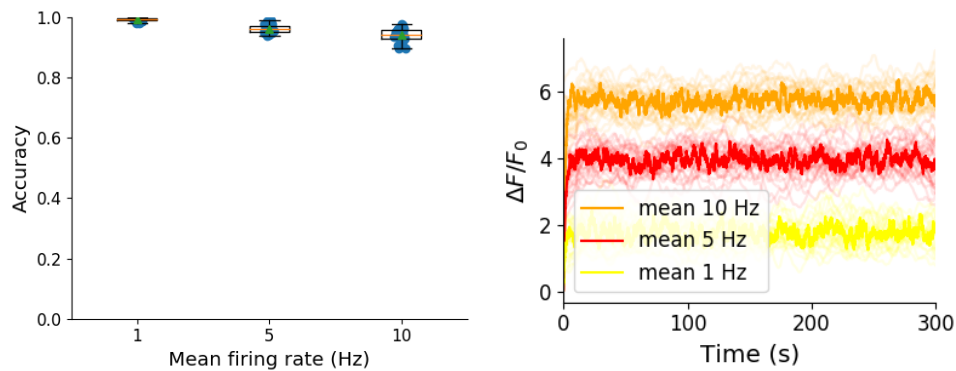


FIGURE 1.8: **Inference quality and $\Delta F/F_0$ vs Firing rate** (left) The spike inference accuracy when applied to 30 traces created using simulated spike trains with mean firing rates of 1, 5, and 10 Hz. (right) The mean $\Delta F/F_0$ across those 30 traces for each frequency.

657 1.3 Discussion

658 We designed a biophysical model for the changes in free calcium and bound calcium con-
 659 centrations within a cell soma with a fluorescent calcium indicator. We used this model to
 660 model the fluorescence trace resulting from a spike train in this cell. We fit the free parame-
 661 ters of the model by matching the power spectrum and amplitude of fluorescence traces with
 662 simultaneously measured spike trains. We inferred spikes from real fluorescence traces and

663 modelled fluorescence traces, and measured the quality of the spike inference in both cases.
664 We found that the spike inference quality was similar in both cases. We perturbed the concen-
665 tration of the calcium buffers in the model, and the binding/unbinding rates of those buffers
666 in the model, and measured the effect on the signal-to-noise ratio (SNR) of the modelled
667 fluorescence traces and the spike inference quality.

668 For the fluorescent calcium indicator, we found that any large perturbation away from
669 the experimental value led to a reduction in SNR, and spike inference quality. For the bind-
670 ing/unbinding rates, we kept the ratio of these rates constant, but altered their values in paral-
671 lel. The lower values caused a reduction in SNR, and a reduction in spike inference quality.
672 For the endogenous buffer concentration, an increase above the experimental value caused a
673 reduction in SNR and spike inference quality.

674 Although the model produced visually similar time series to the real data, there were a
675 few aspects it did not capture. First, the real data featured some low-frequency components
676 that did not appear related to the spike events. These were not captured by the models we
677 used in this study, but could be added in future by adding a suitable low-frequency term to the
678 resulting time series. Second, the real data seemed to have some nonlinearities not captured in
679 the model, for example the response to two nearby spikes was greater than expected from the
680 linear sum of two single spikes. This may be due to the co-operative binding of Calmodulin
681 to calcium, which gives calmodulin a supra-linear sensitivity to calcium concentration. The
682 model, in contrast behaved much more linearly, but could be extended in future to include
683 such nonlinearities. Third, in the real data the fluorescence peak amplitude seemed to vary
684 from spike to spike, even for well-isolated spike events. However in our model we assumed
685 each spike lead to the same fixed-amplitude injection of calcium to the cell, leading to much
686 greater regularity in fluorescence peak amplitudes. This variability could be added in future
687 versions of the model by making the injected calcium peak a random variable. Fourth, we
688 modelled the soma as a single compartment, but in reality there is likely a non-uniform spatial
689 profile of calcium concentration. This may matter because some endogenous buffers might
690 access calcium right as it influxes from the extracellular space, whereas the majority of the
691 fluorescence signal is more likely coming from the bulk of the cytoplasm. Future models
692 could attempt to model these spatial dependencies to assess whether they affect the overall
693 spike inference procedure.

694 As well as the optimised parameters, the model has 14 fixed parameters than can be
695 changed to simulate different types of calcium indicators. This model could be used to test
696 the theoretical performance of proposed new types of calcium indicator. The model could

697 also be used by developers of spike inference algorithms to test the effects of changing cal-
698 cium indicator parameters on spike inference, or to test the affects of changing spiking char-
699 acteristics on spike inference. For example, high firing rate vs low firing rate, or bursting vs
700 no bursting. Given the increasing amplitude of the fluorescence trace with increasing mean
701 firing rate, it would be possible to build a spike inference algorithm on this principle at least
702 in part.

703 Our model has already been used as a tool by our colleagues, for simulating fluorescence
704 traces in response to cells that can fire with a continuous rate between 10 and 20Hz, but do
705 not always do so. Our colleagues found that a combination of the amplitude and the variance
706 of the simulated fluorescence trace was the best indicator of firing rate. For example, when
707 a cell was not firing, the amplitude and variance of the fluorescence trace was relatively low.
708 When the cell fired with a low firing rate \sim 1Hz, the mean amplitude was still low but
709 the variance of the fluorescence trace was high, and for high firing rate \sim 10 – 20Hz, the
710 fluorescence amplitude was high, and the variance was low. In this way, our model may be
711 useful for investigating firing rates underlying real fluorescence traces in response to cells
712 which can fire in these rage ranges.

713 A recent paper by Greenberg et al (2018) described a biophysical model for spike train
714 inference called the ‘Sequential binding model’. Similar to our model, this model included
715 parameters for two types of endogenous buffer. But this model also included dynamics for
716 calcium binding to and unbinding from these endogenous buffers. Furthermore, this model
717 included dynamics for calcium binding to and unbinding from the four binding sites present
718 on a GCaMPs6 molecule. In the accuracy measurements specified in that paper, this model
719 performed better than the MLspike algorithm, which is also partially a biophysically model,
720 and it performed better than the constrained non-negative deconvolution algorithm. The se-
721 quential binding model also biophysically interpretable parameters, and its fitted parameters
722 for quantites such as buffering capacity and calcium influx upon action potential firing fall in
723 line with experimental values (Greenberg et al., 2018). Biophysical models like this appear
724 to be the way forward for spike inference algorithms.

725 1.4 Methods

726 1.4.1 Calcium dynamics model

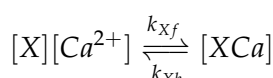
727 We wrote a biophysical model of the calcium dynamics within a cell soma. When a neu-
728 ron fires an action potential, voltage-dependent calcium ion-channels open up that allow a

current of Ca^{2+} to flow into the neuron (Koch, 1999). The increase in the free calcium ion concentration inside of the cell, along with changes in the concentration of potassium and sodium, causes the change in cell membrane potential, which must be depolarised. The depolarising process consists of free calcium ions leaving the cell through open ion channels, or binding to molecules within the cell called buffers, or calcium storage by organelles such as the endoplasmic reticulum. A diagram illustrating the cell, its channels, and its buffers can be seen in figure 1.1A. There are several different types of calcium buffer, each with different dynamics and different concentrations within different types of excitable cell. The fluorescent calcium indicator is another calcium buffer, with the useful property that when it is bound to a calcium ion, the bound molecule may become excited by a photon and release a photon in return. This is what creates the fluorescence. After the action potential has taken place, the free calcium concentration within the cell will return to a baseline level (Maravall et al., 2000).

We modelled the the dynamics of five molecular concentrations,

- Free calcium ion concentration, $[\text{Ca}^{2+}]$
- Fluorescent indicator bound calcium, $[\text{BCa}]$
- Endogenous mobile buffer bound calcium, $[\text{ECa}]$
- Endogenous immobile buffer bound calcium, $[\text{ImCa}]$
- Excited buffered calcium, $[\text{BCa}^*]$

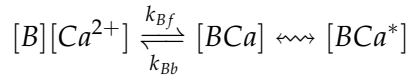
The term ‘buffering’ refers to free calcium ions coming into contact with buffer molecules and binding together. Diagrammatically:



where $[X]$ represents any buffer molecule, and k_{X_f} and k_{X_b} represent the binding and unbinding (dissociation) rates in units of per molar concentration per second ($\text{M}^{-1} \text{s}^{-1}$) and per second (s^{-1}) respectively. The speed of this chemical reaction is determined by the binding and unbinding rates.

There are a number different endogenous buffers in any neuron. Which buffers are present, and the buffers’ concentrations vary from cell to cell. In order to capture the effects of mobile and immobile endogenous buffers without introducing several parameters, they were modelled as two buffers. One representing mobile buffers and the other representing immobile buffers. Each with their own binding and unbinding rates.

The fluorescent calcium indicator behaves similarly to the other calcium buffers. The calcium is buffered by the indicator in the same way. But an indicator bound calcium molecule can become excited by absorbing the energy from a photon. An excited indicator bound calcium molecule can then release a photon to go back to its ‘relaxed’ state.



757 The released photons are captured by a photon collector. This gives us the fluorescence trace.

758 Ignoring the baseline level of free calcium in a neuron, the system of equations we used
759 to model all of these interactions is as follows:

$$\begin{aligned} \frac{d[Ca^{2+}]}{dt} = & k_{Bb}[BCa] + k_{Eb}[ECa] + k_{Imb}[ImCa] \\ & - k_{Bf}[B][Ca^{2+}] - k_{Ef}[E][Ca^{2+}] - k_{Imf}[Im][Ca^{2+}] \\ & + \beta([Ca_0^{2+}] - [Ca^{2+}]) \end{aligned} \quad (1.1)$$

$$\frac{d[BCa]}{dt} = k_{Bf}[B][Ca^{2+}] - k_{Bb}[BCa] + r[BCa^*] - e[BCa] \quad (1.2)$$

$$\frac{d[ECa]}{dt} = k_{Ef}[E][Ca^{2+}] - k_{Eb}[ECa] \quad (1.3)$$

$$\frac{d[ImCa]}{dt} = k_{Imf}[Im][Ca^{2+}] - k_{Imb}[ImCa] \quad (1.4)$$

$$\frac{d[BCa^*]}{dt} = \eta[BCa] - r[BCa^*] \quad (1.5)$$

760 where $[Ca_0^{2+}]$ is the baseline calcium concentration within the cell soma, β is a rate defining
761 how quickly free calcium enters or leaves the cell in the absence of an action potential, η
762 is the excitation rate for indicator bound calcium, r is the photon release rate for the excited
763 indicator bound calcium, and f and b are used to indicate the forward and backward rates
764 for chemical reactions respectively. The excitation rate defines the proportion of indicator
765 bound calcium that becomes excited at each time step. The photon release rate defines the
766 proportion of excited indicator bound calcium that releases a photon and returns to its relaxed
767 state at each time step. An action potential is modelled as a discontinuous increase in the free
768 calcium concentration to an appropriate value (Maravall et al., 2000).

769 Note that each of the three pairs of binding and unbinding terms in the first equation has a
770 corresponding pair in one of the subsequent three equations. Binding removes a free calcium
771 molecule and adds a bound calcium molecule, and unbinding does the opposite.

772 When using this model to simulate a fluorescence trace, the system of equations above are

773 first solved over a period of 25s without action potentials. This lets each of the five tracked
774 chemical concentrations reach their steady state. Then we use the given spike train and the
775 parameters to model the fluorescence trace.

776 Note that since the model has no spatial component, the mobile and immobile buffers
777 only differ in their binding and unbinding rates.

778 **Photon release & capture**

779 We used a simple model for the photon release. The number of photons released at each time
780 step was controlled by the number of excited indicator bound calcium molecules in the cell
781 and a parameter called the ‘release rate’. The release rate is an optimised free parameter of
782 the model.

783 As for the photon capture, in two-photon excitation microscopy the photons scattered
784 by the fluorescent indicator get scattered in all directions. Therefore the number of photons
785 detected is stochastic. This made the process for capturing photons the natural source of
786 noise in the system. The number of photons captured, and therefore the intensity of the
787 fluorescence, is modelled using a binomial distribution. The number of photons released was
788 used as the number of trials. The probability of success, or ‘capture rate’ was a free parameter
789 of the model that we optimised.

790 **1.4.2 Parameter optimisation**

791 The free parameters of the model are as follows:

792 **Calcium rate, β** Controls how quickly the concentration of free calcium will be driven to
793 the baseline concentration.

794 **Capture rate, p** The average proportion of photons captured by the photon detector.

795 **Excitation rate, η** The number of indicator bound calcium molecules that become excited
796 by photon bombardment at each time step.

797 **Release rate, r** The number of excited indicator bound calcium molecules that release a
798 photon at each time step.

799 To optimise the free parameters given a fluorescence trace, we applied the following proce-
800 dure:

- 801 1. The frequency power spectrum of the trace was measured.

802 2. The power spectrum was smoothed using a boxcar smoother (aka. sliding average, box
803 smoother).

804 3. The log of the smoothed power spectrum was measured.

805 4. Use the model to create a modelled fluorescence trace.

806 5. Apply steps 1, 2, and 3 to the modelled fluorescence trace.

807 6. Calculate the root mean squared difference between the log power of the actual fluo-
808 rescence trace, and the log power of the modelled fluorescence trace.

809 7. Calculate the root mean squared difference between the actual fluorescence trace and
810 the modelled fluorescence trace.

811 8. Use an optimisation algorithm to reapply this process, attempting to minimize the sum
812 of the two root mean squared differences at each iteration.

813 Using the root mean squared difference of the log power spectra as part of the objective
814 function forces the model to match the noise frequency of the actual fluorescence. Using
815 the root mean squared difference of the traces themselves forces the model to match the
816 amplitude of the fluorescence trace more accurately.

817 In order to minimise the objective function, a suite of meta-heuristic optimisation (aka.
818 black-box optimisation) algorithms were implemented on each of the traces in the dataset.
819 These methods were chosen because they don't require a gradient for the objective function
820 (gradient-free) and they are particularly useful for minimising stochastic objective functions
821 like the one we used here. The free parameters were optimised for each individual fluo-
822 rescence trace. The most successful method for each trace was recorded. The method that was
823 most often successful was probabilistic descent, and the second most successful method was
824 generating set search. Both of these methods are examples of pattern search. These two
825 methods were the best optimisers on about 75% of the traces in the dataset.

826 Although this optimisation procedure minimises the value of the optimisation function,
827 the value never reaches zero for a number of reasons. Firstly, the fluorescence traces carry low
828 frequency fluctuations that cannot be captured by the model. Secondly, the model assumes
829 that the process of calcium binding to the fluorescent indicator is linear in time (see equation
830 1), but there are more complicated dynamics involved here. Fluorescent calcium indicators
831 are often built upon the calcium binding protein called 'calmodulin'. This protein has four
832 calcium binding sites. These sites are locally split into two pairs. Each pair has a different

Parameter	Description	Value	Source
baseline	The baseline concentration of free calcium within the cell soma	$4.5 \times 10^{-8} \text{M}$	(Maravall et al., 2000)
cell radius	The radius of the soma (assumed to be spherical)	10^{-5}M	(Fiala and Harris, 1999)
endogenous	The concentration of endogenous mobile buffer within the cell soma	10^{-4}M	(Faas et al., 2011)
frequency	The frequency at which the spike trains are sampled.	100Hz	
immobile	The concentration of endogenous immobile buffer within the cell soma	$7.87 \times 10^{-5} \text{M}$	(Bartol et al., 2015)
indicator	The concentration of fluorescent indicator within the cell soma	10^{-4}M	(Maravall et al., 2000)
k_{Bb}	The unbinding rate of the fluorescent calcium indicator	160s^{-1}	(Bartol et al., 2015)
k_{Bf}	The binding rate of the fluorescent calcium indicator	$7.77 \times 10^8 \text{s}^{-1} \text{M}^{-1}$	(Bartol et al., 2015)
k_{Eb}	The unbinding rate of the endogenous mobile buffer	10^4s^{-1}	(Bartol et al., 2015)
k_{ef}	The binding rate of the endogenous mobile buffer	$10^8 \text{s}^{-1} \text{M}^{-1}$	(Bartol et al., 2015)
k_{Imb}	The unbinding rate of the endogenous immobile buffer	524s^{-1}	(Bartol et al., 2015)
k_{Imf}	The binding rate of the endogenous immobile buffer	$2.47 \times 10^8 \text{s}^{-1} \text{M}^{-1}$	(Bartol et al., 2015)
peak	The increase in free calcium concentration within the cell induced by an action potential	$2.9 \times 10^{-7} \text{M}$	(Maravall et al., 2000)

TABLE 1.1: **Fixed parameters** A table of the parameters fixed before optimising the model. The values of these parameters could be changed to model different fluorescent calcium indicators.

833 affinity for calcium, and the affinity of the binding sites is affected by the occupancy of
 834 the other binding sites (Kilhoffer et al., 1992). So the calcium to calcium indicator binding
 835 process is non-linear, but the model does not take this into account.

836 Fixed parameters

837 As well as the optimised parameters mentioned in section 1.4.2, the model also has thirteen
 838 fixed parameters. Please see table 1.1 for details of these parameters and their values. In
 839 an application of the model, these parameters can be changed in order to model any given
 840 fluorescent calcium indicator.

841 **1.4.3 Julia**

842 The programming language used to write and execute the model was ‘Julia’. Julia is a dy-
843 namic programming language designed for technical computing. Julia was designed specif-
844 ically to provide a convenient high-level dynamic language similar to MATLAB, or Python,
845 with improved performance. Julia’s type system and Julia’s direct interfaces with C and
846 Fortran allow this aim to be achieved (Bezanson et al., 2012). The Julia version of the
847 ‘Sundials’ package for ODE solving was used to solve the system of equations above. The
848 BlackBoxOptim.jl package for Julia was used to perform the optimisation.

849 **1.4.4 Spike inference**

850 We used spike inference algorithms to compare the quality of spike inference using the mod-
851 eled traces to the quality of spike inference using the observed traces. We also used the
852 spike inference algorithms to assess the effect of parameter perturbation on the spike infer-
853 ence. Three algorithms were used:

854 **Constrained non-negative deconvolution algorithm (aka Pnevmatikakis algorithm)** This
855 algorithm uses a constrained version of non-negative Weiner deconvolution to infer a
856 calcium signal and a ‘spiking activity signal’ from the fluorescence trace (Vogelstein
857 et al., 2010; Pnevmatikakis et al., 2016). The spiking activity signal is a non-negative
858 vector of real numbers reflecting the cell’s activity rather than an actual spike train. We
859 inferred a spike train by choosing an optimised threshold for the spiking activity sig-
860 nal. Whenever the spiking activity signal exceeded that threshold, an action potential
861 was inferred. The threshold was optimised by minimising the difference between the
862 number of spikes observed and the number of spikes predicted.

863 **ML-Spike algorithm** This algorithm uses a generalised version of the Viterbi algorithm to
864 return the spike train that maximises the likelihood of producing the given fluorescence
865 trace. The Viterbi algorithm is an algorithm for estimating the most likely sequence of
866 hidden states resulting in a sequence of observed states in a discrete-time finite-state
867 Markov process (**forney**). In this case, each hidden state is defined by the presence or
868 absence of an action potential, and each observed state is the value of the fluorescence
869 trace at each time step. This algorithm assumes that the concentration of calcium
870 within the cell will decay to a drifting baseline, rather than a fixed baseline (Deneux
871 et al., 2016).

872 **Online Active Set method to Infer Spikes (OASIS)** This algorithm is once again based on
873 an auto-regressive model of the fluorescence trace, but can be generalised to any or-
874 der. The algorithm itself is a generalisation of the pool adjacent violators algorithm
875 (PAVA) that is used in isotonic regression. The OASIS algorithm works through the
876 fluorescence trace from beginning to end, this combined with the speed of the algo-
877 rithm means that it could be used for real-time online spike inference (Friedrich and
878 Paninski, 2016). Given a fluorescence trace, the algorithm will return the most likely
879 spike train and an inferred denoised fluorescence signal.

880 In order to quantify the quality of spike inference for a given algorithm, we ran that algorithm
881 on all of the fluorescence traces in dataset number eight of the spike finder datasets. Then we
882 measured some binary classification measures on the results. These measures included

- 883 • Accuracy
- 884 • True positive rate (aka recall, sensitivity, hit rate)
- 885 • True negative rate (aka specificity)
- 886 • Precision
- 887 • Negative predicted value
- 888 • False negative rate (aka miss rate)
- 889 • False positive rate (aka fall-out)
- 890 • False discovery rate
- 891 • False omission rate

892 In making these measurements, we allowed a tolerance of two subsequent time bins for spike
893 prediction. For example, the spike train data is a vector of 0s and 1s, with one element for
894 each time bin. A ‘0’ denotes inactivity, a ‘1’ denotes the presence of at least one action
895 potential. The inferred spike trains produced by the spike inference algorithms take the same
896 form. In our analysis, if a spike appeared in the inferred spike train up to two time frames
897 after a spike in the observed spike train, that spike was considered correctly inferred i.e. a true
898 positive. However, once a spike in the inferred spike train was matched to a spike from the
899 observed spike train, the inferred spike could not be matched to another observed spike. To
900 illustrate, if two spikes were inferred in the two time bins following an isolated observed

901 spike, the first inferred spike was considered correctly inferred, but the second inferred spike
902 was considered incorrectly inferred, i.e. a false positive.

903 The most useful measure was the true positive rate. This is because the spiking is sparse
904 and this measurement is sensitive to the number of spikes observed and inferred, but is not
905 affected by the true negative or false negative rates. After optimising the parameters for each
906 fluorescence trace we measured the spike inference quality for the observed fluorescence
907 traces, and compared this to the spike inference quality for the modelled traces.

908 When measuring the spike inference quality for higher frequency spike train (1 – 10Hz),
909 we used the accuracy as our binary classification measure. At these frequencies the variance
910 of the fluorescence trace was much higher than for sparser spiking regimes, therefore we
911 wanted to take into account the number of false negatives inferred by the algorithm.

912 **Comparing spike inference quality**

913 In order to compare spike inference quality we had to use methods for comparing samples.
914 When comparing the true positive rate distributions arising from two different datasets, or
915 two different algorithms on the same dataset, we compared the distributions using a paired
916 t-test.

917 **1.4.5 Perturbation analysis**

918 In order to measure the sensitivity of spike inference to changes in a given model parameter,
919 we perturbed the parameter and compared the quality of spike inference with the perturbed
920 parameters to the quality of spike inference with the experimental or optimised parameters.
921 In order to maximise the possibility of observing a difference due to the perturbation, we
922 perturbed the chosen parameter by a relatively large amount. For example, the experimen-
923 tal value for the molar concentration of the fluorescent indicator within the cell was 10^{-4}M
924 (Maravall et al., 2000). The perturbed values used for this parameter were 10^{-2}M , 10^{-3}M ,
925 10^{-5}M , and 10^{-6}M . The quality of the inference was compared by measuring the true posi-
926 tive rate for each perturbed value and using a t-test to compare the distributions of the results.

927 This analysis was performed firstly without any optimisation of the free parameters for
928 use with the perturbed parameters. Then the analysis was performed after the optimised
929 parameters for each perturbed value were calculated.

930 **1.4.6 Signal-to-noise ratio**

931 To assess the effect of perturbation on the modelled traces, we measured and compared the
932 signal to noise ratio (SNR) on each of the modelled traces. We calculated the SNR as the
933 peak change in fluorescence divided by the standard deviation of the baseline fluctuation of
934 the fluorescence trace (Tada et al., 2014). We measured these values by running the model
935 on a spike train consisting a long period of inactivity followed by one action potential. We
936 ran the model on this spike train one hundred times. We then measured the mean change
937 in fluorescence and standard deviation of baseline activity across the one hundred modelled
938 fluorescence traces, and calculated the SNR.

939 **1.4.7 Data sources**

940 All of the data used in this project was sourced from the ‘Spike Finder’ project (spikefinder.codeneuro.org).
941 The data consisted of a collection of datasets with simultaneously measured fluorescence
942 traces and action potentials (Berens et al., 2018).

⁹⁴³ **Chapter 2**

⁹⁴⁴ **Functional networks expand across
anatomical boundaries as correlation
time-scale increases**

⁹⁴⁵

⁹⁴⁶

947

UNIVERSITY OF BRISTOL

948

Abstract

949

Engineering

950

Department of Computer Science

951

Doctor of Philosophy

952

Investigating, implementing, and creating methods for analysing large neuronal ensembles

954

by Thomas J. DELANEY

955

Decades of research has established that correlated spiking plays a crucial role in representing sensory information. One drawback associated with the recent improvement in recording technology and consequent large datasets is the difficulty in analysing higher order correlations in large neuronal ensembles. One benefit of these datasets that has not yet been explored is the opportunity to compare correlations within anatomical regions to correlations across anatomical regions. In this work, we measured correlations between neurons residing in nine different brains regions in three awake and behaving mice. Using the these correlation measurements, we created weighted undirected graph networks and applied network science methods to detect functional communities in our neural ensembles. We compared these functional communities to their anatomical distribution. We repeated the analysis, using different timescales for our correlation measurements, and found that functional communities were more likely to be dominated by neurons from a single brain region at shorter timescales (< 100ms).

968 2.1 Introduction

969 Decades of research has established that correlations play a crucial role in representing sen-
970 sory information. For example, the onset of visual attention has been shown to have a greater
971 affect on the correlations in the macaque V4 region than on the firing rates in that region
972 (Cohen and Maunsell, 2009). Recent findings show that spontaneous behaviours explain cor-
973 relations in parts of the brain not associated with motor control (Stringer et al., 2019), that
974 satiety state appears to have a brain wide representation (Allen et al., 2019), and that subject
975 exploratory and nonexploratory states are represented in the amygdala (Gründemann et al.,
976 2019). So, behavioural states are likely represented across many regions of the brain, not just
977 motor related areas. In order to understand the brain, we must understand the interactions
978 between neurons and regions.

979 Because of limitations in recording technology almost all research has explored corre-
980 lations between neurons within a given brain region, or within only two regions at most
981 (Wierzynski et al., "2009"; Patterson et al., 2014; Girard, Hupé, and Bullier, 2001). Rel-
982 atively little is known about correlations between neurons in many different brain regions.
983 However, the recent development of ‘Neuropixels’ probes (Jun et al., 2017) has allowed
984 extracellular voltage measurements to be collected from multiple brain regions simultane-
985 ously routinely, and in much larger numbers than traditional methods. In this project we
986 used a publicly-available Neuropixels dataset to analyse correlations between different brain
987 regions (Stringer et al., 2019).

988 A drawback associated with the improvement in recording technology is an increase in
989 the difficulty in analysing these data. For example, analysing the i th order interactions of
990 N neurons generally requires estimation of N^i parameters. A number that becomes astro-
991 nomical for large N . New methods are required for analysing these new large datasets. We
992 attempted to address this requirement in this piece of research by applying a cutting-edge
993 network science community detection method to neural data.

994 Another unexplored area of research is the changes in cell interactions at different timescales.
995 Studies have shown different timescales for fluctuations in spiking activity (Murray et al.,
996 2014), and different time scales for event representation (Baldassano et al., 2017) across dif-
997 ferent brain regions. Still most studies focus on quantifying interactions at a given timescale.
998 But neurons may interact differently, or may interact with different neurons at different
999 timescales. Here we explore correlated communities of neurons at different timescales.

1000 In this work, we measured correlations between binned spike counts from neurons from

1001 nine different regions of the mouse brain. These measurements induced a weighted undi-
1002 rected graph or network where each neuron is represented by a node, and the strength of
1003 the connection between these nodes/neurons is the strength of the correlation between their
1004 spike counts. We then applied newly invented network methods (Humphries et al., 2019)
1005 to this network to find any community structure, and place the neurons in these correlation
1006 based communities. Finally, we compared these functional communities to the anatomical
1007 membership of the neurons.

1008 To investigate the functional communities and their relationship with anatomy at different
1009 time scales, we repeated these analyses using different length bin widths when binning spike
1010 times.

1011 To find and analyse functional networks while controlling for the subject's behaviour, we
1012 conditioned the binned spike counts on data from a video of the subject's face, and repeated
1013 our analysis for spike count correlations (or noise correlations) and signal correlations.

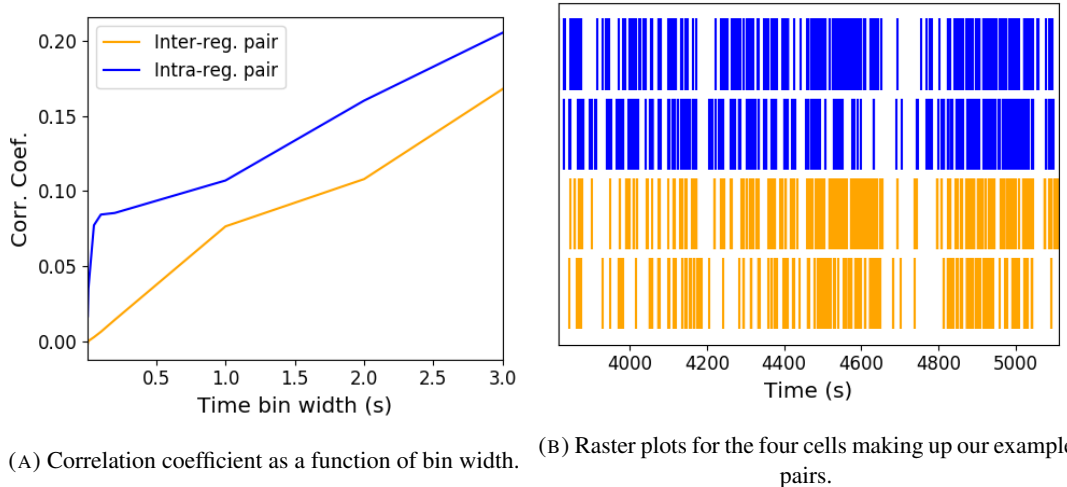
1014 **2.2 Results**

1015 Note that in the following text, we refer to the correlation coefficient between two sequences
1016 of spike counts from two different cells as the *total correlation*. We refer to the correlation
1017 between spike counts in response to a certain stimulus as the *spike count correlation* aka
1018 *noise correlation*, and we refer to the correlation between mean or expected responses to
1019 different stimuli as the *signal correlation* (Cohen and Kohn, 2011).

1020 The nine different brain regions from which we had data were the caudate putamen (CP),
1021 frontal motor cortex (FrMoCtx), hippocampus (HPF), lateral septum (LS), midbrain (MB),
1022 primary visual cortex (V1), superior colliculus (SC), somatomotor cortex (SomMoCtx), and
1023 thalamus (TH).

1024 **2.2.1 Average correlation size increases with increasing time bin width**

1025 First we inspected the affect of time bin width on total correlations. We know that using short
1026 time bins results in artificially small correlation measurements (Cohen and Kohn, 2011), so
1027 we expected to see an increase in correlation amplitude with increasing time bin width. That
1028 is exactly what we observed. Taking 50 cells at random, we calculated the total correla-
1029 tion between every possible pair of these cells, using different time bin widths ranging from
1030 0.005s to 3s. We found that the longer the time bin width, the greater the correlations (see
1031 figure 2.2a).



(A) Correlation coefficient as a function of bin width. (B) Raster plots for the four cells making up our example pairs.

FIGURE 2.1: (A) An example of the correlation coefficients between two different pairs of cells, one where both cells are in the same brain region (intra-regional pair), and one where both cells are in different brain regions (inter-regional pair). The correlation coefficients have been measured using different time bin widths, ranging from 5ms to 3s. Note the increasing amplitude of the correlations with increasing bin width. (B) A raster plot showing the spike times of each pair of cells.

1032 We also separated the positively correlated pairs from the negatively correlated pairs
 1033 using the mean correlation of each pair across all bin widths (see section 2.5.2). We found
 1034 that the positively correlated pairs become more positively correlated with increasing time bin
 1035 width, and the negatively correlated pairs become more negatively correlated with increasing
 1036 time bin width (see figures 2.2b and 2.2c).

1037 In figure 2.1a we plot correlations from two example pairs, one pair from within a region,
 1038 and one pair between regions. It can be seen that the correlation coefficient increases with
 1039 bin width. The correlations can be observed by eye in the raster plot for these cells in figure
 1040 2.1b.

1041 When taking the mean across all pairs, the positively correlated pairs dominate in terms
 1042 of both number of pairs, and amplitude of correlations. Therefore the mean across all pairs
 1043 is positive.

1044 These results were observed in each of the three mouse subjects from which we had data.

1045 2.2.2 Goodness-of-fit for Poisson and Gaussian distributions across increasing 1046 time bin widths

1047 We wanted to investigate if the width of the time bin used to bin spike times into spike counts
 1048 had an effect on the distribution of spike counts. We used the χ^2 statistic as a goodness-of-fit
 1049 measure for Poisson and Gaussian (normal) distributions to the spike count of 100 randomly

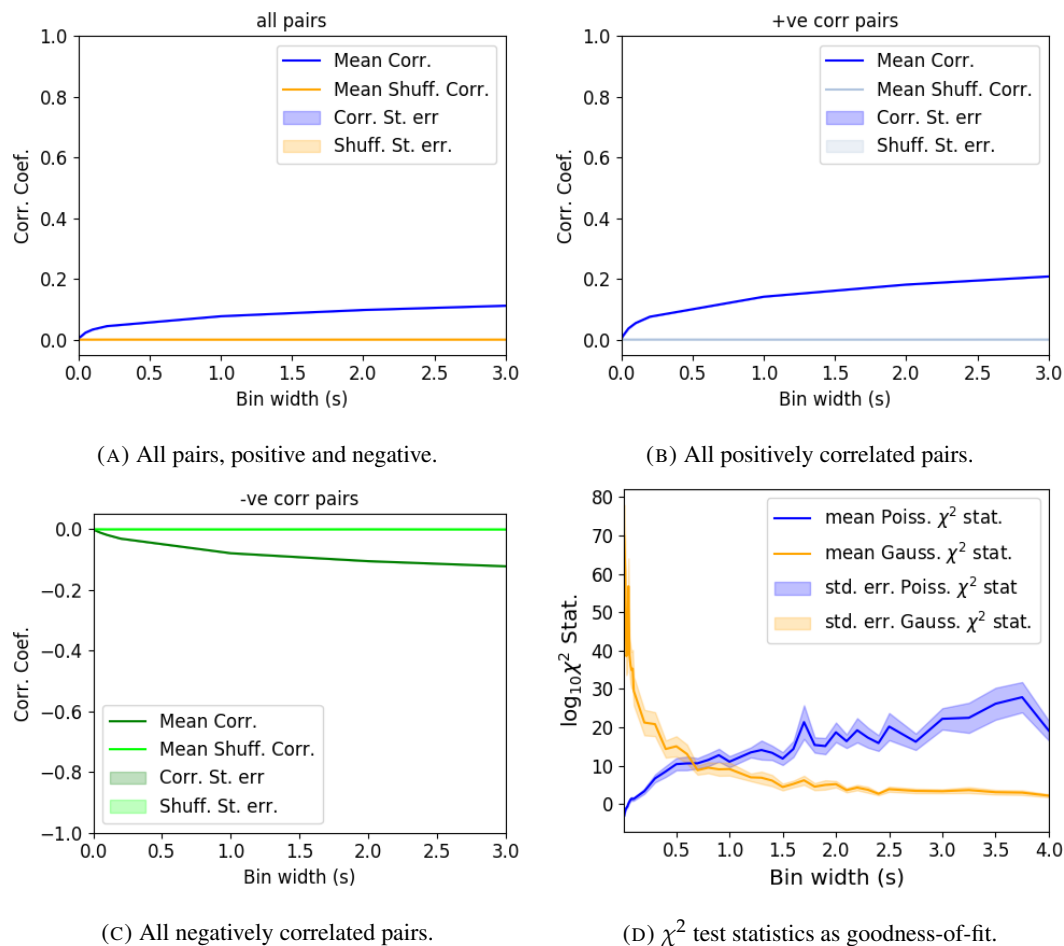


FIGURE 2.2: Mean correlation coefficients measured from pairs of 50 randomly chosen neurons. (A) All possible pairs, (B) positively correlated pairs, and (C) negatively correlated pairs. (D) Mean and standard error of χ^2 test statistics for Poisson and Gaussian distributions fitted to neuron spike counts.

1050 chosen neurons for a number of bin widths ranging from 0.01s to 4s. For the χ^2 statistic, the
1051 higher the value, the worse the fit.

1052 We expected a Poisson distribution to be a better fit for shorter time bin widths because
1053 spike counts must be non-negative, therefore any distribution of spike counts with mass dis-
1054 tributed at or close to 0 will be skewed. The distribution of spike counts is more likely to be
1055 distributed close to 0 when the time bin widths used to bin spike times into spike counts are
1056 small relative to the amount of time it takes for a neuron to fire an action potential ($\sim 1\text{ms}$ in
1057 the case of non-burst firing neurons).

1058 We expected a Gaussian distribution to be a better fit for longer time bin widths, because
1059 a Poisson distribution with a large rate is well approximated by a Gaussian distribution with
1060 mean and variance equal to the Poisson rate. Therefore, a Gaussian distribution would ap-
1061 proximate the mean of a collection of large spike counts, and have more flexibility than a
1062 Poisson distribution to fit the variance.

1063 We found that that a Poisson distribution is the best fit for shorter time bins less than 0.7s
1064 in length. Then a Gaussian distribution is a better fit for time bins greater than 0.7s in length
1065 (see figure 2.2d).

1066 **2.2.3 Differences between and inter- and intra- regional correlations decrease 1067 with increasing bin width**

1068 We investigated the differences in distribution between inter-regional correlations, i.e. corre-
1069 lations between neurons in different brain regions, and intra-regional correlations, i.e. corre-
1070 lations between neurons in the same brain region.

1071 Firstly, we investigated these quantities for all possible pairs of ~ 500 neurons taken
1072 from across all the 9 brain regions from which we had data. We distributed these neurons as
1073 evenly as possible across all of the regions, so that cells from one region would not dominate
1074 our data. We observed that the mean intra-regional correlations were always higher than the
1075 mean inter-regional correlations for every value of time bin width used. We also observed
1076 that as the time bin width increased these mean correlations increased and the difference
1077 between the mean inter-regional and intra-regional correlations grew (see figure 2.3 (Left)).

1078 Stringer et al. (2019) had a similar finding using the same data. They used only one value
1079 for the time bin width, 1.2s. Using this time bin width to bin spike times and measure total
1080 correlations, they found that the mean ‘within-region’ correlations were always greater than
1081 the ‘out-of-region’ correlations (Stringer et al., 2019). The figure from thier paper showing
1082 this result can be seen in figure 2.3 (Right).

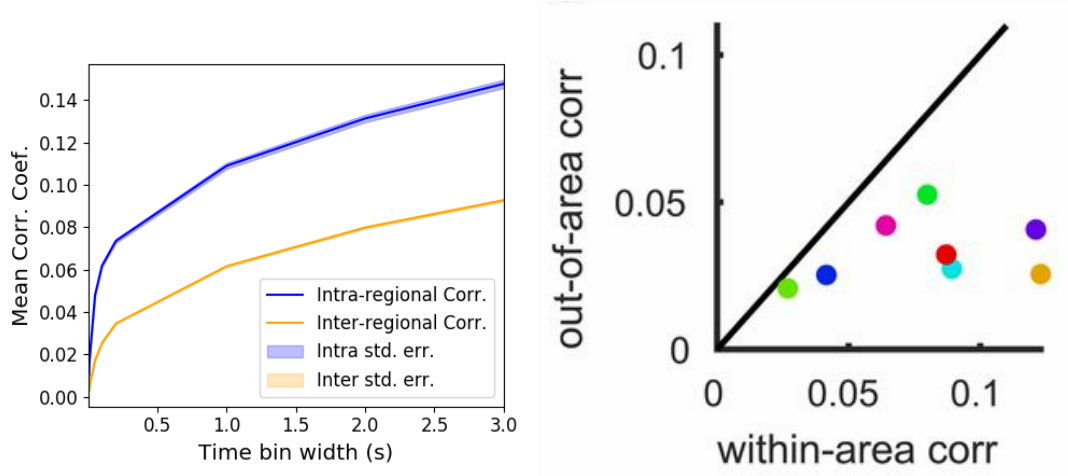


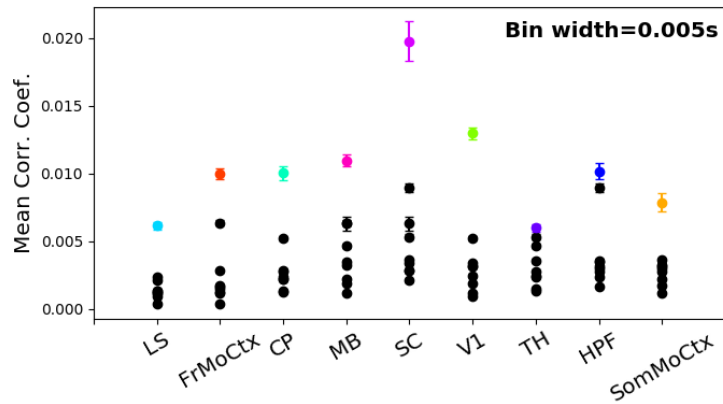
FIGURE 2.3: (Left) The mean intra-region and inter-region correlations using all possible pairs of ~ 500 neurons, spread across 9 different brain regions. (Right) Courtesy of Stringer et al. (2019), mean inter-regional (out-of-area) correlation coefficients vs mean intra-regional (within-area) correlation coefficients for a bin width of 1.2s. Note that the intra-regional coefficients are higher in each case.

1083 Examples of the correlations of one intra-regional pair and one inter-regional pair can be
1084 seen in figure 2.1.

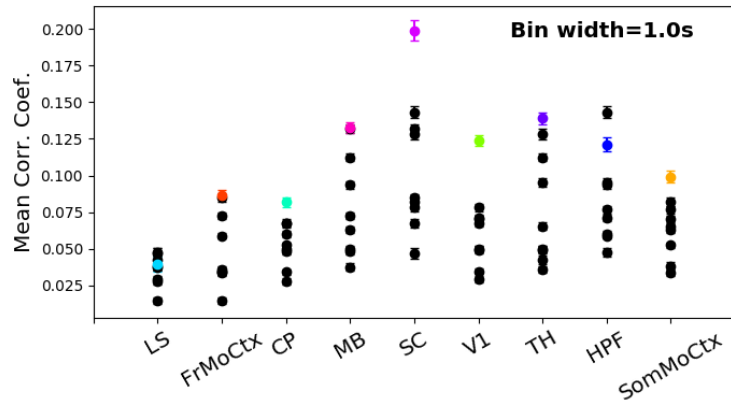
1085 Secondly, we separated those pairs into intra-regional and inter-regional groups. We
1086 noted that the mean intra-regional correlations (coloured dots in figures 2.4a and 2.4b) for
1087 a given region tended to be higher than the mean inter-regional correlations (black dots in
1088 figures 2.4a and 2.4b) involving cells from that region. However, in contrast with our previous
1089 result, we noted that the difference between the mean intra-regional correlations and most
1090 highly correlated inter-regional correlations reduced as we increased the time bin width (see
1091 figures 2.4a and 2.4b). This shows that the mean correlations shown in figure 2.3 are not
1092 distributed evenly across all region pair combinations.

1093 Finally, to see these regional mean correlations in a bit more detail, to examine the indi-
1094 vidual pair combinations in particular, we displayed these data in a matrix of mean corre-
1095 lations (see figure 2.5), showing the mean intra-regional correlations on the main diagonal, and
1096 the mean inter-regional correlations off diagonal. Comparing a version of this figure created
1097 using a short time bin width of 5ms (figure 2.5a) and a version using a longer time bin width
1098 of 1s (figure 2.5b) we observed that the mean intra-regional correlations are always relatively
1099 high in comparison to the mean inter-regional correlations, but the mean correlations in some
1100 inter-regional pairs are relatively much higher when using the longer time bin width.

1101 This could indicate information being processed quickly at a local or within-region level,
1102 and the local representations of this information spreading between regions at longer timescales.

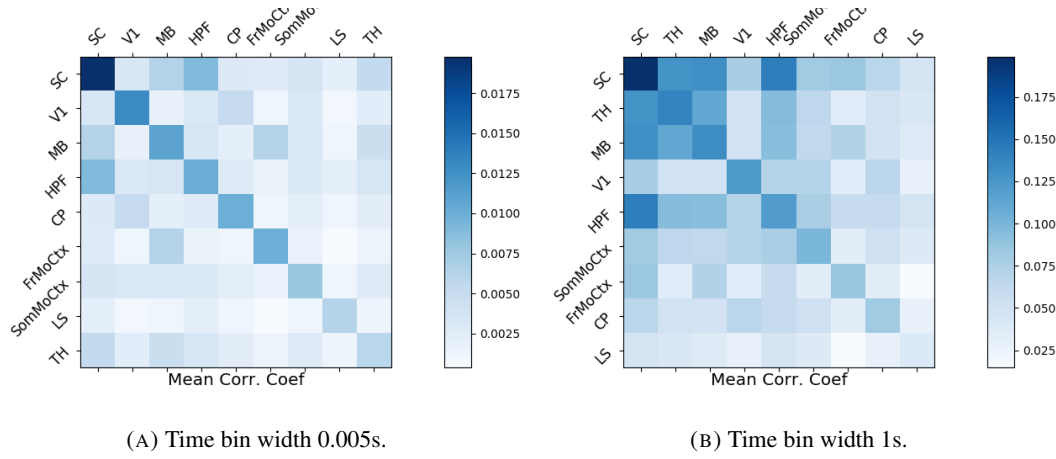


(A) Mean inter-regional and intra-regional correlations using a time bin width of 5ms.



(B) Mean inter-regional and intra-regional correlations using a time bin width of 1s.

FIGURE 2.4: The mean intra-regional correlations (coloured dots) and mean inter-regional correlations (black dots) for a given region, indicated on the x-axis, for different time bin widths. Each black dot represents the mean inter-regional correations between the region indicated on the x-axis and one other region. (A) shows these measurements when we used a time bin width of 5ms. (B) shows these measurements when we used a time bin width of 1s. Note that the difference between the mean inter-regional correlations and mean intra-regional correlations is smaller for 1s bins.



(A) Time bin width 0.005s.

(B) Time bin width 1s.

FIGURE 2.5: Mean inter-regional (main diagonal) and intra-regional (off diagonal) correlation coefficients. (A) Shows these measurements when spike times were binned using 5ms time bins. (B) Shows the same, using 1s time bins. Note that the matrices are ordered according to the main diagonal values, therefore the ordering is different in each subfigure.

1103 These results were consistent across the three mouse subjects. But, the relative magnitudes
 1104 of the mean intra-regional and inter-regional correlations were not consistent. For ex-
 1105 ample, the region with the highest mean intra-regional correlations when using 1s bin widths
 1106 for subject one is the superior colliculus (SC), but for subject two it is the midbrain (MB).

1107 **2.2.4 Connected and divided structure in correlation based networks reduces
 1108 in dimension with increasing bin width**

1109 We used the correlation measurements to create weighted undirected graphs/networks where
 1110 each node represents a neuron, and the weight of each edge is the pairwise correlation be-
 1111 tween those neurons represented by the nodes at either end of that edge. We aimed to find
 1112 communities of neurons within these networks, and compare the structure of these commu-
 1113 nities to the anatomical division of those neurons. The first step of this process involved
 1114 applying the ‘spectral rejection’ technique developed by Humphries et al (2019) (Humphries
 1115 et al., 2019). This technique compares our data network to a chosen null network model, and
 1116 finds any additional structure in the data network beyond that which is captured in the null
 1117 network model (if there is any such structure).

1118 By comparing the eigenspectrum of the data network to the eigenspectrum of many sam-
 1119 ples from the null network model, this technique allows us to estimate the dimensionality of
 1120 the additional structure in the data network, and gives us a basis for that vector space. It also
 1121 divides the additional structure into connected structure, and k -partite (or divided) structure.
 1122 For example, if our algorithm found two dimensions of additional connected structure, and

1123 one dimension of additional divided structure. We might expect to find three communities,
1124 that is groups more strongly connected within group than without, and we might expect to
1125 find bi-partite structure, that is two sets that are more strongly connected between groups
1126 than within groups.

1127 The technique also finds which nodes contribute to this additional structure, and divides
1128 our data network into signal and noise networks. The details of spectral rejection and node
1129 rejection can be found in sections 2.5.5 and 2.5.5 respectively, and a full overview can be
1130 found in (Humphries et al., 2019).

1131 We chose the sparse weighted configuration model (see section 2.5.5) as our null network
1132 model. This model matches the sparsity and the total weight of the original network but
1133 distributes the weight at random across the sparse network.

1134 We applied the spectral rejection method to our networks based on total correlations using
1135 different values for the time bin width. We observed that for smaller time bin widths, our data
1136 networks had both k -partite structure, and community structure. As the width of the time bin
1137 increased, we found that the k -partite structure disappeared from our data networks, and the
1138 dimension of the community structure reduced in two of the three mice from which we had
1139 data (see figure 2.6).

1140 2.2.5 Detecting communities in correlation based networks

1141 We applied the community detection procedure described in section 2.5.5 to our signal net-
1142 works for our various time bin widths. We detected a greater number of smaller communities
1143 at shorter time bin widths, and a smaller number of larger communities for longer time bin
1144 widths (see figure 2.7). This was expected after the results found in section 2.2.4. We found
1145 more dimensions of additional structure at shorter time bin widths, therefore we found more
1146 communities at shorter time bin widths.

1147 We also noticed that at short time bin widths the communities detected tended to be
1148 dominated by cells from one region. Whereas communities existing in networks created
1149 using wider time bin widths tended to contain cells from many different brain regions. More
1150 on this in the next section.

1151 2.2.6 Functional communities resemble anatomical division at short timescales

1152 In order to quantify the similarity of the communities detected to the anatomical division of
1153 the cells. We treated both the anatomical division and the communities as clusterings of these
1154 cells. We then used measures for quantifying the difference or similarity between clusterings

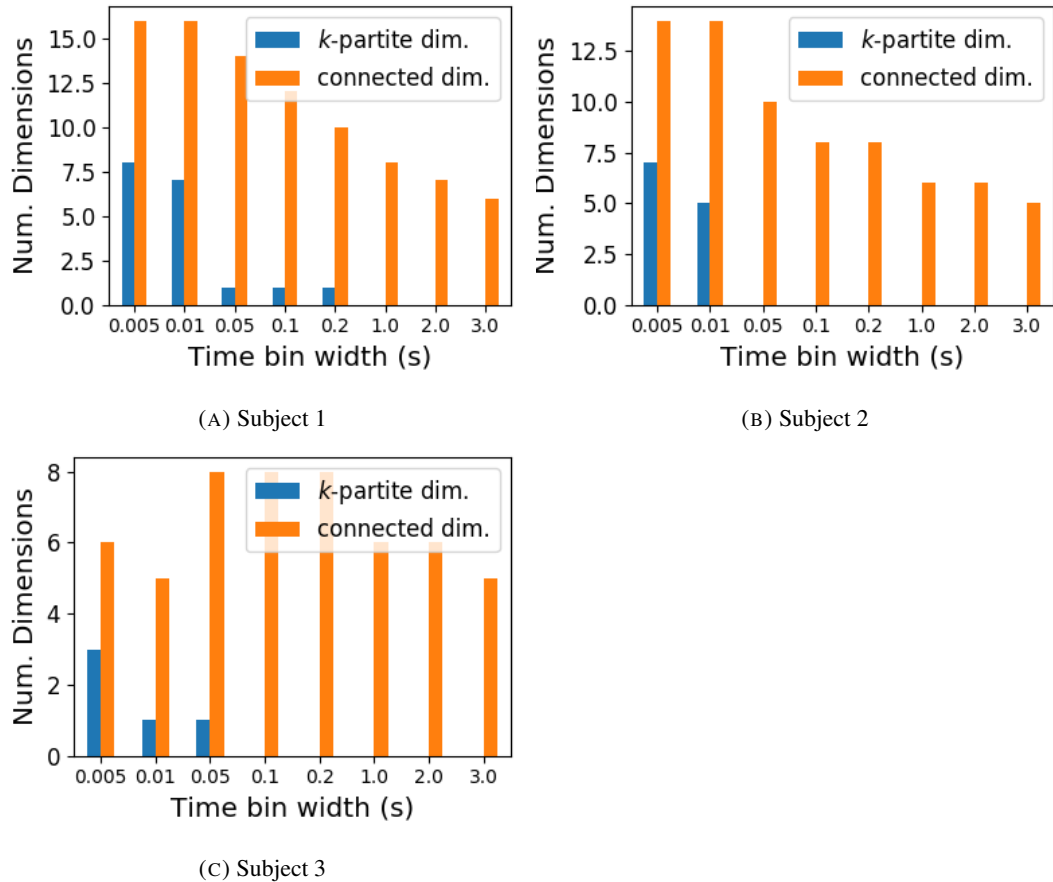


FIGURE 2.6: The number of dimensions in the *k*-partite and connected structure in the correlation based networks beyond the structure captured by a sparse weighted configuration null network model (see section 2.5.5), shown for different time bin widths. Note that the *k*-partite structure disappears for time bin width greater than 200ms for all three subjects. The dimension of the connected structure reduces with increasing bin width for 2 of the 3 subjects (top row).

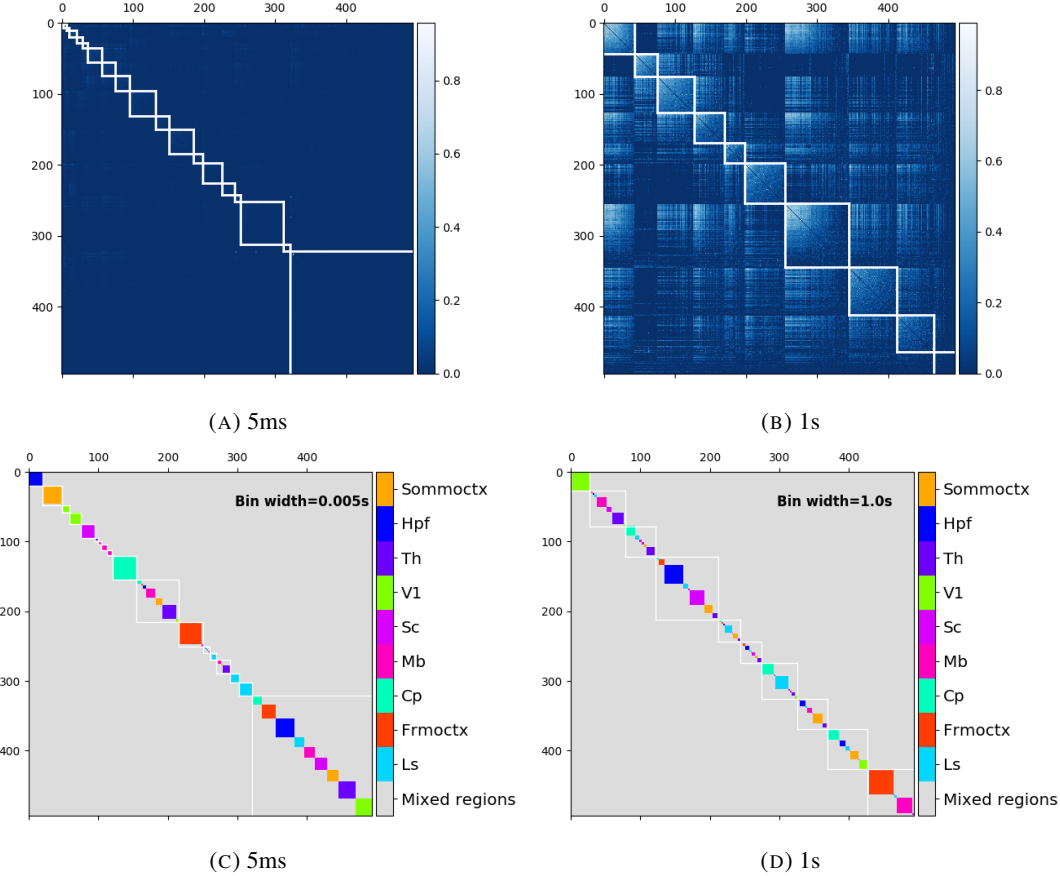


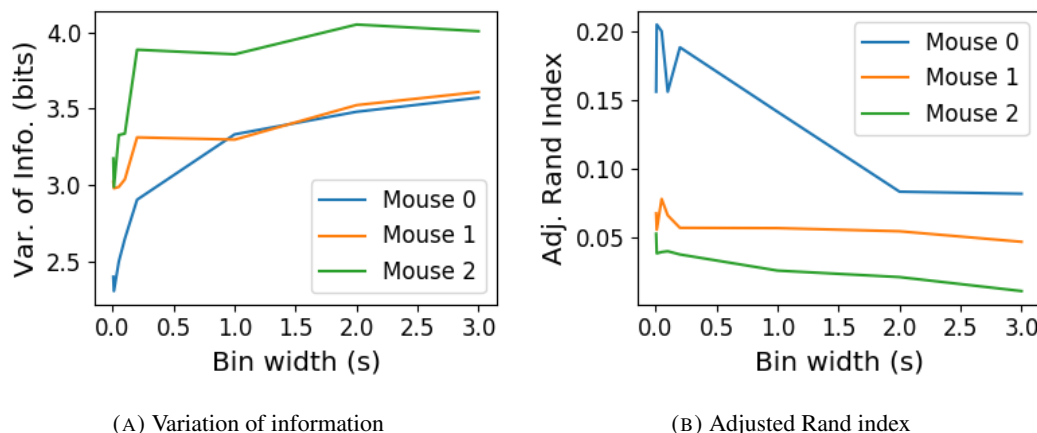
FIGURE 2.7: (A-B) Correlation matrices with detected communities indicated by white lines. Each off main diagonal entry in the matrix represents a pair of neurons. Those entries within a white square indicate that both of those neurons are in the same community as detected by our community detection procedure. Matrices shown are for 5ms and 1s time bin widths respectively. Main diagonal entries were set to 0. (C-D) Matrices showing the anatomical distribution of pairs along with their community membership. Entries where both cells are in the same region are given a colour indicated by the colour bar. Entries where cells are in different regions are given the grey colour also indicated by the colour bar.

to quantify the difference or similarity between the detected communities and the anatomical division. Details of these measures can be found in section 2.5.6 or in (Vinh, Epps, and Bailey, 2010).

We used two different types of measures for clustering comparison; information based measures (see section 2.5.6) and pair counting based measures (see section 2.5.6). We include one example of each in figure 2.8.

The variation of information is the information based measure included in figure 2.8a. This measure forms a metric on the space of clusterings. The larger the value for the variation of information, the more different the clusterings.

The adjusted Rand index is the pair counting based measure included in figure 2.8b. In contrast with the variation of information, the adjusted Rand index is a normalised similarity measure. The adjusted Rand index takes value 1 when the clusterings are identical, and takes value 0 when the clusterings are no more similar than chance.



(A) Variation of information

(B) Adjusted Rand index

FIGURE 2.8: (A) The variation of information is a measure of distance between clusterings. The distance between the anatomical ‘clustering’ and community detection ‘clustering’ increases with increasing time bin width. (B) The adjusted Rand index is a normalised similarity measure between clusterings. The anatomical and community detection clusterings become less similar as the time bin width increases.

Both measures indicated that the detected communities and the anatomical division of the cells were more similar when we used shorter time bins widths (see figure 2.8). This indicates that correlated behaviour in neuronal ensembles is more restricted to individual brain regions at short timescales (< 250ms), and the correlated activity spreads out across brain regions over longer time scales.

1173 **2.2.7 Conditional correlations & signal correlations**

1174 In light of the excellent research of Stringer et al (2019) showing that spontaneous behaviours
 1175 can drive activity in neuronal ensembles across the visual cortex and midbrain (Stringer et
 1176 al., 2019), we decided to control for the mouse's behaviour when performing our analyses.
 1177 It is possible that our community detection process may be detecting communities across
 1178 multiple brain regions at longer time scales due to aggregating neuronal activity driven by
 1179 several spontaneous behaviours occurring during the time interval covered by a given time bin.
 1180 A time bin of 1s, for example, could contain a spike count where those spikes were driven by
 1181 different spontaneous behaviours. We aimed to investigate this possibility by applying our
 1182 community detection analysis to conditional correlation measures.

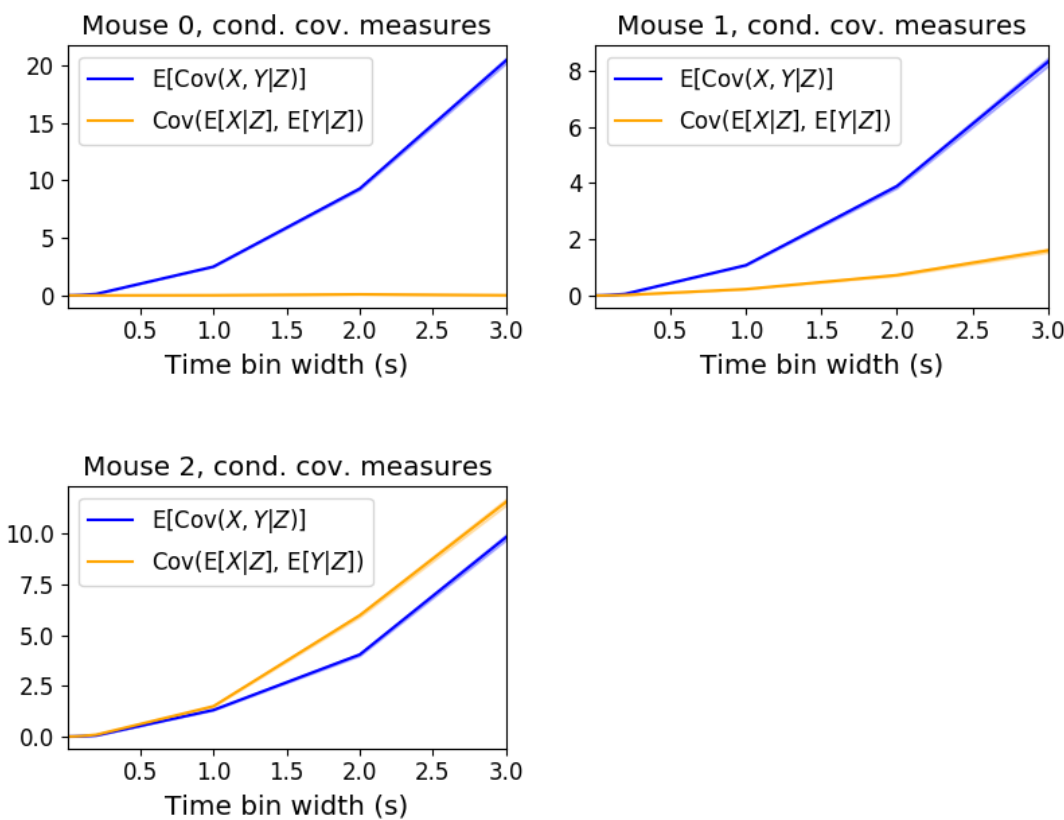


FIGURE 2.9: Comparing the components of the total covariance across different values for the time bin width. We observed a consistent increase in $E[\text{cov}(X, Y|Z)]$ as the time bin width increased. But we saw different trends for $\text{cov}(E[X|Z], E[Y|Z])$ for each mouse.

1183 We used the top 500 principal components of a video of the mouse's face as a measure of
 1184 the mouse's behaviour (see section 2.4.2). We modelled the spike counts as a linear combi-
 1185 nation of the principal components using linear regression with ElasticNet regularisation (see

section 2.5.3). Using this model, we quantified the expected spike count given the mouse’s behaviour $E[X|Z_1, \dots, Z_{500}]$.

We used these expected values to measure $\text{cov}(E[X|Z], E[Y|Z])$, and we used that value, the covariance $\text{cov}(X, Y)$, and the *law of total covariance* (see section 2.5.3) to measure $E[\text{cov}(X, Y|Z)]$. Here X and Y represent spike counts from individual cells, and Z is short-hand for the 500 principal components mentioned above. The two components of the covariance, $\text{cov}(E[X|Z], E[Y|Z])$ and $E[\text{cov}(X, Y|Z)]$, represent a ‘signal covariance’ and expected value of a ‘spike count covariance’ respectively, analogous to the signal correlation and spike count correlation (Cohen and Kohn, 2011).

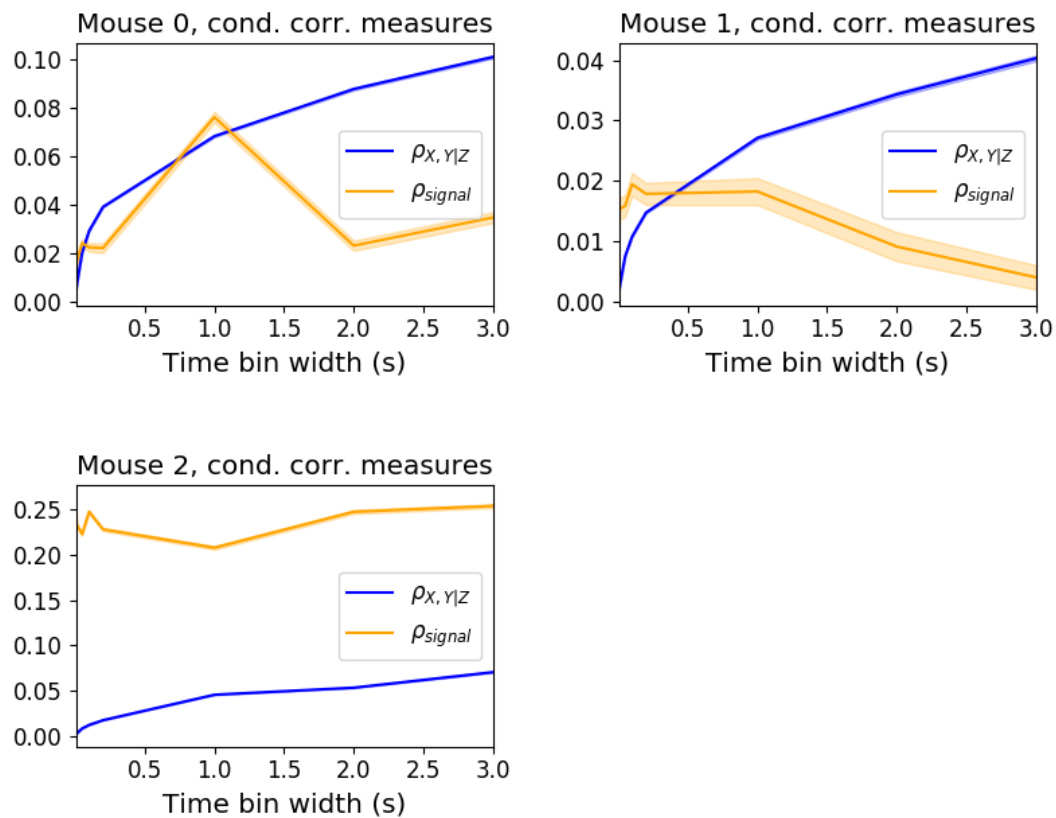


FIGURE 2.10: Comparing the components of the total covariance across different values for the time bin width. We saw a consistent increase in $\rho_{X,Y|Z}$ as the time bin width increased in all three subjects. But we saw different trends in ρ_{signal} for each of the subjects.

We examined the means of these components for different values of the time bin width (see figure 2.9). We observed a consistent increase in $E[\text{cov}(X, Y|Z)]$ as the time bin width increased. But we saw different trends for $\text{cov}(E[X|Z], E[Y|Z])$ for each mouse.

Using $\text{cov}(E[X|Z], E[Y|Z])$ we measured the signal correlation, ρ_{signal} , and using $E[\text{cov}(X, Y|Z)]$ we measured the event conditional correlation, $\rho_{X,Y|Z}$ (see section 2.5.3 for more details).

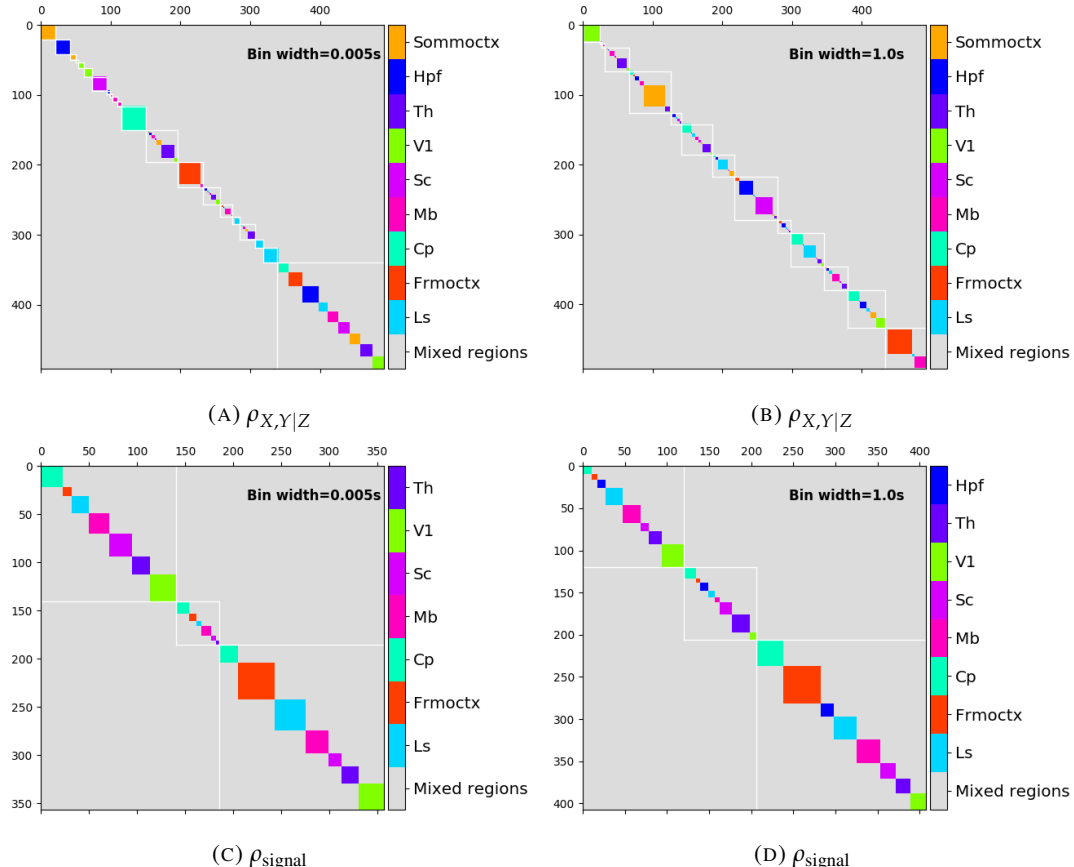


FIGURE 2.11: Matrices showing the regional membership of pairs by colour, and the communities in which those pairs lie. (A-B) Detected communities and regional membership matrix for network based on rectified spike count correlation $\rho_{X,Y|Z}$, using time bin widths of 0.005s and 1s respectively. (C-D) Detected communities and regional membership matrix for network based on rectified signal correlation ρ_{signal} , using time bin widths of 0.005s and 1s respectively.

1200 We saw a consistent increase in $\rho_{X,Y|Z}$ as the time bin width increased, this corresponds to
 1201 the result for $E[\text{cov}(X, Y|Z)]$. We observed different trends for ρ_{signal} for each mouse, this
 1202 corresponds to the result for $\text{cov}(E[X|Z], E[Y|Z])$.

1203 We applied our network noise rejection and community detection process to networks
 1204 based on the spike count correlations $\rho_{X,Y|Z}$ and the signal correlations ρ_{signal} . We noted that
 1205 the community detection on $\rho_{X,Y|Z}$ behaved similarly to the community detection on the total
 1206 correlation. We can see this in figures 2.11a and 2.11b. At very short time bin widths, we
 1207 detect more communities, and those communities often contain cells from one brain region
 1208 only. At longer time bin widths, we detect fewer communities, and those communities tend
 1209 to contain cells from multiple brain regions. When we examine the distance between (or
 1210 similarity between) the anatomical division of the cells, and the detected communities we
 1211 notice that the two clusterings are more similar at shorter time bin widths (see figure 2.12).

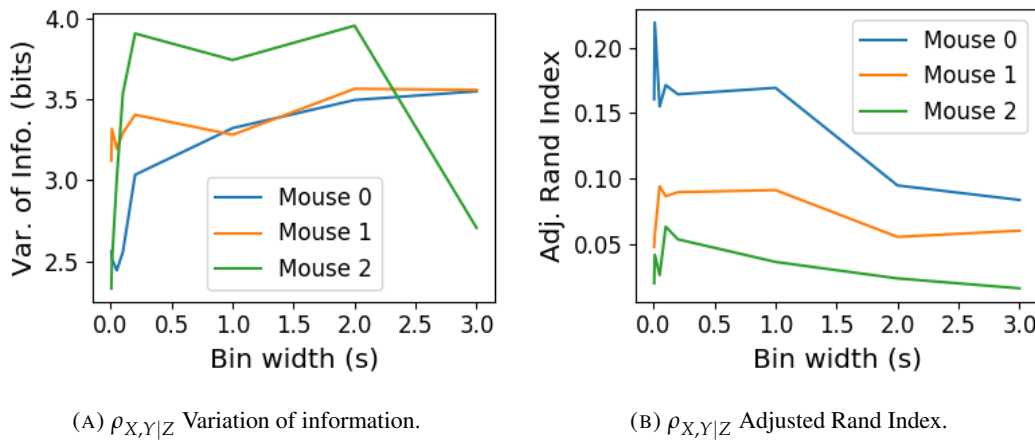
(A) $\rho_{X,Y|Z}$ Variation of information.(B) $\rho_{X,Y|Z}$ Adjusted Rand Index.

FIGURE 2.12: Distance and similarity measures between the anatomical division of the neurons, and the communities detected in the network based on the spike count correlations $\rho_{X,Y|Z}$. (A) The variation of information is a ‘distance’ measure between clusterings. The distance between the anatomical ‘clustering’ and the community clustering increases as the time bin width increases. (B) The adjusted Rand index is a similarity measure between clusterings. The detected communities become less similar to the anatomical division of the cells as the time bin width increases.

1212 When we applied the network noise rejection and community detection process to the
 1213 networks based on the signal correlations ρ_{signal} we found the number of communities we
 1214 detected reduced with increasing time bin width. But the number of communities detected
 1215 was less than that for the total correlations or the spike count correlations. The communi-
 1216 ties detected always tended to contain cells from multiple regions at both short and long
 1217 timescales (see figures 2.11c and 2.11d). The communities detected bore very little relation
 1218 to the anatomical division of the cells. The adjusted Rand index between the community

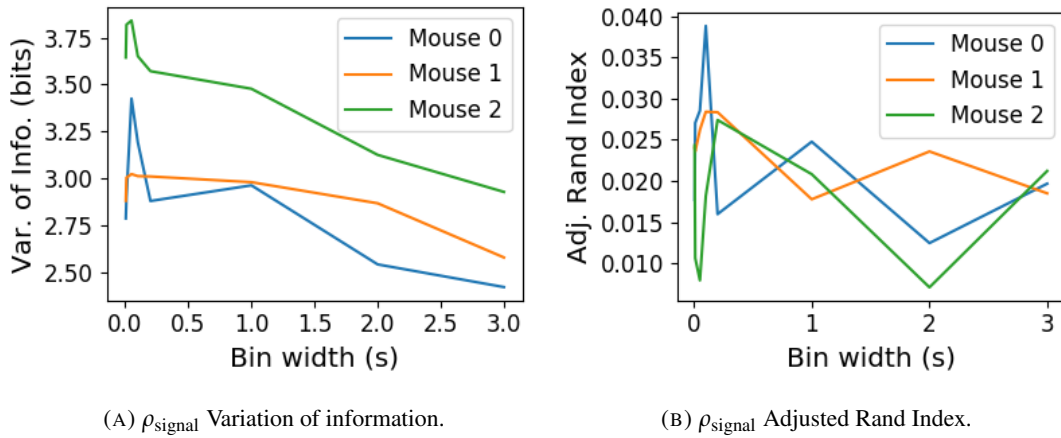
(A) ρ_{signal} Variation of information.(B) ρ_{signal} Adjusted Rand Index.

FIGURE 2.13: Distance and similarity measures between the anatomical division of the neurons, and the communities detected in the network based on the signal correlations ρ_{signal} . (A) The variation of information is a ‘distance’ measure between clusterings. The distance between the anatomical ‘clustering’ and the community clustering increases as the time bin width increases. (B) The adjusted Rand index is a similarity measure between clusterings. The detected communities become less similar to the anatomical division of the time bin width increases.

1219 clustering and the anatomical ‘clustering’ is close to zero for every time bin width (see figure
 1220 2.13b). This indicates that the similarity between the clusterings is close to chance. We did
 1221 observe a slight downward trend in the variation of information with increasing bin width
 1222 (see figure 2.13a), but this is more likely due to a decrease in the number of communities
 1223 detected rather than any relationship with anatomy.

1224 We also observed that the network noise rejection process rejected some of the cells
 1225 when applied to the network based on the signal correlations. This means that those cells
 1226 did not contribute to the additional structure of the network beyond that captured by the
 1227 sparse weighted configuration model. This is why the matrices in figures 2.11c and 2.11d are
 1228 smaller than their analogues in figures 2.11a and 2.11b.

1229 2.2.8 Absolute correlations and negative rectified correlations

1230 At the moment, the network noise rejection protocol can only be applied to weighted undi-
 1231 rected graphs with non-negative weights. This meant that we had to rectify our correlated
 1232 networks before applying the network noise rejection and community detection process. We
 1233 wanted to investigate what would happen if instead of rectifying the correlations, we used the
 1234 absolute value, or reversed the signs of the correlations and then rectified.

1235 When we used the absolute value of the correlations, we found very similar results to

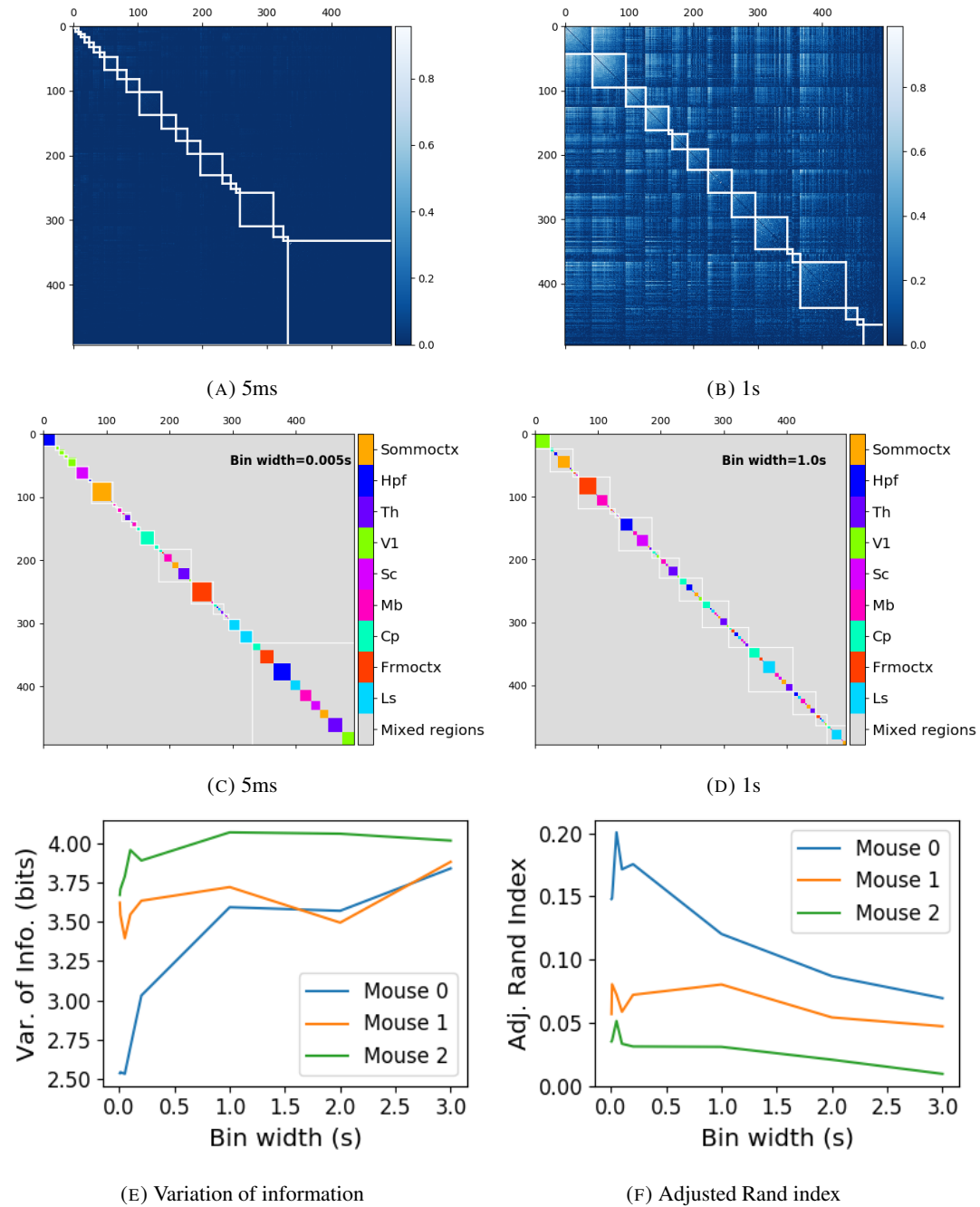


FIGURE 2.14: (A-B) Absolute correlation matrices with detected communities indicated by white lines. These communities are based on the absolute value of the total correlation between each pair of cells. Those entries within a white square indicate that both of those neurons are in the same community. Matrices shown are for 5ms and 1s time bin widths respectively. Main diagonal entries were set to 0. (C-D) Matrices showing the anatomical distribution of pairs along with their community membership. Regional membership is indicated by the colour bar. (E) Variation of information between the anatomical division of the cells, and the detected communities. (F) Adjusted Rand index between the anatomical division, and the detected communities.

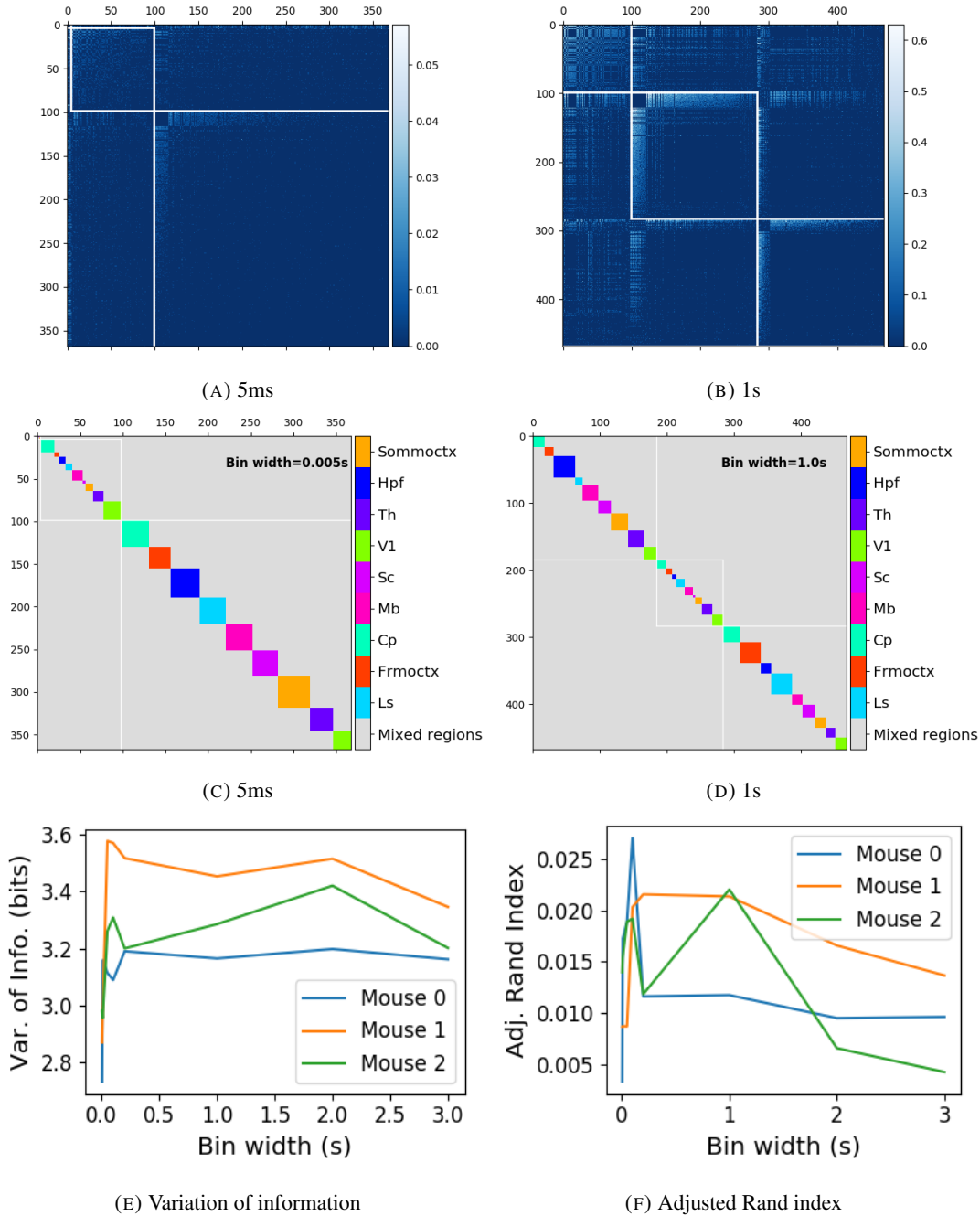


FIGURE 2.15: (A-B) Sign reversed rectified correlation matrices with detected communities indicated by white lines. Those entries within a white square indicate that both of those neurons are in the same community. Matrices shown are for 5ms and 1s time bin widths respectively. Main diagonal entries were set to 0. (C-D) Matrices showing the anatomical distribution of pairs along with their community membership. Regional membership is indicated by the colour bar. (E) Variation of information between the anatomical division of the cells, and the detected communities. (F) Adjusted Rand index between the anatomical division, and the detected communities.

1236 those shown above for the rectified total correlations and the rectified spike count corre-
1237 lations. We detected more communities using shorter bin widths, and these communities
1238 were more similar to the brain's anatomy than those communities detected using a longer bin
1239 width (see figure 2.14). The only exception being that we detected more communities. This
1240 could indicate that we detected both positively and negatively correlated communities, but
1241 we haven't done any further investigation so we cannot say for sure.

1242 When we used the sign reversed rectified correlated networks, we tended to find fewer
1243 communities. Each community contained cells from many different anatomical regions, at
1244 both long and short bin widths (see figures 2.15a, 2.15b, 2.15c, 2.15d). The communities
1245 bore little relation to the anatomical distribution of the cells, this can be seen in figure 2.15f,
1246 the values close to zero indicate that the similarity between the two clusterings are around
1247 chance level. This indicates that there was not much structure in the negatively correlated
1248 networks beyond that captured by the sparse weighted configuration model.

1249 2.3 Discussion

1250 It is well established that the brain uses correlated behaviour in neuronal ensembles to repre-
1251 sent the information taken in through sensation (Cohen and Maunsell, 2009; Litwin-Kumar,
1252 Chacron, and Doiron, 2012; deCharms and Merzenich, 1996). However, most studies that
1253 examine the nature of these correlations in-vivo, study an ensemble of cells from only one or
1254 two brain regions (Cohen and Kohn, 2011; Wierzynski et al., "2009"; Patterson et al., 2014;
1255 Girard, Hupé, and Bullier, 2001). Furthermore, recent results have shown that behaviour can
1256 drive correlated activity in multiple brain regions, including those not normally associated
1257 with motor control (Stringer et al., 2019; Gründemann et al., 2019; Allen et al., 2019). In this
1258 study, we utilised one of the newly recorded large datasets containing electrophysiological
1259 recordings from multiple brain regions simultaneously. We investigated correlated behaviour
1260 in these different brain regions and we investigated correlated behaviour between neurons in
1261 different regions, during spontaneous behaviour.

1262 A number of studies have found that the timescale of correlated behaviour induced by a
1263 stimulus can be modulated by the stimulus structure and behavioural context. For example,
1264 the spike train correlations between cells in weakly electric fish are modulated by the spa-
1265 tial extent of the stimulus (Litwin-Kumar, Chacron, and Doiron, 2012), and neurons in the
1266 marmoset primary auditory cortex modulate their spike timing (and therefore correlation) in
1267 response to stimulus features without modulating their firing rate (deCharms and Merzenich,

1268 1996). Furthermore, the width of the time bins over which spike counts are measured has
1269 been shown to have an effect on the magnitude of those correlations (Cohen and Kohn, 2011).
1270 Despite this, very little research has been done comparing correlation measures from the same
1271 dataset at different timescales. We investigated this by varying the time bin width used to bin
1272 spike times into spike counts from as short as 5ms up to 3s.

1273 In order to further investigate the effect of these correlations at different timescales, we
1274 regarded our neuronal ensemble as a weighted undirected graph, where each neuron is rep-
1275 resented by a node, and the weight on each edge is the correlation between the neurons
1276 connected by that edge. We then applied a novel clustering method from network science
1277 (Humphries et al., 2019) to identify communities in these networks. Communities in a net-
1278 work graph refer to sets of nodes that are more strongly connected to each other than the
1279 nodes outside of their set. Another way to put this is to say that the nodes in a community
1280 are more strongly connected than *expected*. What connection strength might be expected is
1281 defined by a null network model. We chose a null network model that matched the sparsity
1282 and total strength of our correlation based data networks. So, if two cells were in the same
1283 community, those cells were more correlated than would be expected given the correlation
1284 strength of their ensemble.

1285 These networks, and the community detection process, were completely agnostic of the
1286 anatomical division of the cells in our ensemble. When we compared the detected commu-
1287 nities with the anatomical division of the cells using distance and similarity measures for
1288 clusterings, we found that the detected communities were more similar to the anatomical
1289 division at shorter timescales. That is, when we used a wider time bin to count spikes, and
1290 computed pairwise correlations with these spike counts, the correlated communities tended to
1291 exist within anatomical regions at shorter timescales, and tended to span anatomical regions
1292 at longer timescales. This could reflect localised functional correlations at short time scales
1293 rippling outwards across brain regions at longer timescales. The brain may be processing
1294 some information quickly locally, and carrying out further, perhaps more detailed, represen-
1295 tation over a longer timescale across many regions using the representations that were just
1296 built locally.

1297 These changes in communities across timescales could also be driven by the anatomy
1298 of the individual cells. For example, it may simply take longer to transmit action potentials
1299 over longer distances, hence correlated activity over longer timescales will exist between
1300 anatomical regions, rather than within. However, the switch to almost exclusively multi-
1301 regional functional networks at 1s bin widths, rather than a mixture of multi-region, and

1302 single-region suggests that the inter-regional correlations either overpower, or inhibit the
1303 local correlations. So there may be more at play than just timescales.

1304 We acknowledged that the region spanning correlated communities that we detected at
1305 longer time scales could exist due to collating activity driven by distinct spontaneous activi-
1306 ties. In order to account for this, we modelled the spike counts as a linear function of the
1307 top 500 principal components of a video of the mouse's face filmed simultaneously with the
1308 electrophysiological readings. We applied our network noise rejection and community de-
1309 tection process to the weighted undirected networks formed by the spike count correlations
1310 (or noise correlations) and the signal correlations that we calculated using our model. For the
1311 spike count correlation networks, we found much the same results as for the total correlations
1312 as described above. For the signal correlations, the communities detected in these networks
1313 bore little relation to the anatomical division of the cells. Recent findings have shown that
1314 behavioural data accounts for correlations in many brain regions that would otherwise be
1315 dismissed as noise (Stringer et al., 2019), our finding to shows that these correlations are still
1316 governed by the timescale division betteen local and across-region communication.

1317 There is a lot of room for further investigation based on this research. For a start, the
1318 data that we used here were collected from nine different regions in the mouse brain, but
1319 none of these regions were part of the somatosensory cortex. Given that a mouse experiences
1320 so much of its environment through its sense of smell, some data from this region would be
1321 interesting to investigate. On the same theme, the mice in the experiment from which the
1322 data were collected were headfixed and placed on a rotating ball, but were otherwise behav-
1323 ing spontaneously. Had these mice been exposed to a visual, aural, or olfactory stimulus,
1324 we could have examined the responses of the cells in the brain regions corresponding to vi-
1325 sion, hearing, and olfaction, and compared these responses to the responses from the other
1326 brain regions. Furthermore, we could have investigated the interaction between the sets of
1327 responses.

1328 Another space for further investigation is the community detection. The algorithm that we
1329 used here never detects overlapping communities. But functional communities could indeed
1330 have overlaps. Clustering methods that detect overlapping clusters do exist (Baadel, Thabtah,
1331 and Lu, 2016). Applying one of those algorithms could yield some interesting results. Also,
1332 the community detection algorithm that we used here cannot process graphs with negative
1333 weights, this forced us to separate positive and negative correlations before applying our
1334 network noise rejection and community detections process, or use the absolute value of our
1335 correlations. A community detection algorithm that can work on weighted undirected graphs

1336 with negative weights could yield some interesting results here.

1337 **2.4 Data**

1338 The data that we used in this project were collected by Nick Steinmetz and his lab members
1339 (Stringer et al., 2019).

1340 **2.4.1 Brain regions**

1341 Neuropixels probes were used to collect extracellular recordings (Jun et al., 2017) from three
1342 different mice. The mice were awake, headfixed, and engaging in spontaneous behaviour.
1343 The mice were of different sexes and different ages. One mouse was ‘wild-type’, the others
1344 were mutants. Details as follows:

1345 1. male, wild type, P73.

1346 2. female, TetO-GCaMP6s, Camk2a-tTa, P113

1347 3. male, Ai32, Pvalb-Cre, P99

1348 Eight probes were used to collect readings from 2296, 2668, and 1462 cells respectively.

1349 Data were collected from nine brain regions in each mouse:

1350 • Caudate Putamen (CP)

1351 • Frontal Motor Cortex (Frmocx)

1352 • Hippocampal formation (Hpf)

1353 • Lateral Septum (Ls)

1354 • Midbrain (Mb)

1355 • Superior Colliculus (Sc)

1356 • Somatomotor cortex (Sommocx)

1357 • Thalamus (Th)

1358 • Primary visual cortex (V1)

1359 Readings were continuous and lasted for about 1 hour (Stringer et al., 2019). Locations of
1360 each of the probes can be seen in figure 2.16.

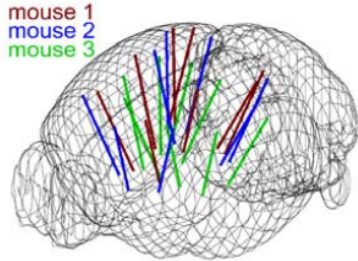


FIGURE 2.16: **Probe Locations:** The locations of the probes in each of the three mouse brains (Stringer et al., 2019).

2.4.2 Video recordings

Video recordings of the mouse's face were taken during the spontaneous behaviour. We had access to the top 500 principle components and top 500 eigenvectors of the processed videos. The frequency of recording was slightly less than 40Hz. Each frame contained 327×561 pixels. These principal components were used as behavioural data. We controlled for these components when taking measurements conditioned on behaviour.

2.5 Methods

2.5.1 Binning data

We transfoformed the spike timing data into binned spike count data by dividing the experimental period into time bins and counting the spikes fired by each cell within the time period covered by each of those bins. The data were divided into time bins of various widths ranging from 0.01s to 4s.

If the total length of the recording period was not an integer multiple of the time bin width, we cut off the remaining time at the end of the recording period. This period was at most 3.99s. This is far less than the total recording time of around 1 hour. So, this detail would not affect our results.

2.5.2 Correlation coefficients

We calculated Pearson's correlation coefficient for pairs of spike counts from pairs of neurons. For jointly distributed random variables X and Y , Pearson's correlation coefficient is

defined as:

$$\rho_{XY} = \frac{\text{cov}(X, Y)}{\sigma_X \sigma_Y} \quad (2.1)$$

$$= \frac{E[(X - \mu_X)(Y - \mu_Y)]}{\sigma_X \sigma_Y} \quad (2.2)$$

1378 where E denotes the expected value, μ denotes the mean, and σ denotes the standard deviation.
 1379 The correlation coefficient is a normalised measure of the covariance. It can take values
 1380 between 1 (completely correlated) and -1 (completely anti-correlated). Two independent
 1381 variables will have a correlation coefficient of 0. But, having 0 correlation does not imply
 1382 independence.

If we do not know the means and standard deviations required for equation 2.1, but we have samples from X and Y , Pearson's sample correlation coefficient is defined as:

$$r_{XY} = \frac{\sum_{i=1}^n (x_i - \bar{x})(y_i - \bar{y})}{\sqrt{\sum_{i=1}^n (x_i - \bar{x})^2} \sqrt{\sum_{i=1}^n (y_i - \bar{y})^2}} \quad (2.3)$$

1383 where $\{(x_i, y_i)\}$ for $i \in \{1, \dots, n\}$ are the paired samples from X and Y , and $\bar{x} = \frac{1}{n} \sum_{i=1}^n x_i$,
 1384 and $\bar{y} = \frac{1}{n} \sum_{i=1}^n y_i$ are the sample means.

1385 In practice we used the python function `scipy.stats.pearsonr` to calculate the
 1386 correlation coefficients.

1387 Total correlations, r_{SC}

1388 The total correlation (r_{SC}) of two cells is the correlation between the spike counts of those
 1389 cells in response to a given stimulus condition.

1390 Shuffled total correlations

1391 We measured the shuffled total correlations between two neurons by randomly permuting one
 1392 of the neuron's spike counts and measuring the total correlations. These shuffled correlations
 1393 were useful when measuring the effect of time bin width on correlations, and when decid-
 1394 ing which correlations should be preserved when creating correlation networks (see section
 1395 2.5.5).

1396 Separating Correlations & Anti-correlations

1397 In order to compare the effect of bin width on measures of negative r_{SC} (anti-correlation) and
 1398 positive r_{SC} separately, we had to separate correlated and anti-correlated pairs. To do this, we

simply measured the mean r_{SC} , taking the mean across all the bin widths. If this quantity was positive or zero we regarded the pair as positively correlated. If this quantity was negative we regarded the pair as anti-correlated.

2.5.3 Conditioning on behavioural data

Our behavioural data consisted of the top 500 principal components (PCs) of a processed video recording of the mouse's face (see section 2.4.2). Denoting the spike count of a given cell by X , and the PCs by Z_1, \dots, Z_{500} , we wanted to model X as a function of Z_1, \dots, Z_{500} in order to estimate

$$E[X|Z_1, \dots, Z_{500}] = \int_{x \in X} x P(X = x|Z_1, \dots, Z_{500}) dx \quad (2.4)$$

$$= \int_{x \in X} x \frac{P(X = x, Z_1, \dots, Z_{500})}{P(Z_1, \dots, Z_{500})} dx \quad (2.5)$$

Given the 500 components, a naïve estimation of $P(Z_1, \dots, Z_{500})$ or $P(X, Z_1, \dots, Z_{500})$ by histogramming was impossible. Therefore we modelled X as a linear combination of the PCs.

Linear regression

We modelled the spike count of a given cell, X , as a linear combination of the PCs of the video of the mouse's face, $\mathbf{Z} = Z_1, \dots, Z_{500}$. We tried three different types of regularization

- $L1$ or 'Lasso'

- $L2$ or 'Ridge regression'

- 'Elastic net' regularisation (a linear combination of both $L1$ and $L2$ regularisation penalties)

The elastic net regularisation performed the best, so we stuck with that.

Elastic net regularisation

Suppose we wish to model n observations of a random variable X , $\mathbf{x} = (x_1, \dots, x_n)$ using n instances of m predictors $\mathbf{Z} = (Z_1, \dots, Z_m)$. The naïve elastic net criterion is

$$L(\lambda_1, \lambda_2, \boldsymbol{\beta}) = |\mathbf{x} - \mathbf{Z}\boldsymbol{\beta}|^2 + \lambda_2|\boldsymbol{\beta}|_2 + \lambda_1|\boldsymbol{\beta}|_1 \quad (2.6)$$

where

$$|\boldsymbol{\beta}|_2 = \sum_{j=1}^m \beta_j^2 \quad (2.7)$$

$$|\boldsymbol{\beta}|_1 = \sum_{j=1}^m |\beta_j| \quad (2.8)$$

The naïve elastic net estimator $\hat{\boldsymbol{\beta}}$ is the minimiser of the system of equations 2.6 (Zou and Hastie, 2005)

$$\hat{\boldsymbol{\beta}} = \arg \min_{\boldsymbol{\beta}} L(\lambda_1, \lambda_2, \boldsymbol{\beta}) \quad (2.9)$$

1415 We implemented the model using the `ElasticNetCV` method of Python's
1416 `sklearn.linear_models` package.

1417 As well as using the PCs, we also tried fitting the models using the raw video data recon-
1418 structed from the PCs and eigenvectors. These models performed worse than those using the
1419 PCs. We expected this because each representation contains the same amount of information,
1420 but the raw video representation spreads this information across many more components.
1421 This requires more parameter fitting, but given the same information.

1422 **Conditional covariance**

We calculated the expected value of the conditional covariance using the law of total covari-
ance.

$$\text{cov}(X, Y) = E[\text{cov}(X, Y|Z)] + \text{cov}(E[X|Z], E[Y|Z]) \quad (2.10)$$

1423 where these expected values are calculated with respect to the distribution of Z as a random
1424 variable.

1425 The law of total covariance breaks the covariance into two components. The first com-
1426 ponent $E[\text{cov}(X, Y|Z)]$ is the expected value, under the distribution of Z , of the conditional
1427 covariance $\text{cov}(X, Y|Z)$. This covariance could be interpreted as the unnormalised version
1428 of what Cohen et al. (2011) call the spike count correlation (Cohen and Kohn, 2011), aka.
1429 the noise correlation. In particular, this is the covariance of the spike counts in response to
1430 repeated presentation of identical stimuli.

1431 The second component is analogous to what Cohn et al. (2011) call the *signal correlation*
1432 (Cohen and Kohn, 2011). In particular, $\text{cov}(E[X|Z], E[Y|Z])$ is the covariance between

¹⁴³³ spike counts in response to different stimuli.

Using our linear model, we calculated $E[X|Z_1, \dots, Z_{500}]$ for each cell X. Then we proceeded to calculate

$$E[\text{cov}(X, Y|Z_1, \dots, Z_{500})] = \text{cov}(X, Y) - \quad (2.11)$$

$$\text{cov}(E[X|Z_1, \dots, Z_{500}], E[Y|Z_1, \dots, Z_{500}]) \quad (2.12)$$

¹⁴³⁴ **Measures of conditional correlation**

As a measure of expected correlation, we measured the ‘event conditional correlation’ (Maugis, 2014)

$$\rho_{XY|Z} = \frac{E[\text{cov}(X, Y|Z)]}{\sqrt{E[\text{var}(X|Z)]}E[\text{var}(Y|Z)]} \quad (2.13)$$

¹⁴³⁵ Although this is not an actual correlation, it is an intuitive analogue to the correlation as a
¹⁴³⁶ normalised version of the covariance.

For comparison, we also measured the ‘signal correlation’

$$\rho_{\text{signal}} = \frac{\text{cov}(E[X|Z], E[Y|Z])}{\sqrt{\text{var}(E[X|Z])}\sqrt{\text{var}(E[Y|Z])}} \quad (2.14)$$

¹⁴³⁷ this is an actual correlation.

¹⁴³⁸ **2.5.4 Information Theory**

¹⁴³⁹ **Entropy $H(X)$**

The entropy of a random variable X, with outcomes x_1, \dots, x_N , and corresponding probabilities p_1, \dots, p_N is defined as

$$H(X) = - \sum_{n=1}^N p_n \log_2 p_n \quad (2.15)$$

¹⁴⁴⁰ This quantity is also known as the information entropy or the ‘surprise’. It measures the
¹⁴⁴¹ amount of uncertainty in a random variable. For example, a variable with a probability of 1
¹⁴⁴² for one outcome, and 0 for all other outcomes will have 0 bits entropy, because it contains no
¹⁴⁴³ uncertainty. But a variable with a uniform distribution will have maximal entropy as it is the
¹⁴⁴⁴ least predictable. This quantity is analogous to the entropy of a physical system (Shannon,

1445 1948). Note that any base may be used for the logarithm in equation 2.15, but using base 2
 1446 means that the quantity will be measured in ‘bits’.

The joint entropy of two jointly distributed random variables X and Y , where Y has outcomes y_1, \dots, y_M , is defined as

$$H(X, Y) = - \sum_{n=1}^N \sum_{m=1}^M P(X = x_n, Y = y_m) \log_2 P(X = x_n, Y = y_m) \quad (2.16)$$

1447 If X and Y are independent then $H(X, Y) = H(X) + H(Y)$. Otherwise $H(X, Y) <$
 1448 $H(X) + H(Y)$. When X and Y are completely dependent $H(X, Y) = H(X) = H(Y)$.

The conditional entropy of Y conditioned on X is defined as

$$H(Y|X) = - \sum_{n=1}^N \sum_{m=1}^M P(X = x_n, Y = y_m) \log_2 \frac{P(X = x_n, Y = y_m)}{P(X = x_n)} \quad (2.17)$$

1449 When X and Y are independent $H(Y|X) = H(Y)$. Intuitively, we learn nothing of Y by
 1450 knowing X , so Y is equally uncertain whether we know X or not. If Y is totally dependent
 1451 on X , then the fraction in the logarithm is 1, which gives $H(Y|X) = 0$.

1452 These entropy measures are the basis of the mutual information measure.

1453 Maximum entropy limit

When spiking data is binned into spike counts there is an upper limit on the entropy of these data. The maximum entropy discrete distribution is the discrete uniform distribution. A random variable with this distribution will take values from some finite set with equal probabilities. Binned spike count data will take values between 0 and some maximum observed spike count n_{\max} . A neuron with responses that maximises entropy will take these values with equal probability, i.e. if $i \in \{0, \dots, n_{\max}\}$ then $P(X = i) = \frac{1}{n_{\max}+1}$. The entropy of this neuron will be

$$\begin{aligned} H(X) &= - \sum_{i=0}^{n_{\max}} P(X = i) \log_2 P(X = i) \\ &= - \sum_{i=0}^{n_{\max}} \frac{1}{n_{\max}+1} \log_2 \left(\frac{1}{n_{\max}+1} \right) \\ &= - \log_2 \left(\frac{1}{n_{\max}+1} \right) \\ &= \log_2 (n_{\max} + 1) \end{aligned}$$

1454 Therefore, the maximum entropy of the binned spike counts of a neuron is $\log_2(n_{\max} + 1)$.
 1455 Of course, it would be very unusual for a neuron to fire in accordance with the discrete
 1456 uniform distribution. Most measurements of entropy taken on binned spiking data will be
 1457 much lower than the maximum. See figure 2.17 to see the maximum entropy as a function of
 1458 the maximum observed spike count.

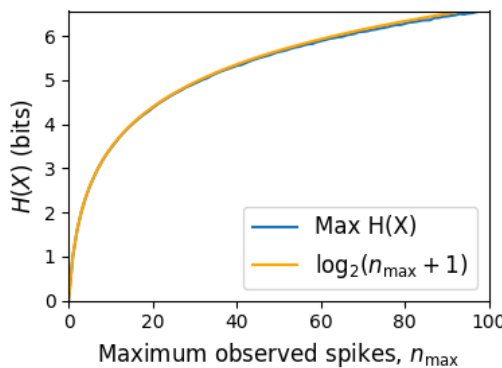


FIGURE 2.17: **Entropy Limit:** The upper limit on entropy of binned spike count data as a function of the maximum observed spike count. The orange line is the analytical maximum. The blue line is the entropy of samples with $N = 1000$ data points taken from the discrete uniform distribution.

1459 **Mutual Information $I(X; Y)$**

1460 The mutual information can be defined mathematically in a number of ways, all of which are
 1461 equivalent. These definitions illustrate the different ways of interpreting the mutual informa-
 1462 tion.

For two jointly distributed random variables X and Y , the mutual information $I(X; Y)$ is defined as

$$I(X; Y) = H(Y) - H(Y|X) \quad (2.18)$$

$$= H(X) - H(X|Y) \quad (2.19)$$

1463 Equation 2.18 fits with the following intuition: The mutual information between X and Y is
 1464 the reduction in uncertainty about X gained by knowing Y , or vice versa. We could also say
 1465 the mutual information is the amount of information gained about X by knowing Y , or vice
 1466 versa.

Another useful entropy based definition for the mutual information is

$$I(X; Y) = H(X) + H(Y) - H(X, Y) \quad (2.20)$$

¹⁴⁶⁷ This definition is useful because it does not require the calculation of conditional probabilities.
¹⁴⁶⁸

The mutual information can also be defined in terms of marginal, joint, and conditional distributions. For example,

$$I(X;Y) = - \sum_{n=1}^N \sum_{m=1}^M P(X = x_n, Y = y_m) \log_2 \frac{P(X = x_n, Y = y_m)}{P(X = x_n)P(Y = y_m)} \quad (2.21)$$

Notice that this can be rewritten as a Kullback–Leibler divergence.

$$I(X;Y) = D_{KL}(P(X,Y) || P(X)P(Y)) \quad (2.22)$$

¹⁴⁶⁹ So, we can also think of the mutual information as a measure of the difference between
¹⁴⁷⁰ the joint distribution of X and Y , and the product of their marginal distributions. Since the
¹⁴⁷¹ product of the marginal distributions is the joint distribution for independent variables, we
¹⁴⁷² can think of the mutual information as a measure of the variables' dependence on one another.

¹⁴⁷³ The minimum value that $I(X;Y)$ can take is 0. This occurs when the random variables
¹⁴⁷⁴ X and Y are independent. Then we have $H(X|Y) = H(X)$, and $H(Y|X) = H(Y)$, which
¹⁴⁷⁵ according to equation 2.18, gives $I(X;Y) = 0$. We also have that $H(X,Y) = H(X) +$
¹⁴⁷⁶ $H(Y)$ in this case, which according equation 2.20, gives $I(X;Y) = 0$. Finally, we also have
¹⁴⁷⁷ $P(X,Y) = P(X)P(Y)$, which leaves us with 1 in the argument for the logarithm in equation
¹⁴⁷⁸ 2.21, which again gives $I(X;Y) = 0$.

¹⁴⁷⁹ The mutual information reaches its maximum value when one of the variables X and
¹⁴⁸⁰ Y is completely determined by knowing the value of the other. In that case $I(X;Y) =$
¹⁴⁸¹ $\min\{H(X), H(Y)\}$.

¹⁴⁸² Variation of Information $VI(X,Y)$

The variation of information is another information theoretical quantity based on the mutual information. It is defined as

$$VI(X;Y) = H(X) + H(Y) - 2I(X;Y) \quad (2.23)$$

We can rewrite this as the summation of two positive quantities

$$VI(X;Y) = [H(X) - I(X;Y)] + [H(Y) - I(X;Y)] \quad (2.24)$$

1483 In English, the variation of information is the summation of the uncertainty in the random
1484 variables X and Y excluding the uncertainty shared by those variables.

1485 This measure will become more relevant when we go on to talk about clusterings because
1486 $VI(X; Y)$ forms a metric on the space of clusterings.

1487 **Measuring entropies & mutual information**

1488 In practice, we measured the mutual information between spike counts using Python and the
1489 python package `pyitlib`. We used the PT-bias correction technique to estimate the bias of
1490 our measurements when measuring the mutual information between the spike counts of two
1491 cells (Treves and Panzeri, 1995).

1492 When measuring the mutual information between clusterings we used Python, but we
1493 used the `mutual_info_score`, `adjusted_mutual_info_score`, and
1494 `normalized_mutual_info_score` functions from the `sklearn.metrics` part of
1495 the `sklearn` package.

1496 **2.5.5 Network analysis**

1497 **Correlation networks**

1498 In order to analyse functional networks created by the neurons in our ensemble, we mea-
1499 sured the total correlation between each pair of neurons. These measurements induced an
1500 undirected weighted graph/network between the neurons. The weight of each connection
1501 was equal to the total correlation between each pair of neurons.

1502 We followed the same procedure for total correlations 2.5.2, spike count correlations, and
1503 signal correlations 2.5.3.

1504 **Rectified correlations**

1505 At the time of writing, the community detection method outlined in (Humphries et al., 2019)
1506 could only be applied to networks with positively weighted connections. But many neuron
1507 pairs were negatively correlated. To apply the community detection method, we *rectified* the
1508 network, by setting all the negative weights to zero.

1509 We also looked for structure in the network created by negative correlations by reversing
1510 the signs of the correlations, and rectifying these correlations before applying our network
1511 analysis.

1512 Finally, we used the absolute value of the correlations as the weights for the graph/network.
1513 By doing this, we hoped to identify both correlated and anti-correlated functional communi-
1514 ties of neurons.

1515 **Sparsifying data networks**

1516 When creating our correlation networks, we wanted to exclude any correlations that could
1517 be judged to exist ‘by chance’. To do this, we measured the 5th and 95th percentile of
1518 the shuffled correlations (see section 2.5.2) for the given mouse and time bin width. We
1519 then set all the data correlations between these two values to 0. This excluded any ‘chance’
1520 correlations from our network, and created a sparser network. This allowed us to make use
1521 of the ‘sparse weighted configuration model’ as described in section 2.5.5.

1522 **Communities**

1523 Given some network represented by an adjacency matrix \mathbf{A} , a community within that net-
1524 work is defined as a collection of nodes where the number of connections within these nodes
1525 is higher than the expected number of connections between these nodes. In order to quan-
1526 tify the ‘expected’ number of connections, we need a model of expected networks. This is
1527 analogous to a ‘null model’ in traditional hypothesis testing. We test the hypothesis that our
1528 data network departs from the null network model to a statistically significant degree. For
1529 undirected unweighted networks, the canonical model of a null network is the configuration
1530 model (Fosdick et al., 2016). Since we are working with weighted sparse networks, we used
1531 more suitable null models, described below.

1532 **Weighted configuration model**

1533 The *weighted configuration model* is a canonical null network model for weighted networks.
1534 Given some data network, the weighted configuration model null network will preserve the
1535 degree sequence and weight sequence of each node in the data network. But the edges will
1536 be distributed randomly (Fosdick et al., 2016). Any structure in the data network beyond
1537 its degree sequence and weight sequence will not be captured in the weighted configuration
1538 model. So, this model can be used in testing the hypothesis that this extra structure exists.

1539 **Sparse weighted configuration model**

1540 The *sparse weighted configuration model* is another null network model. Similar in nature to
1541 the weighted configuration model (see section 2.5.5), but the sparsity of the data network is

1542 preserved in the null network. This is achieved by sampling from a probability distribution
 1543 for the creation or non-creation of each possible connection, then distributing the weight of
 1544 the data network randomly in this sparse network (Humphries et al., 2019). This is the null
 1545 network that we used when searching for additional structure in our data networks.

1546 **Spectral rejection**

1547 We made use of the spectral rejection algorithm as outlined in (Humphries et al., 2019). The
 1548 spectral rejection algorithm is a method for finding structure in a network not captured by a
 1549 supposed null model, if such structure exists.

To describe the method, we denote our data network matrix \mathbf{W} , we denote the expected network of our null network model as $\langle \mathbf{P} \rangle$. Then the departure of our data network from the null network can be described by the matrix

$$\mathbf{B} = \mathbf{W} - \langle \mathbf{P} \rangle \quad (2.25)$$

1550 a common choice for $\langle \mathbf{P} \rangle$ in community detection is the ‘configuration model’ (Fosdick et
 1551 al., 2016; Humphries, 2011). The matrix \mathbf{B} is often called the configuration matrix, in this
 1552 context we will use the term ‘deviation matrix’ as it captures the deviation of \mathbf{W} from the
 1553 null model.

1554 To test for structure in the network represented by \mathbf{W} , we examine the eigenspectrum of \mathbf{B}
 1555 and compare it to the eigenspectrum of our null model. Firstly, note that since our data model
 1556 doesn’t allow self loops, and is not directed, the matrix representing the network will be
 1557 symmetric and positive semi-definite, and will therefore be invertible with real eigenvalues.
 1558 We selected a null model with the same characteristics.

1559 To find the eigenspectrum of the null model, we generated N samples from our null
 1560 model P_1, \dots, P_N , and we measured their deviation matrices B_1, \dots, B_N . We then calculated
 1561 the eigenspectrum of each of those samples. We calculated the upper bound of the null model
 1562 eigenspectrum by taking the mean of the largest eigenvalues of B_1, \dots, B_N . We calculated a
 1563 lower bound on the null model eigenspectrum by taking the mean of the smallest eigenvalues
 1564 of B_1, \dots, B_N .

1565 We then calculated the eigenspectrum of \mathbf{B} , our data network deviation matrix. If any of
 1566 those eigenvalues lay outside of the upper or lower bounds of the null model eigenspectrum,
 1567 this is evidence of additional structure not captured by the null model. If we chose the sparse
 1568 weighted configuration model (see section 2.5.5) as our null network model, then eigenvalues

1569 lying below the lower bound indicate k -partite structure in the network. For example, if one
1570 eigenvalue lay below the lower bound, this would indicate some bipartite structure in the data
1571 network. If any eigenvalues lay above the upper bound of the null model eigenspectrum, this
1572 is evidence of community structure in the data network. For example, one eigenvalue of \mathbf{B}
1573 lying above the upper bound of the null model eigenspectrum indicates the presence of two
1574 communities in the network (Humphries, 2011).

1575 **Node rejection**

1576 If there are d data eigenvalues lying outside of the null network eigenspectrum, the d eigen-
1577 vectors corresponding to these eigenvalues will form a vector space. If we project the nodes
1578 of our network into this vector space, by projecting either rows or columns of the data matrix,
1579 we can see how strongly each node contributes to the vector space. Nodes that contribute
1580 strongly to the additional structure will project far away from the origin, nodes that do not
1581 contribute to the additional structure will project close to the origin. We want to use this
1582 information to discard those nodes that do not contribute.

1583 We can test whether a node projects *far* away from the origin or *close* to the origin
1584 using the eigenvalues and eigenvectors of B_1, \dots, B_N . The j th eigenvector and eigenvalue
1585 of B_i gives a value for a null network's projection into the j th dimension of the additional
1586 structure vector space. The matrices B_1, \dots, B_N give N projections into that dimension.
1587 These projections are a distribution of the null networks' projections. If the data node's
1588 projection exceeds that of the null network projections this node is judged to project *far* from
1589 the origin, and therefore contribute to the additional structure. Otherwise, the node is judged
1590 to project *close* to the origin, and is therefore rejected (Humphries et al., 2019).

1591 **Community detection**

1592 Another application for this d dimensional space is community detection. We first project
1593 all of the nodes into this d -dimensional space, then perform the clustering in this space. The
1594 clustering and community detection procedure is described in (Humphries, 2011).

1595 In practice, the procedure is carried out n times (we chose $n = 100$ times), this returns n
1596 clusterings. We resolve these n clusterings to one final clustering using *consensus clustering*.
1597 We used the consensus clustering method that uses an explicit null model for the consensus
1598 matrix, as outlined in (Humphries et al., 2019).

2.5.6 Clustering Comparison

A clustering \mathcal{C} is a partition of a set D into sets C_1, C_2, \dots, C_K , called clusters, that satisfy the following for all $k, l \in \{1, \dots, K\}$:

$$C_k \cap C_l = \emptyset \quad (2.26)$$

$$\bigcup_{k=1}^K C_k = D \quad (2.27)$$

If we consider two clusterings, \mathcal{C} with clusters C_1, C_2, \dots, C_K and \mathcal{C}' with clusters C'_1, C'_2, \dots, C'_K . There are a number of measurements we can use to compare \mathcal{C} and \mathcal{C}' . In the following, the number of elements in D is denoted by n , and the number of elements in cluster C_k is n_k .

Adjusted Rand Index

The *adjusted Rand Index* is a normalised similarity measure for clusterings based on pair counting.

If we consider the clusterings \mathcal{C} and \mathcal{C}' , and denote

- the number of pairs in the same cluster in \mathcal{C} and \mathcal{C}' by N_{11}

- the number of pairs in different clusters in \mathcal{C} and \mathcal{C}' by N_{00}

- the number of pairs in the same cluster in \mathcal{C} and different clusters in \mathcal{C}' by N_{10}

- the number of pairs in different clusters in \mathcal{C} and the same cluster in \mathcal{C}' by N_{01}

then the *Rand Index* is defined as

$$RI = \frac{N_{11} + N_{00}}{N_{11} + N_{00} + N_{10} + N_{01}} = \frac{N_{11} + N_{00}}{\binom{n}{2}} \quad (2.28)$$

The Rand Index is 1 when the clusterings are identical, and 0 when the clusterings are completely different.

The *adjusted Rand Index* intends on correcting the Rand Index for chance matching pairs.

This is defined as

$$ARI = \frac{2(N_{00}N_{11} - N_{01}N_{10})}{(N_{00} + N_{01})(N_{01} + N_{11}) + (N_{00} + N_{10})(N_{10} + N_{11})} \quad (2.29)$$

The adjusted Rand Index is 1 when the clusterings are identical, and 0 when the Rand Index is equal to its expected value.

1616 **Clusterings as random variables**

If we take any random element of D , the probability that this element is in cluster C_k of clustering \mathcal{C} is

$$P(K = k) = \frac{n_k}{n} \quad (2.30)$$

1617 this defines a probability distribution, which makes the clustering a random variable. Any
1618 clustering can be considered as a random variable this way.

This means that we can measure any of the information theoretic quantities defined in section 2.5.4 with respect to clusterings. For example, the entropy of a clustering is

$$H(\mathcal{C}) = - \sum_{k=1}^K \frac{n_k}{n} \log \frac{n_k}{n} \quad (2.31)$$

If we have two clusterings, the joint probability distribution of these clusterings is defined as

$$P(K = k, K' = k') = \frac{|C_k \cap C'_{k'}|}{n} \quad (2.32)$$

1619 The joint distribution allows us to define the mutual information between two clusterings,
1620 $I(\mathcal{C}; \mathcal{C}')$ (Meilă, 2007).

1621 **Information based similarity measures**

The mutual information between two clusterings is a similarity measure, with $I(\mathcal{C}; \mathcal{C}') = 0$ if \mathcal{C} and \mathcal{C}' are completely different, and $I(\mathcal{C}; \mathcal{C}') = H(\mathcal{C}) = H(\mathcal{C}')$ if \mathcal{C} and \mathcal{C}' are identical. This can be normalised in a number of different ways to make more similarity measures (Vinh, Epps, and Bailey, 2010)

$$NMI_{joint} = \frac{I(\mathcal{C}; \mathcal{C}')}{H(\mathcal{C}, \mathcal{C}')} \quad (2.33)$$

$$NMI_{max} = \frac{I(\mathcal{C}; \mathcal{C}')}{\max\{H(\mathcal{C}), H(\mathcal{C}')\}} \quad (2.34)$$

$$NMI_{sum} = \frac{2I(\mathcal{C}; \mathcal{C}')}{H(\mathcal{C}) + H(\mathcal{C}')} \quad (2.35)$$

$$NMI_{sqrt} = \frac{I(\mathcal{C}; \mathcal{C}')}{\sqrt{H(\mathcal{C})H(\mathcal{C}')}} \quad (2.36)$$

$$NMI_{min} = \frac{I(\mathcal{C}; \mathcal{C}')}{\min\{H(\mathcal{C}), H(\mathcal{C}')\}} \quad (2.37)$$

We can control for chance similarities between the two clusterings by measuring the *adjusted mutual information* between the clusterings. This is defined as

$$AMI_{sum} = \frac{I(\mathcal{C}; \mathcal{C}') - E\{I(\mathcal{C}; \mathcal{C}')\}}{\frac{1}{2}[H(\mathcal{C}) + H(\mathcal{C}')] - E\{I(\mathcal{C}; \mathcal{C}')\}} \quad (2.38)$$

1622 The first term in the denominator, taking the average of the marginal entropies, can be replaced
1623 by taking the maximum, minimum, or the geometric mean (Vinh, Epps, and Bailey, 2010).

1624 Information based metrics

The variation of information between two clusterings $VI(\mathcal{C}; \mathcal{C}')$ (see section 2.5.4) is a metric on the space of clusterings (Meilă, 2007). That is,

$$VI(\mathcal{C}; \mathcal{C}') \geq 0 \quad (2.39)$$

$$VI(\mathcal{C}; \mathcal{C}') = 0 \iff \mathcal{C} = \mathcal{C}' \quad (2.40)$$

$$VI(\mathcal{C}; \mathcal{C}') = VI(\mathcal{C}'; \mathcal{C}) \quad (2.41)$$

$$VI(\mathcal{C}; \mathcal{C}'') \leq VI(\mathcal{C}; \mathcal{C}') + VI(\mathcal{C}'; \mathcal{C}'') \quad (2.42)$$

Another metric is the *information distance* (Vinh, Epps, and Bailey, 2010)

$$D_{max} = \max\{H(\mathcal{C}), H(\mathcal{C}')\} - I(\mathcal{C}; \mathcal{C}') \quad (2.43)$$

Both of these can be normalised

$$NVI(\mathcal{C}; \mathcal{C}') = 1 - \frac{I(\mathcal{C}; \mathcal{C}')}{H(\mathcal{C}, \mathcal{C}')} \quad (2.44)$$

$$d_{max} = 1 - \frac{I(\mathcal{C}; \mathcal{C}')}{\max\{H(\mathcal{C}), H(\mathcal{C}')\}} \quad (2.45)$$

1625 Comparing detected communities and anatomical divisions

1626 In order to quantify the difference or similarity between the communities detected in our cor-
1627 relation network and the anatomical classification of the cells in that network, we considered
1628 the communities and the anatomical regions as clusters in two different clusterings, \mathcal{C}_{comm}
1629 and \mathcal{C}_{anat} , respectively. We then measured the similarity between the clusterings using the
1630 mutual information, the adjusted mutual information, and the normalised mutual informa-
1631 tion. We measured the difference between, or the distance between, the clusterings using the

1632 variation of information, the normalised variation of information, and the normalised infor-
1633 mation distance. We also measured the difference between the clusterings using the adjusted
1634 Rand Index, just to use a non-information based measure.

1635 We took all of these measures for communities detected using different time bin widths.
1636 This gave us an idea of the effect of time bin width on correlation networks in neural ensem-
1637 bles relative to anatomical regions within those ensembles.

¹⁶³⁸ **Chapter 3**

¹⁶³⁹ **A simple two parameter distribution
for modelling neuronal activity and
capturing neuronal association**

1642

UNIVERSITY OF BRISTOL

1643

Abstract

1644

Engineering

1645

Department of Computer Science

1646

Doctor of Philosophy

1647

Investigating, implementing, and creating methods for analysing large neuronal ensembles

1649

by Thomas J. DELANEY

1650

Recent developments in electrophysiological technology have lead to an increase in the size of electrophysiology datasets. Consequently, there is a requirement for new analysis techniques that can make use of these new datasets, while remaining easy to use in practice. In this work, we fit some one or two parameter probability distributions to spiking data collected from a mouse exposed to visual stimuli. We show that the Conway-Maxwell-binomial distribution is a suitable model for the number of active neurons in a neuronal ensemble at any given moment. This distribution fits these data better than binomial or beta-binomial distributions. It also captures the correlated activity in the primary visual cortex induced by stimulus onset more effectively than simply measuring the correlations, at short timescales (< 10ms). We also replicate the finding of Churchland et al (2010) relating to stimulus onset quenching neural variability in cortical areas, and we show a correspondence between this quenching and changes in one of the parameters of the fitted Conway-Maxwell-binomial distributions.

3.1 Introduction

Recent advances in electrophysiological technology, such as ‘Neuropixels’ probes (Jun et al., 2017) have allowed extracellular voltage measurements to be collected from larger numbers of cells than traditional methods, in multiple brain regions simultaneously, and routinely. These larger datasets require innovative methods to extract information from the data in a reasonable amount of time, ‘reasonable’ being subjective in this case.

Theoretically, all the information at any given moment in an electrophysiological dataset with n neurons could be captured by calculating the probability distribution for every possible spiking pattern. This would require defining a random variable with 2^n possible values, a task that quickly becomes impossible as n increases. Attempts at approximating this random variable often involve measuring pairwise or higher order correlations (Schneidman et al., 2006; Flach, 2013; Ganmor, Segev, and Schneidman, 2011). But pairwise correlations may not be enough to characterise instantaneous neural activity (Tkačik et al., 2014). Furthermore, these kinds of models tend to ignore the temporal structure of neuronal data, in favour of smaller model size, and scalability.

Higher order correlations would be helpful here, but defining these correlations can be tricky, never-mind quantifying them. If we use the interaction parameters arising from the exponential family model as measures of higher order correlations, measuring these correlations becomes computationally impractical quite quickly also (the number of ‘three neuron correlations’ to measure scales with $(^n_3)$). In this paper, we dispense with measuring correlations directly, and attempt to characterise correlated behaviour by measuring ‘association’; a more general concept that includes correlation.

In this work, we examined the ability of simple distributions to model the number of active (spiking) neurons in a neuronal ensemble at any given timepoint. We compared a little-known distribution named the Conway-Maxwell-binomial distribution to the binomial distribution and the beta-binomial distribution. The binomial distribution is a probability distribution over the number of successes in a sequence of independent and identical Bernoulli trials. The beta-binomial distribution is similar, but allows for a bit more flexibility while still being a model for heterogeneity. Similar to the binomial and beta-binomial, the Conway-Maxwell-binomial distribution is a probability distribution over the number of successes in a series of Bernoulli trials, but allows over- and under-dispersion relative to the binomial distribution. This distribution should therefore be a good candidate for our purposes. We found that Conway-Maxwell-binomial distribution was usually the best candidate of the three that

1695 we examined.

1696 We also observed some interesting changes in the number of active neurons in the primary
1697 visual cortex and hippocampus at stimulus onset and some changes in this activity in the
1698 thalamus which were sustained for the full duration of the stimulus presentation. This let us
1699 know that there were some responses to model.

1700 We found that fitting a Conway-Maxwell-binomial distribution was a better method of
1701 capturing association between neurons than measuring the spike count correlation for the
1702 short time bins that we used (< 10ms).

1703 Finally, we also wanted to investigate parallels between the parameters of the Conway-
1704 Maxwell-binomial distribution and quantities that have been established as relevant to sen-
1705 sory processing. So, we replicated the findings made by Churchland et al. (2010) relating
1706 to a reduction in neural variability at stimulus onset in the macaque cortical regions, but for
1707 data taken from the mouse primary visual cortex. We compared these findings to the values
1708 of the fitted Conway-Maxwell-binomial distribution parameters.

1709 3.2 Data

1710 We used data collected by Nick Steinmetz and his lab ‘CortexLab at UCL’ (Steinmetz, Caran-
1711 dini, and Harris, 2019). The data can be found online ¹ and are free to use for research
1712 purposes.

1713 Two ‘Phase3’ Neuropixels (Jun et al., 2017) electrode arrays were inserted into the brain
1714 of an awake, head-fixed mouse for about an hour and a half. These electrode arrays recorded
1715 384 channels of neural data each at 30kHz and less than $7\mu\text{V}$ RMS noise levels. The sites
1716 are densely spaced in a ‘continuous tetrode’-like arrangement, and a whole array records
1717 from a 3.8mm span of the brain. One array recorded from visual cortex, hippocampus, and
1718 thalamus, the other array recorded from motor cortex and striatum. The data were spike-
1719 sorted automatically by Kilosort and manually by Nick Steinmetz using Phy. In total 831
1720 well-isolated individual neurons were identified.

1721 3.2.1 Experimental protocol

1722 The mouse was shown a visual stimulus on three monitors placed around the mouse at right
1723 angles to each other, covering about ± 135 degrees azimuth and ± 35 degrees elevation.

¹<http://data.cortexlab.net/dualPhase3/>

1724 The stimulus consisted of sine-wave modulated full-field drifting gratings of 16 drift di-
1725 rections ($0^\circ, 22.5^\circ, \dots, 337.5^\circ$) with 2Hz temporal frequency and 0.08 cycles/degree spatial
1726 frequency displayed for 2 seconds plus a blank condition. Each of these 17 conditions were
1727 presented 10 times in a random order across 170 different trials. There were therefore 160
1728 trials with a drifting-grating visual stimulus present, and 10 trials with a blank stimulus.

1729 **3.3 Methods**

1730 **3.3.1 Binning data**

1731 We converted the spike times for each cell into spike counts by putting the spike times into
1732 time bins of a given ‘width’ (in milliseconds). We used time bins of 1ms, 5ms, and 10ms.
1733 We used different time bin widths to assess the impact of choosing a bin width.

1734 **3.3.2 Number of *active* neurons**

1735 To count the number of active neurons in each neuronal ensemble, we split the time interval
1736 for each trial into bins of a given width. We counted the number of spikes fired by each cell
1737 in each bin. If a cell fired *at least* one spike in a given bin, we regarded that cell as active in
1738 that bin. We recorded the number of active cells in every bin, and for the purposes of further
1739 analysis, we recorded each cell’s individual spike counts.

1740 It should be noted that when we used a bin width of 1ms, the maximum number of
1741 spikes in any bin was 1. For the wider time bins, some bins had spike counts greater than
1742 1. Consequently when using a bin width of 1ms, the number of active neurons and the total
1743 spike count of a given bin were identical. But for wider bin widths, the total spike count was
1744 greater than the number of active neurons.

1745 So for the 1ms bin width, the activity of a neuron and the number of spikes fired by that
1746 neuron in any bin can be modelled as a Bernoulli variable. But for wider time bins, only the
1747 activity can be modelled in this way.

1748 **3.3.3 Moving windows for measurements**

1749 When taking measurements (e.g. moving average over the number of active neurons) or
1750 fitting distributions (eg. the beta binomial distribution) we slid a window containing a certain
1751 number of bins across the data, and made our measurements at each window position. For
1752 example, when analysing 1ms bin data, we used a window containing 100 bins, and we slid

Bin width (ms)	Window size (bins)	Window size (ms)	Windows per trial
1ms	100	100ms	296
5ms	40	200ms	286
10ms	40	400ms	266

TABLE 3.1: Details of the different bin width and analysis window sizes used when binning spike times, and analysing those data.

1753 the window across the time interval for each trial moving 10 bins at a time. So that for
 1754 3060ms of data, we made 296 measurements.

1755 For the 5ms bin width data, we used windows containing 40 bins, and slid the window 2
 1756 bins at a time when taking measurements.

1757 For the 10ms bin width data, we used windows containing 40 bins, and slid the window
 1758 1 bin at a time when taking measurements (see table 3.1 for concise details).

1759 By continuing to use windows containing 40 bins, we retained statistical power but sac-
 1760 rificed the number of measurements taken.

1761 There was an interval between each trial with a grey image in place of the moving of
 1762 the moving bar stimulus. This interval varied in time. But we included some of this interval
 1763 when recording the data for each trial. We started recording the number of active neurons,
 1764 and the number of spikes from each neuron from 530ms before each trial until 1030ms after
 1765 each trial. This way, we could see the change in our measurements at the onset of a stimulus
 1766 and the end of stimulus presentation.

1767 As mentioned in section 3.3.2, we recorded the number of active neurons in each bin, and
 1768 the spike count for each neuron in each bin. The actual measurements we took using these
 1769 data in each window were as follows:

1770 **Moving average** The average number of active cells in each window.

1771 **Moving variance** The variance of the number of active cells in each window.

1772 **Average correlation** We measured the correlation between the spike counts of each pair of
 1773 cells in the ensemble, and took the average of these measurements.

1774 **Binomial p** We fitted a binomial distribution to the data in each window and recorded the
 1775 fitted probability of success, p in each case.

1776 **Beta-binomial α, β** We fitted a beta-binomial distribution to the data in each window, and
 1777 recorded the values of the fitted shape parameters, α and β , of each distribution.

1778 **Conway-Maxwell-binomial distribution p, ν** We fitted a Conway-Maxwell-binomial dis-
 1779 tribution to the data in each window, and recorded the fitted values of p and ν for each
 1780 distribution.

1781 **Log-likelihoods** We also recorded the log-likelihood of each of the fitted distributions for
 1782 each window.

1783 **3.3.4 Fano factor**

The *Fano factor* of a random variable is defined as the ratio of the variable's variance to its mean.

$$F = \frac{\sigma^2}{\mu} \quad (3.1)$$

1784 We measured the Fano factor of the spike count of a given cell by measuring the mean and
 1785 variance of the spike count across trials, and taking the ratio of those two quantities. When
 1786 calculated in this way the Fano factor can be used as a measure of neural variability that
 1787 controls for changes in the firing rate. This is similar to the calculation used in (Churchland
 1788 et al., 2010).

1789 **3.3.5 Probability Distributions suitable for modelling ensemble activity**

1790 We present here three different probability distributions that could be suitable to model the
 1791 number of active neurons in an ensemble. Each distribution has the set $\{0, \dots, n\}$ as its sup-
 1792 port, where n is the number of neurons in the ensemble. These are simple distributions with
 1793 either two or three parameters each. However, we regard n as known when using these dis-
 1794 tributions for modelling, so in effect each distribution has either one or two free parameters.

1795 **Association**

1796 *Association* between random variables is similar to the correlation between random variables
 1797 but is more general in concept. The correlation is a measure of association; and association
 1798 doesn't have a mathematical definition like correlation does. Essentially, the association
 1799 between two random variables is their tendency to take the same or similar values. Positively
 1800 associated variables tend to take the same value, and negatively associated variables tend to
 1801 take different values. In this research, we work with probability distributions of the number of
 1802 successes in a set of Bernoulli trials. These Bernoulli variables may or may not be associated.

1803 A probability distribution over the number of successes in n Bernoulli trials, where the
 1804 Bernoulli variables may be associated, could constitute a good model for the number of active
 1805 neurons in an ensemble of n neurons.

1806 **Binomial distribution**

The binomial distribution is a two parameter discrete probability distribution that can be thought of as a probability distribution the number of successes from n independent Bernoulli trials, each with the same probability of success. The parameters of the binomial distribution are n the number of trials, and $0 \leq p \leq 1$, the probability of success for each of these trials. A random variable with the binomial distribution can take values from $\{0, \dots, n\}$. The probability mass function of the distribution is

$$P(k; n, p) = \binom{n}{k} p^k (1 - p)^{n-k} \quad (3.2)$$

1807 As a model for the activity of a neuronal ensemble, the main problem with the binomial
 1808 distribution is that it treats each neuron, represented as a Bernoulli trial, as independent. It is
 1809 well known that neurons are not independent, and that correlated behaviour between neurons
 1810 is vital for representing sensory information (**cohen**). The binomial distribution falls short
 1811 in this regard, but it is useful as performance benchmark when assessing the performance of
 1812 other models.

1813 **Beta-binomial distribution**

1814 The beta distribution is the conjugate distribution of the binomial distribution. The beta-
 1815 binomial distribution is the combination of the beta distribution and the binomial distribution,
 1816 in that the probability of success for the binomial distribution is sampled from the beta dis-
 1817 tribution. This allows the beta-binomial distribution to capture some over dispersion relative
 1818 to the binomial distribution.

The beta-binomial distribution is a three parameter distribution, n the number of Bernoulli trials, and $\alpha \in \mathbb{R}_{>0}$ and $\beta \in \mathbb{R}_{>0}$ the shape parameters of the beta distribution. The probability mass function for the beta-binomial distribution is

$$P(k; n, \alpha, \beta) = \binom{n}{k} \frac{B(k + \alpha, n - k + \beta)}{B(\alpha, \beta)} \quad (3.3)$$

1819 where $B(\alpha, \beta)$ is the beta function.

This probability distribution can be reparametrised in a number of ways. One of which defines new parameters π and ρ by

$$\pi = \frac{\alpha}{\alpha + \beta} \quad (3.4)$$

$$\rho = \frac{1}{\alpha + \beta + 1} \quad (3.5)$$

1820 This reparametrisation is useful because π acts as a location parameter analogous to the p
 1821 parameter of a binomial distribution. A value of $\rho > 0$ indicates over-dispersion relative to a
 1822 binomial distribution.

1823 As a model for the activity of a neuronal ensemble, the beta-binomial distribution is
 1824 more suitable than a binomial distribution because the over-dispersion of the beta-binomial
 1825 distribution can be used to model positive association between the neurons. An extreme
 1826 example of this over-dispersion/positive association can be seen in figure 3.1b. In this figure,
 1827 the neurons are positively associated and so tend to take the same value, consequently the
 1828 probability mass of the beta-binomial distribution builds up close to $k = 0$ and $k = n$. It is
 1829 worth noting that the location parameter for each distribution has the same value, $p = \pi =$
 1830 0.5.

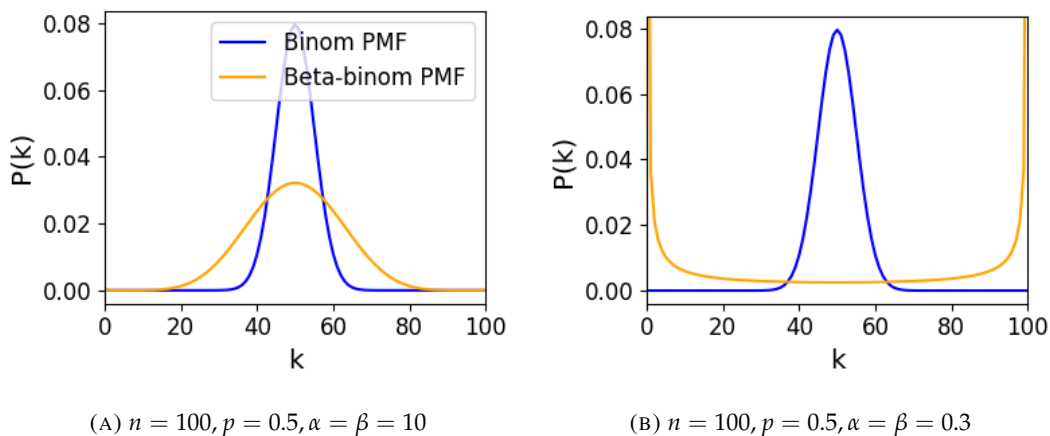
(A) $n = 100, p = 0.5, \alpha = \beta = 10$ (B) $n = 100, p = 0.5, \alpha = \beta = 0.3$

FIGURE 3.1: Figures showing the over-dispersion possible for a beta-binomial distribution relative to a binomial distribution. Parameters are shown in the captions.

1831 Conway-Maxwell-binomial distribution

1832 The Conway-Maxwell-binomial distribution (COMb distribution) is a three parameter generalisation of the binomial distribution that allows for over dispersion and under dispersion

relative to the binomial distribution. The parameters of the distribution are n the number of Bernoulli trials, and two shape parameters $0 \leq p \leq 1$, and $\nu \in \mathbb{R}$.

The probability mass function of the COMb distribution is

$$P(k; n, p, \nu) = \frac{1}{S(n, p, \nu)} \binom{n}{k}^{\nu} p^k (1-p)^{n-k} \quad (3.6)$$

where

$$S(n, p, \nu) = \sum_{j=0}^n \binom{n}{j}^{\nu} p^j (1-p)^{n-j} \quad (3.7)$$

The only difference between this PMF and the PMF for the standard binomial is the introduction of ν and the consequent introduction of the normalising function $S(n, p, \nu)$.

Indeed, if $\nu = 1$ the COMb distribution is identical to the binomial distribution with the same values for n and p . We can see in figure 3.2d that the KL-divergence $D_{KL}(P_{COMb}(n, p, \nu) || P_{Bin}(n, p)) = 0$ along the line where $\nu = 1$. The analytical expression for the divergence is

$$D_{KL}(P_{COMb}(k; n, p, \nu) || P_{Bin}(k; n, p)) = (\nu - 1) E_{P_{COMb}(k; n, p, \nu)} \left[\log \binom{n}{k} \right] \quad (3.8)$$

$$- \log S(n, p, \nu) \quad (3.9)$$

At $\nu = 1$, we have $S(n, p, 1)$ which is just the sum over the binomial PMF, so $S(n, p, 1) = 1$ and therefore $D_{KL}(P_{COMb}(n, p, \nu) || P_{Bin}(n, p)) = 0$.

If $\nu < 1$ the COMb distribution will exhibit over-dispersion relative to the binomial distribution. If $p = 0.5$ and $\nu = 0$ the COMb distribution is the discrete uniform distribution, and if $\nu < 0$ the mass of the COMb distribution will tend to build up near $k = 0$ and $k = n$. This over-dispersion represents positive association in the Bernoulli variables. An example of this over-dispersion can be seen in figure 3.2b.

If $\nu > 1$ the COMb distribution will exhibit under-dispersion relative to the binomial distribution. The larger the value of ν the more probability mass will build up at $n/2$ for even n , or at $\lfloor n/2 \rfloor$ and $\lceil n/2 \rceil$ for odd n . This under-dispersion represents negative association in the Bernoulli variables. An example of this under-dispersion can be seen in figure 3.2a.

It should be noted that the p parameter of the COMb distribution does not correspond to the mean of the distribution, as is the case for the binomial p parameter, and beta-binomial π parameter. That is, the COMb p parameter is not a location parameter. An illustration of this can be seen in figure 3.2c. This is because an interaction between the p and ν parameters skews the mean. There is no analytical expression for the mean of the COMb distribution.

ν	Relative dispersion	Association between neurons/variables
< 1	over	positive
1	none	none
> 1	under	negative

TABLE 3.2: Relative dispersion of the COMb distribution, and association between Bernoulli variables as represented by the value of the ν parameter.

1854 Since the COMb distribution has the potential to capture positive and negative associa-
 1855 tions between the neurons/Bernoulli variables, it should be an excellent candidate for mod-
 1856 elling the number of active neurons in a neuronal ensemble.

1857 We wrote a dedicated Python package to enable easy creation and fitting of COMb dis-
 1858 tribution objects. The format of the package imitates the format of other distribution objects
 1859 from the `scipy.stats` Python package. The COMb package can be found here:
 1860 https://github.com/thomasjdelaney/Conway_Maxwell_Binomial_Distribution

1861 3.3.6 Fitting

1862 We fitted binomial, beta-binomial, and Conway-Maxwell-binomial (COMb) distributions to
 1863 the neural activity in each of the overlapping windows covering each trial. To fit the distribu-
 1864 tions we minimised the appropriate negative log likelihood function using the data from the
 1865 window.

There is an analytical solution for maximum likelihood estimate of the binomial distribution's p parameter.

$$\hat{p} = \frac{1}{n} \sum_{i=1}^N k_i \quad (3.10)$$

1866 We minimised the negative log likelihood function of the beta-binomial distribution nu-
 1867 merically. We calculated the negative log likelihood for a sample directly, by taking the sum
 1868 of the log of the probability mass function for each value in the sample. We minimised the
 1869 negation of that function using the `minimise` function of the `scipy.optimize` Python
 1870 package.

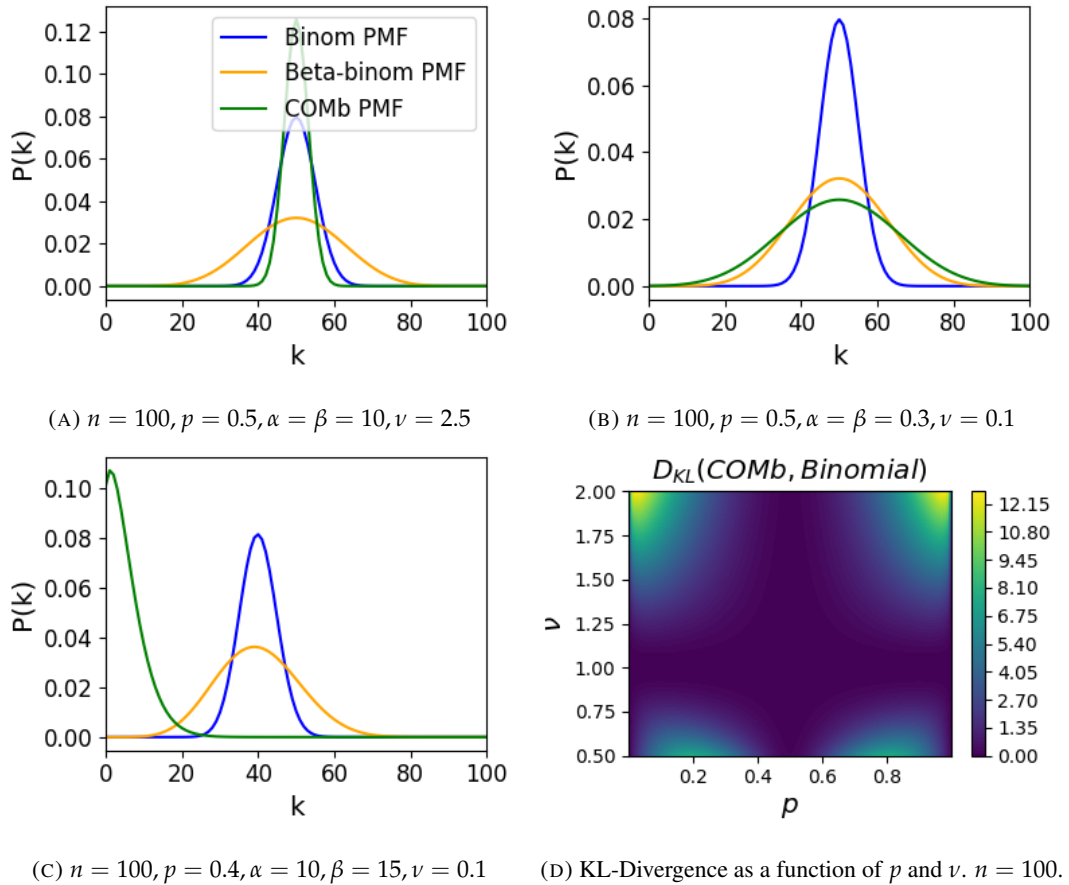


FIGURE 3.2: Figures showing (A) the under-dispersion and (B) over-dispersion permitted by the COMb distribution relative to a binomial distribution. (C) illustrates that the p parameter of the COMb distribution does not correspond to the mean of the distribution, as it does for the binomial and beta-binomial distributions. (D) shows a heatmap for the value of the Kullback-Liebler divergence between the COMb distribution and the standard binomial distribution with same value for n , as a function of p and ν . Parameters are shown in the captions.

The log likelihood function of the COMb distribution given some sample $\{k_1, \dots, k_N\}$ is

$$\ell(p, \nu | k_1, \dots, k_N) = N [n \log(1 - p) - \log S(n, p, \nu)] \quad (3.11)$$

$$+ \log \frac{p}{1 - p} \sum_{i=1}^N k_i \quad (3.12)$$

$$+ \nu \sum_{i=1}^N \log \binom{n}{k_i} \quad (3.13)$$

1871 We minimised the negation of this function using numerical methods. More specifically, we
 1872 used the `minimise` function of the `scipy.optimize` Python package.

1873 **3.3.7 Goodness-of-fit**

1874 After fitting, we measured the goodness-of-fit of each model/distribution with their log like-
 1875 lihood. We calculated this directly using the `logpmf` functions of the distribution objects in
 1876 Python.

1877 **3.4 Results**

1878 We defined a neuron as *active* in a time bin if it fires at least one spike during the time interval
 1879 covered by that bin. We measured the number of active neurons in the primary visual cortex
 1880 of a mouse in 1ms bins across 160 trials of a moving bar visual stimulus. We then slid a
 1881 100ms window across these 1ms bins taking measurements, and fitting distributions along
 1882 the way. We did the same for neurons in the thalamus, hippocampus, striatum, and motor
 1883 cortex. We repeated the analysis for 5ms time bins with 40 bin windows, and 10ms time bins
 1884 with 40 bin windows.

1885 **3.4.1 Increases in mean number of active neurons and variance in number of
 1886 active neurons at stimulus onset in some regions**

1887 We measured the average number of active neurons, and the variance of the number of active
 1888 neurons in a 100ms sliding window starting 500ms before stimulus onset until 1000ms after
 1889 stimulus onset. We found differences in the response across regions. There were no observed
 1890 changes in response to the stimulus in the motor cortex or the striatum. The changes in the
 1891 other regions are detailed below.

1892 Primary visual cortex

1893 We found a transient increase in both the average and variance of the number of active neu-
1894 rons at stimulus onset, followed by a fall to pre-stimulus levels, followed by another transient
1895 increase (see figure 3.3). The oscillation in both of these measurements appear to reflect the
1896 frequency of the stimulus (see Data section 3.2.1), and it is known that stimulus structure
1897 can influence response structure (“parencite –litwinkumar”). We see a similar but lower
1898 amplitude oscillation at the end of the stimulus presentation.

1899 Hippocampus

1900 In the hippocampus we observed a transient increase in the average number of active neurons
1901 and in the variance of the number of active neurons at stimulus onset (see figure 3.4). The
1902 increase lasted about 125ms, and the subsequent fall to baseline took the a similar amount of
1903 time.

1904 Thalamus

1905 In the thalamus we observed a transient increase in the both the average and variance of
1906 the number of active neurons on stimulus onset, followed by a fall to pre-stimulus levels,
1907 followed by a sustained increase until the stimulus presentation ends.

1908 As one you might expect for a visual stimulus, the change in the average number of active
1909 neurons was greatest in the primary visual cortex. In this region, this quantity doubled on
1910 stimulus onset. In contrast, in the hippocampus and the thalamus, the average number of
1911 active neurons only increased by a fraction of the unstimulated baseline value. The duration
1912 of the response in V1 and the hippocampus at stimulus onset was 300 – 400ms, but the
1913 response in the thalamus appeared to last for the duration of stimulus presentation. The V1
1914 also showed a change in the average number of active neurons at stimulus end. The change
1915 was similar to that observed at stimulus onset, but smaller in magnitude (see figures ??)

**1916 3.4.2 Conway-Maxwell-binomial distribution is usually a better fit than bino-
1917 mial or beta-binomial**

1918 Since the Conway-Maxwell-binomial distribution has not been fitted to neuronal data before,
1919 it is not clear that it would be a better fit than the binomial or beta-binomial distributions.
1920 In order to find out which parametric distribution was the best fit for the largest proportion
1921 of our data, we fit a binomial, a beta-binomial, and a Conway-Maxwell-binomial (COMb)

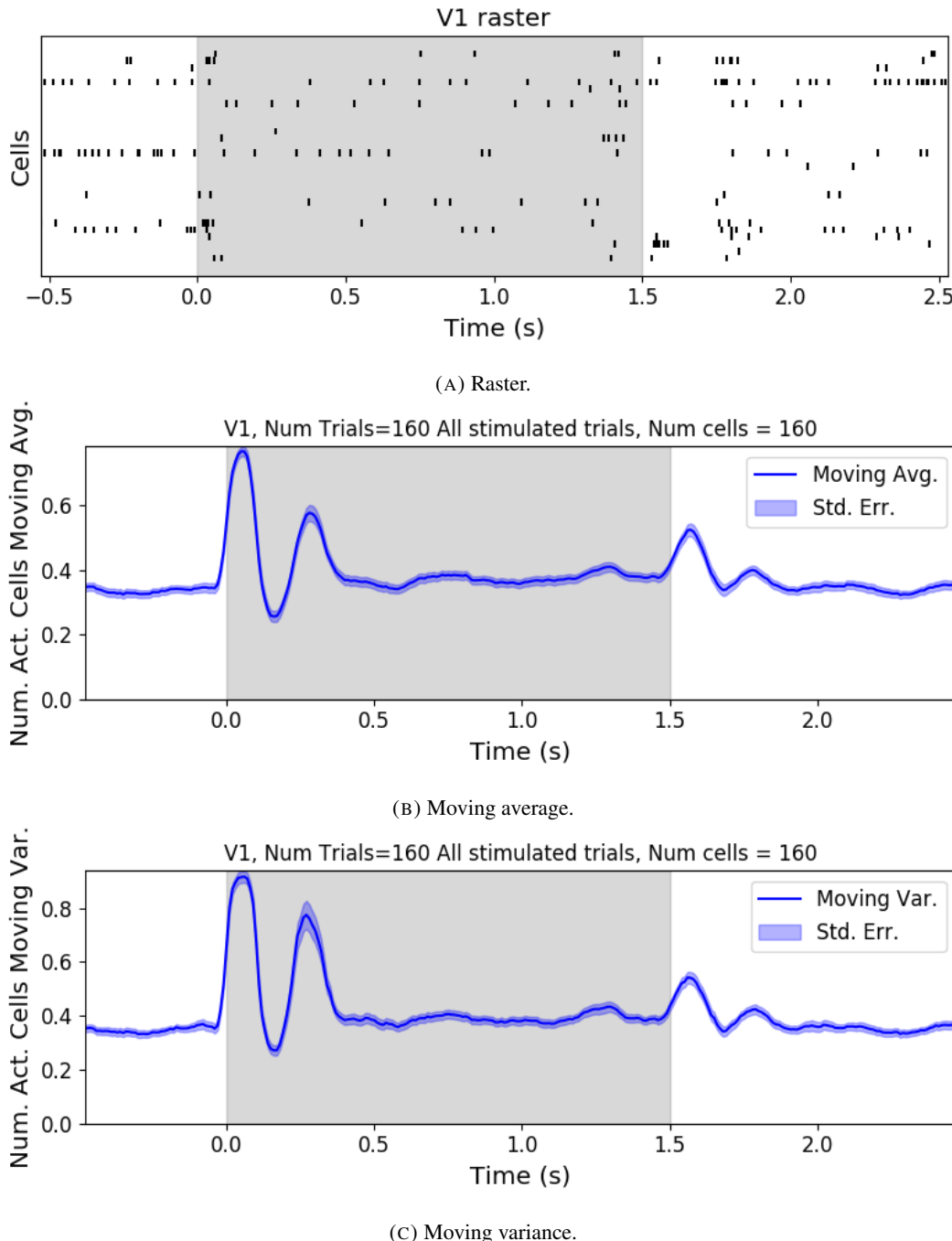


FIGURE 3.3: (A) Raster plot showing the spikes fired by 33 randomly chosen neurons in the primary visual cortex. (B-C) (B) average and (C) variance of the number of active neurons, measured using a sliding window 100ms wide, split into 100 bins. The midpoint of the time interval for each window is used as the timepoint (x-axis point) for the measurements using that window. The grey shaded area indicates the presence of a visual stimulus. The opaque line is an average across the 160 trials that included a visual stimulus of any kind. We can see a transient increase in the average number of active neurons and the variance of this number, followed by a fluctuation and another increase.

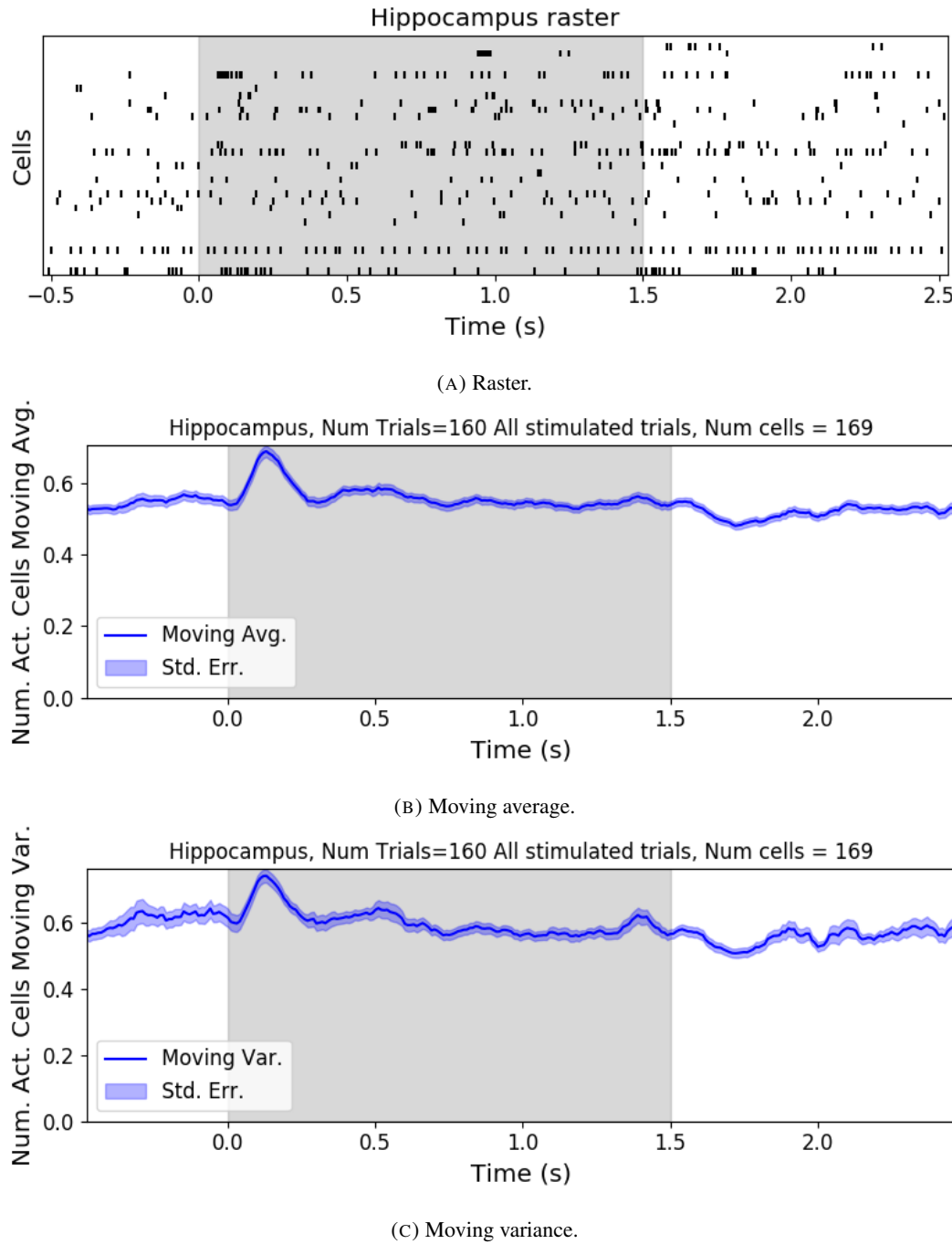


FIGURE 3.4: (A) Raster plot showing the spikes fired by 33 randomly chosen neurons in the hippocampus. (B-C) (B) average and (C) variance of the number of active neurons, measured using a sliding window 100ms wide, split into 100 bins. The midpoint of the time interval for each window is used as the timepoint (x-axis point) for the measurements using that window. The grey shaded area indicates the presence of a visual stimulus. The opaque line is an average across the 160 trials that included a visual stimulus of any kind. We can see a transient increase in the average number of active neurons and the variance of this number at stimulus onset.

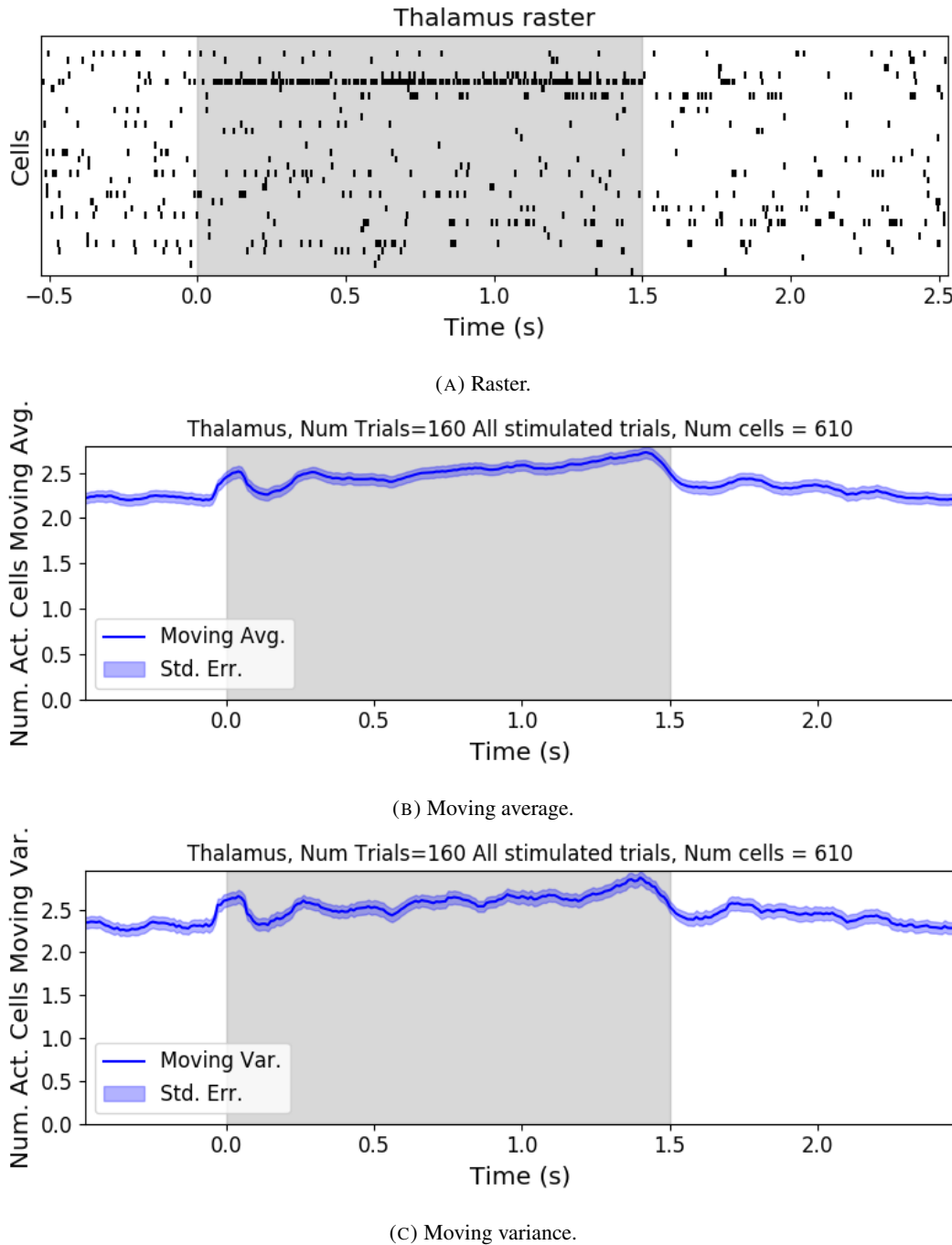


FIGURE 3.5: (A) Raster plot showing the spikes fired by 33 randomly chosen neurons in the thalamus. (B-C) (B) average and (C) variance of the number of active neurons, measured using a sliding window 100ms wide, split into 100 bins. The midpoint of the time interval for each window is used as the timepoint (x-axis point) for the measurements using that window. The grey shaded area indicates the presence of a visual stimulus. The opaque line is an average across the 160 trials that included a visual stimulus of any kind. We can see an immediate increase at stimulus onset, a subsequent fall, and another sustained increase until the stimulus presentation ends.

distribution to each window for each bin width, and each region. Then we assessed the goodness-of-fit of each distribution by calculating the log-likelihood of each fitted distribution using the associated sample. We measured the proportion of samples for which each distribution was the best fit, for each bin width value and each region.

We found that the COMb distribution was the best fit for most of the samples regardless of bin width or region. The bin width had an effect on the number of samples for which the COMb distribution was the best fit. The results are summarised in table 3.3. For a bin width of 1ms, the COMb distribution was the best fit for over 90% of samples, the beta-binomial distribution was the best fit for less than 10% of samples, and the binomial distribution was the best fit for less than 1% of samples, across regions. For 5ms bins, the COMb distribution was the best fit for 70 – 80% of samples, the beta-binomial distribution was the best fit for 20 – 30% of the samples, and again the binomial distribution was the best fit for less than 1% of samples, across regions. Finally, for 10ms bins, the COMb distribution was the best fit for 53 – 80% of samples, the beta-binomial distribution was the best fit for 20 – 47% of the samples, and the binomial distribution was the best fit for less than 0.1% of samples, across regions.

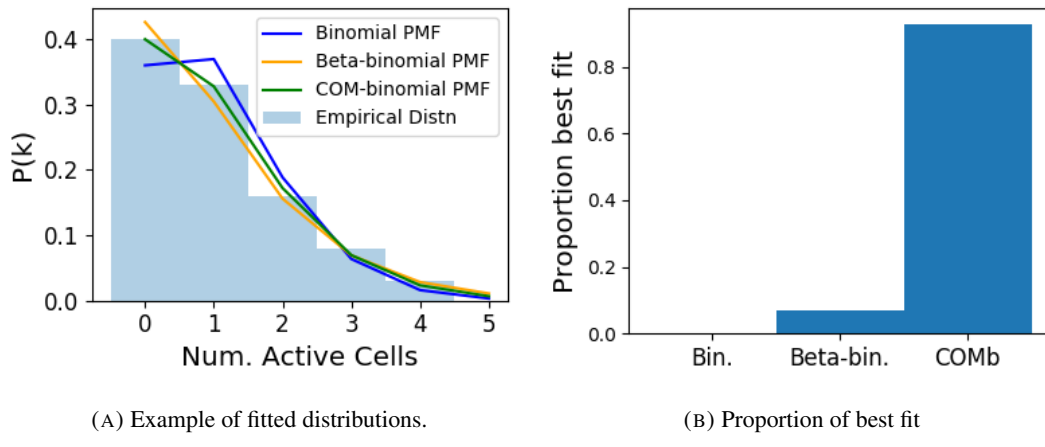


FIGURE 3.6: (A) An example of the binomial, beta-binomial, and Conway-Maxwell-binomial distributions fitted to a sample of neural activity. The Conway-Maxwell-binomial distribution is the best fit in this case. The histogram shows the empirical distribution of the sample. The probability mass function of each distribution is indicated by a different coloured line. (B) Across all samples in all trials, the proportion of samples for which each fitted distribution was the best fit. The Conway-Maxwell-binomial distribution was the best fit for 93% of the samples taken from V1 using a bin width of 1ms.

Bin Width (ms)	Binomial	Beta-binomial	COMb
1ms	< 1%	< 10%	> 90%
5ms	< 0.1%	20 – 30%	70 – 80%
10ms	< 0.1%	20 – 47%	53 – 80%

TABLE 3.3: Proportion of samples for which each distribution was the best fit, grouped by bin width. The COMb distribution is the best fit most of the time.

1938 3.4.3 Conway-Maxwell-binomial distribution captures changes in association 1939 at stimulus onset

1940 We fit a Conway-Maxwell-binomial (COMb) distribution to the number of active neurons in
1941 the 1ms time bins in a 100ms sliding window. We also measured the correlation coefficient
1942 between the spike counts of all possible pairs of neurons, and took the average of these
1943 coefficients. We did this for all the trials with a visual stimulus. We observed a reduction in
1944 the COMb distribution's ν parameter at stimulus onset from around 1 to between 0 and 1 (see
1945 figure 3.7a). A value of ν less than 1 indicates positive association between the neurons (see
1946 section 3.3.5). We might expect to see this positive association reflected in the correlation
1947 coefficients, but this is not the case. We see no change in the time series of average correlation
1948 measures at stimulus onset.

1949 This may be due to the very short time bin we used in this case. We know that using
1950 small time bins can artificially reduce correlation measurements (**cohen**). In this case, fitting
1951 the COMb distribution may be a useful way to measure association in a neuronal ensemble
1952 over very short timescales (< 10ms).

1953 3.4.4 Replicating stimulus related quenching of neural variability

1954 Churchland et al. (2010) inspected the effect of a stimulus on neural variability. One of the
1955 measures of neural variability that they employed was the Fano factor of the spike counts of
1956 individual cells (see section 3.3.4). They found a reduction in neural variability as measured
1957 by the Fano factor in various cortical areas in a macaque at the onset of various visual stimuli,
1958 or a juice reward (Churchland et al., 2010).

1959 We measured the Fano factor of the spike count of each cell in each brain region, during
1960 each trial. We measured the mean and standard error of these Fano factors from 500ms
1961 before stimulus onset until 1000ms after stimulus end. For the primary visual cortex, we
1962 found a transient reduction in the Fano factor immediately after stimulus onset. We used
1963 a Mann-Whitney U test to check that the Fano factors measured in a window starting at

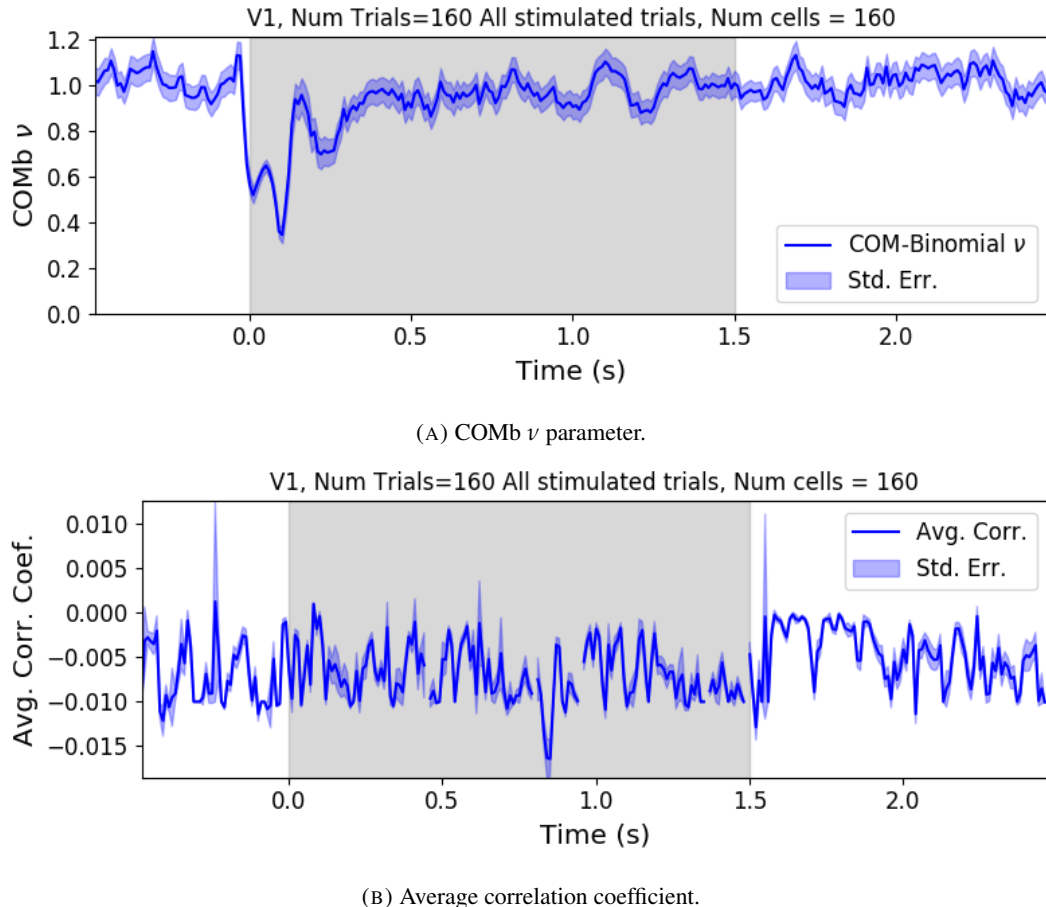


FIGURE 3.7: (A) We fit a Conway-Maxwell-binomial distribution to the number of active neurons in 1ms time bins of a 100ms sliding window. We did this for all trials with a visual stimulus and took the average across those trials. We see a transient drop in value for the distribution’s ν parameter at stimulus onset. This shows an increase in association between the neurons. (B) We measured the correlation coefficient between the spike counts of all possible pairs of neurons in the same sliding window. We took the average of those coefficients. We also did this for every visually stimulated trial, and took the average across trials. The increase in association is not reflected with an increase in average correlation.

1964 stimulus onset and ending 100ms later were significantly lower than the factors measured
 1965 in a window ending at stimulus onset ($p < 0.001$, see figure 3.8a). We did not get this
 1966 statistically significant result in any other region.

1967 Our findings agree with those of Churchland et al. for the primary visual cortex. However
 1968 Churchland also found a reduction in the Fano factor in the dorsal premotor cortex (PMd) at
 1969 stimulus onset. Our measurements from the mouse motor cortex show no change at stimulus
 1970 onset (see figure 3.8b). This could indicate some difference in the functionality of the motor
 1971 cortex in a macaque and the motor cortex of a mouse.

1972 Similar to these findings in the Fano factor, we found a reduction in the ν parameter of
 1973 the COMB distribution on stimulus onset in V1 (figure 3.7a) and in no other region from

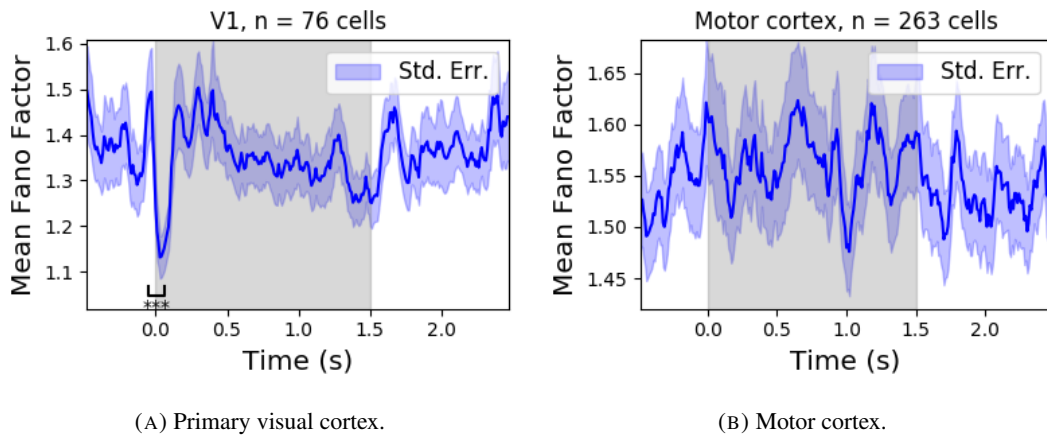


FIGURE 3.8: (A) The mean Fano factor of the spike counts of the cells in the primary visual cortex. Means were taken across cells first, then across trials. There was a significant decrease in the Fano factors immediately after stimulus onset. (B) The mean Fano factor of the spike counts of the cells in the motor cortex. No significant change in measurements at any point.

1974 which we had data. Specifically, the ν parameter reduced from around 1, to between 1 and 0.
 1975 This represents a change from no association between the neurons, to a positive association.
 1976 It is possible that this positive association may be responsible for the reduction in the Fano
 1977 factor.

1978 3.5 Discussion

1979 Our aim in this research was to develop a new statistical method for analysing the activity
 1980 of a neuronal ensemble at very short timescales. We wanted our method to use information
 1981 taken from the whole ensemble, but we also wanted the method to be quick and easy to
 1982 implement. It is likely that analysis methods with these characteristics will become valuable
 1983 as electrophysiological datasets include readings from more cells over longer time periods. In
 1984 this case, we used the number of active, or spiking, neurons in a very short time bin ($< 10\text{ms}$)
 1985 as a measure of ensemble activity.

1986 First of all, we showed that there were changes in response that we could model at these
 1987 very short time scales in some of the brain regions from which we had recordings. We ob-
 1988 served changes in the average number of active neurons, and the variance of the number of
 1989 active neurons in three different brain regions in response to visual stimuli. Since we know
 1990 that correlated behaviour is associated with sensory perception (deCharms and Merzenich,
 1991 1996), we might hope to measure the pairwise correlations within the neuronal population
 1992 in order to further investigate these responses. But, using such short time bins can produce
 1993 artificially small spike count correlation measurements (**cohen**). Overcoming this limitation

1994 was one of our objectives for our new method. In order to do this, we abandoned the idea
1995 of measuring the correlations directly and embraced the concept of *association*. In order to
1996 quantify the association between neurons, we used the Conway-Maxwell-binomial distribu-
1997 tion to model the number of active (spiking) neurons in an ensemble as a sum of possibly
1998 associated Bernoulli random variables.

1999 We showed that the Conway-Maxwell-binomial distribution performed better than the
2000 more common options of the binomial and beta-binomial distributions. Furthermore, we
2001 showed that the positively associated behaviour between neurons in the primary visual cortex
2002 could be captured by fitting a Conway-Maxwell-binomial distribution, but was not captured
2003 by the more standard approach of measuring the spike count correlation. The associated
2004 behaviour could not be measured using spike count correlations, because of the very short
2005 bins required to capture short timescale behaviour.

2006 We replicated a famous result from Churchland et al (2010) relating to the quenching of
2007 neural variability in cortical areas at stimulus onset, and in doing so, we established a corre-
2008 spondence between the association quantifying parameter of the Conway-Maxwell-binomial
2009 (COMB) distribution and the neural variability as measured by the Fano factor. We found a
2010 reduction in the ν parameter of the COMB distribution at stimulus onset, indicating a change
2011 from no association to positive association between neurons in V1. We found a corresponding
2012 reduction in the Fano factor of the individual cells in V1. The positive association between
2013 neurons induced by the stimulus would constrain the neurons to fire at the same time. The
2014 stimulus also induced a larger number of neurons to spike. These two actions combined could
2015 cause an increase in the firing rate of individual cells that is greater in magnitude than the in-
2016 crease in firing rate variability. If this is indeed the case, then the association as captured by
2017 the COMB distribution could be regarded as one of the ‘natural parameters’ of the ensemble
2018 response for short timescales. That is, a quantity that directly measures some aspect of the
2019 behaviour of the ensemble. In this case, it the correlated behaviour of the individual neurons
2020 is captured.

2021 This work could be just a first step in creating analysis methods based on the Conway-
2022 Maxwell-binomial distribution, or similar statistical models. One way to extend the method
2023 would be to pair it up with the ‘Population Tracking model’ (O’Donnell et al., 2017). This
2024 model attempts to characterise the interaction between an ensemble and each member of the
2025 ensemble by quantifying the probability of spiking for a given a cell, given the number of
2026 active cells in the whole population. Combining this model with the COMB distribution
2027 would give us a model that could accurately fit the number of active neurons at any moment,

2028 and that gives a probability of firing for each cell, and therefore probabilities for full spiking
2029 patterns, without adding a huge number of parameters to fit.

2030 A more complex way to extend the model would be to fit a Conway-Maxwell-binomial
2031 distribution to data recorded from multiple brain regions simultaneously, with a different fit
2032 for each region, then to analyse the temporal relationship between the fitted parameters of
2033 each region. If we analysed the time series of the COMB distribution parameters from the
2034 different regions, looking at cross-correlations between regions, this may give some results
2035 relating to the timescales in which information is processed in different brain regions.

²⁰³⁶ **Chapter 4**

²⁰³⁷ **Studies with practical limitations &**
²⁰³⁸ **negative results**

2039

UNIVERSITY OF BRISTOL

2040

Abstract

2041

Engineering

2042

Department of Computer Science

2043

Doctor of Philosophy

2044

Investigating, implementing, and creating methods for analysing large neuronal ensembles

2045

by Thomas J. DELANEY

2047

Here I will present some details on research topics that I started, but that unfortunately did not lead anywhere useful. There are two pieces of research, based on two papers. Each paper is related to the overall theme of my PhD of analysing and modelling behaviours of populations of neurons. The first part is based on a model of parallel spike trains including higher order interactions by Shimazaki et al (2012). The second part is based on a multiscale model for making inferences on hierarchical data.

2053 **4.1 Dynamic state space model of pairwise and higher order neu-**
2054 **ronal correlations**

2055 In their paper Shimazaki et al (2012) aimed to model spike trains from populations of neurons
2056 in parallel, with pairwise and higher order dynamic interactions between the trains. They
2057 modelled the spike trains as multi-variate binary processes using a log-linear model, and they
2058 extracted spike interaction parameters using a Bayesian filter/EM-algorithm. They developed
2059 a goodness-of-fit measure for the model to test if including these higher order correlations
2060 is necessary for an accurate model. Their measure was based on the Bayes factor but they
2061 also assessed the suitability of higher order models using the AIC and BIC. So the increase
2062 in the number of parameters associated with fitting higher order interactions was taken into
2063 account. They tested the performance of the model on synthetic data with known higher
2064 order correlations. They used the model to look for higher order correlations in data from
2065 awake behaving animals. They use the model to demonstrate dynamic appearance of higher
2066 order correlations in the monkey motor cortex (**shimazaki**).

2067 We used the available Python repository to implement the model, and we successfully
2068 worked through the tutorial provided. But we found that the model did not scale well to
2069 larger populations. We attempted to fit the model to a population of 10 neurons and found we
2070 didn't manage to finish the process. Since, our goal was to find a model to scale to hundreds
2071 or thousands of neurons, we decided that this model was no longer worth pursuing.

2072 **4.2 A multiscale model for hierarchical data applied to**
2073 **neuronal data**

2074 In their paper Kolacayk et al (2001) developed a framework for a modelling hierarchically
2075 aggregated data, and making inferences based on a model arising from this framework. They
2076 assumed that a hierarchical aggregation existed on the data in question, where each element at
2077 each level of the hierarchy had some associated measurements, an associated mean process,
2078 which was the expected value of these measurements. They also assumed that the measure-
2079 ments of each parent were equal to the sum of the measurements from all of its children.
2080 They showed that these assumptions gave rise to a relationship between parent and child
2081 measurements across all levels of the hierarchy, where the product of the likelihood of the
2082 parameters of the lowest level of the hierarchy can be expressed as products of conditional
2083 likelihoods of the elements of higher levels of the hierarchy (**kolacayk**).

2084 They gave examples of these expressions for measurements sampled from Gaussian dis-
2085 tributions, and Poisson distributions, and showed the definitions of the hierarchical param-
2086 eters which reparametrise the distribution of these data taking the hierarchy into account.
2087 They go on to suggest prior distributions for this multiscale model, and integrate these priors
2088 to give posterior distributions for the measurements from each element at each level in the hi-
2089 erarchy, and expressions for the MAP estimated parameters of each the associated processes
2090 (**kolacayk**).

2091 We implemented their model in Python by creating some synthetic data from Poisson
2092 distributions, and defining a hierarchy by agglomerating these data. We calculated the MAP
2093 estimates using our knowledge of the hierarchy, and using the expressions given in the paper.
2094 We found that the MAP estimates were far less accurate than would be achieved by simply
2095 ignoring the hierarchy during estimation, and using a maximum likelihood approach. After
2096 that, we decided to move on.

2097 **4.3 Discussion**

2098 Ideas (not in order):

- 2099 • Calcium imaging limitations (spike inference not always possible)
- 2100 • Judging by Greenberg biophysical modelling is the way to go.
- 2101 • our fluorescence model could be useful in a number of situations.
- 2102 • Applied new network science to new electrophysiological dataset.
- 2103 • Abandon calcium
- 2104 • Multi region calcium imaging dataset would be useful?
- 2105 • Results might be intuitive, but are new nonetheless (as far as I know)
- 2106 • Potential for more network science applications?
- 2107 • Applied the COMB distribution to neuronal data for the first time.
- 2108 • captures correlated behaviour by quantifying *association*.
- 2109 • Abandon correlations.
- 2110 • coupling with existing models could yield some nice models.
- 2111 • More statistical invention could be useful.

2112 Bibliography

- 2113 Allen, William E. et al. (2019). “Thirst regulates motivated behavior through modulation of
 2114 brainwide neural population dynamics”. In: *Science* 364.6437. ISSN: 0036-8075. DOI:
 2115 [10.1126/science.aav3932](https://doi.org/10.1126/science.aav3932). eprint: <https://science.sciencemag.org/content/364/6437/eaav3932.full.pdf>. URL: <https://science.sciencemag.org/content/364/6437/eaav3932>.
- 2116 Baadel, S., F. Thabtah, and J. Lu (2016). “Overlapping clustering: A review”. In: *2016 SAI Computing Conference (SAI)*, pp. 233–237. DOI: [10.1109/SAI.2016.7555988](https://doi.org/10.1109/SAI.2016.7555988).
- 2117 Baldassano, Christopher et al. (2017). “Discovering Event Structure in Continuous Narrative Perception and Memory”. In: *Neuron* 95.3, 709 –721.e5. ISSN: 0896-6273. DOI: <https://doi.org/10.1016/j.neuron.2017.06.041>. URL: <http://www.sciencedirect.com/science/article/pii/S0896627317305937>.
- 2118 Bartol, Thomas M. et al. (2015). “Computational reconstitution of spine calcium transients from individual proteins”. In: *Frontiers in Synaptic Neuroscience* 7, p. 17. ISSN: 1663-3563. DOI: [10.3389/fnsyn.2015.00017](https://doi.org/10.3389/fnsyn.2015.00017). URL: <https://www.frontiersin.org/article/10.3389/fnsyn.2015.00017>.
- 2119 Berens, Philipp et al. (May 2018). “Community-based benchmarking improves spike rate inference from two-photon calcium imaging data”. In: *PLOS Computational Biology* 14.5, pp. 1–13. DOI: [10.1371/journal.pcbi.1006157](https://doi.org/10.1371/journal.pcbi.1006157). URL: <https://doi.org/10.1371/journal.pcbi.1006157>.
- 2120 Bezanson, Jeff et al. (Sept. 2012). “Julia: A Fast Dynamic Language for Technical Computing”. In: *MIT*.
- 2121 Chen, Tsai-Wen et al. (July 2013). “Ultrasensitive fluorescent proteins for imaging neuronal activity”. In: *Nature* 499, 295–300. DOI: [10.1038/nature12354](https://doi.org/10.1038/nature12354). URL: <https://doi.org/10.1038/nature12354>.
- 2122 Churchland, Mark M. et al. (2010). “Stimulus onset quenches neural variability: a widespread cortical phenomenon”. eng. In: *Nature neuroscience* 13.3. 20173745[pmid], pp. 369–378. ISSN: 1546-1726. DOI: [10.1038/nn.2501](https://doi.org/10.1038/nn.2501). URL: <https://pubmed.ncbi.nlm.nih.gov/20173745>.

- 2141 Cohen, Marlene R. and Adam Kohn (2011). “Measuring and interpreting neuronal correla-
2142 tions”. In: *Nature Neuroscience* 14.7, pp. 811–819. ISSN: 1546-1726. DOI: [10.1038/nn.2842](https://doi.org/10.1038/nn.2842). URL: <https://doi.org/10.1038/nn.2842>.
- 2144 Cohen, Marlene R. and John H. R. Maunsell (2009). “Attention improves performance pri-
2145 marily by reducing interneuronal correlations”. eng. In: *Nature neuroscience* 12.12. 19915566[pmid],
2146 pp. 1594–1600. ISSN: 1546-1726. DOI: [10.1038/nn.2439](https://doi.org/10.1038/nn.2439). URL: <https://pubmed.ncbi.nlm.nih.gov/19915566/>.
- 2148 deCharms, R. Christopher and Michael M. Merzenich (1996). “Primary cortical represen-
2149 tation of sounds by the coordination of action-potential timing”. In: *Nature* 381.6583,
2150 pp. 610–613. ISSN: 1476-4687. DOI: [10.1038/381610a0](https://doi.org/10.1038/381610a0). URL: <https://doi.org/10.1038/381610a0>.
- 2152 Deneux, Thomas et al. (July 2016). “Accurate spike estimation from noisy calcium signals
2153 for ultrafast three-dimensional imaging of large neuronal populations *in vivo*”. In: *Nature
2154 Communications* 7.1. DOI: [10.1038/ncomms12190](https://doi.org/10.1038/ncomms12190). URL: <https://doi.org/10.1038/ncomms12190>.
- 2156 Faas, G. C. et al. (Mar. 2011). “Calmodulin as a direct detector of Ca²⁺ signals”. In: *Nature
2157 neuroscience* 14.3, pp. 301–304. DOI: [10.1038/nn.2746](https://doi.org/10.1038/nn.2746). URL: <https://doi.org/10.1038/nn.2746>.
- 2159 Fiala, John C. and Kristen M. Harris (1999). *Dendrite Structure*.
- 2160 Flach, Boris (Sept. 2013). “A Class of Random Fields on Complete Graphs with Tractable
2161 Partition Function”. In: *IEEE transactions on pattern analysis and machine intelligence*
2162 35, pp. 2304–6. DOI: [10.1109/TPAMI.2013.99](https://doi.org/10.1109/TPAMI.2013.99).
- 2163 Fosdick, Bailey et al. (Aug. 2016). “Configuring Random Graph Models with Fixed Degree
2164 Sequences”. In: *SIAM Review* 60. DOI: [10.1137/16M1087175](https://doi.org/10.1137/16M1087175).
- 2165 Friedrich, Johannes and Liam Paninski (2016). “Fast Active Set Methods for Online Spike
2166 Inference from Calcium Imaging”. In: *Advances in Neural Information Processing Sys-
2167 tems* 29. Ed. by D. D. Lee et al. Curran Associates, Inc., pp. 1984–1992. URL: <http://papers.nips.cc/paper/6505-fast-active-set-methods-for-online-spike-inference-from-calcium-imaging.pdf>.
- 2170 Ganmor, Elad, Ronen Segev, and Elad Schneidman (2011). “Sparse low-order interaction
2171 network underlies a highly correlated and learnable neural population code”. In: *Proceed-
2172 ings of the National Academy of Sciences* 108.23, pp. 9679–9684. ISSN: 0027-8424. DOI:
2173 [10.1073/pnas.1019641108](https://doi.org/10.1073/pnas.1019641108). eprint: <https://www.pnas.org/content/>

- 2174 108/23/9679.full.pdf. URL: <https://www.pnas.org/content/108/23/9679>.
- 2175
- 2176 Girard, P., J. M. Hupé, and J. Bullier (2001). “Feedforward and Feedback Connections Between Areas V1 and V2 of the Monkey Have Similar Rapid Conduction Velocities”. In: *Journal of Neurophysiology* 85.3. PMID: 11248002, pp. 1328–1331. DOI: [10.1152/jn.2001.85.3.1328](https://doi.org/10.1152/jn.2001.85.3.1328). eprint: <https://doi.org/10.1152/jn.2001.85.3.1328>. URL: <https://doi.org/10.1152/jn.2001.85.3.1328>.
- 2177
- 2178
- 2179
- 2180
- 2181 Greenberg, David et al. (Nov. 2018). “Accurate action potential inference from a calcium sensor protein through biophysical modeling.” in: DOI: [10.1101/479055](https://doi.org/10.1101/479055).
- 2182
- 2183 Gründemann, Jan et al. (2019). “Amygdala ensembles encode behavioral states”. In: *Science* 364.6437. ISSN: 0036-8075. DOI: [10.1126/science.aav8736](https://doi.org/10.1126/science.aav8736). eprint: <https://science.sciencemag.org/content/364/6437/eaav8736.full.pdf>. URL: <https://science.sciencemag.org/content/364/6437/eaav8736>.
- 2184
- 2185
- 2186
- 2187
- 2188 Humphries, Mark et al. (Jan. 2019). “Spectral rejection for testing hypotheses of structure in networks”. In:
- 2189
- 2190 Humphries, Mark D. (2011). “Spike-Train Communities: Finding Groups of Similar Spike Trains”. In: *Journal of Neuroscience* 31.6, pp. 2321–2336. ISSN: 0270-6474. DOI: [10.1523/JNEUROSCI.2853-10.2011](https://doi.org/10.1523/JNEUROSCI.2853-10.2011). eprint: <https://www.jneurosci.org/content/31/6/2321.full.pdf>. URL: <https://www.jneurosci.org/content/31/6/2321>.
- 2191
- 2192
- 2193
- 2194
- 2195 Jun, James J. et al. (2017). “Fully integrated silicon probes for high-density recording of neural activity”. In: *Nature* 551.7679, pp. 232–236. ISSN: 1476-4687. DOI: [10.1038/nature24636](https://doi.org/10.1038/nature24636). URL: <https://doi.org/10.1038/nature24636>.
- 2196
- 2197
- 2198 Kilhoffer, Marie-Claude et al. (Sept. 1992). “Use of Engineered Proteins With Internal Tryptophan Reporter Groups and Perturbation Techniques to Probe the Mechanism of Ligand-Protein Interactions: Investigation of the Mechanism of Calcium Binding to Calmodulin”. In: *Biochemistry* 31.34, pp. 8098–8106. DOI: [10.1021/bi00149a046](https://doi.org/10.1021/bi00149a046). URL: <https://doi.org/10.1021/bi00149a046>.
- 2199
- 2200
- 2201
- 2202
- 2203 Koch, Christoff (1999). *Biophysics of Computation: Information Processing in Single Neurons*. Oxford University Press. ISBN: ISBN 0-19-510491-9.
- 2204
- 2205 Lee, Suk-HO et al. (July 2000). “Differences in Ca²⁺ buffering properties between excitatory and inhibitory hippocampal neurons from the rat”. In: *The Journal of Physiology* 525. DOI: [10.1111/j.1469-7793.2000.t01-3-00405.x](https://doi.org/10.1111/j.1469-7793.2000.t01-3-00405.x).
- 2206
- 2207

- 2208 Litwin-Kumar, Ashok, Maurice Chacron, and Brent Doiron (Sept. 2012). “The Spatial Struc-
2209 ture of Stimuli Shapes the Timescale of Correlations in Population Spiking Activity”.
2210 In: *PLoS computational biology* 8, e1002667. DOI: [10.1371/journal.pcbi.1002667](https://doi.org/10.1371/journal.pcbi.1002667).
- 2212 Maravall, M et al. (May 2000). “Estimating intracellular calcium concentrations and buffer-
2213 ing without wavelength ratioing”. In: *Biophysical Journal* 78.5, pp. 2655–2667. DOI:
2214 [10.1016/S0006-3495\(00\)76809-3](https://doi.org/10.1016/S0006-3495(00)76809-3). URL: [https://doi.org/10.1016/S0006-3495\(00\)76809-3](https://doi.org/10.1016/S0006-3495(00)76809-3).
- 2216 Maugis, Pa (Jan. 2014). “Event Conditional Correlation: Or How Non-Linear Linear Depen-
2217 dence Can Be”. In:
- 2218 Meilă, Marina (2007). “Comparing clusterings—an information based distance”. In: *Journal
of Multivariate Analysis* 98.5, pp. 873 –895. ISSN: 0047-259X. DOI: <https://doi.org/10.1016/j.jmva.2006.11.013>. URL: <http://www.sciencedirect.com/science/article/pii/S0047259X06002016>.
- 2222 Murray, John D. et al. (2014). “A hierarchy of intrinsic timescales across primate cortex”.
2223 In: *Nature Neuroscience* 17.12, pp. 1661–1663. ISSN: 1546-1726. DOI: [10.1038/nn.3862](https://doi.org/10.1038/nn.3862). URL: <https://doi.org/10.1038/nn.3862>.
- 2225 Neher, E. and G. J. Augustine (1992). “Calcium gradients and buffers in bovine chromaffin
2226 cells”. eng. In: *The Journal of physiology* 450. 1331424[pmid], pp. 273–301. ISSN: 0022-
2227 3751. DOI: [10.1113/jphysiol.1992.sp019127](https://doi.org/10.1113/jphysiol.1992.sp019127). URL: <https://pubmed.ncbi.nlm.nih.gov/1331424>.
- 2229 O’Donnell, Cian et al. (Jan. 2017). “The population tracking model: a simple, scalable statis-
2230 tical model for neural population data”. English. In: *Neural Computation* 29.1, pp. 50–
2231 93. ISSN: 0899-7667. DOI: [10.1162/NECO_a_00910](https://doi.org/10.1162/NECO_a_00910).
- 2232 Patterson, Carolyn A. et al. (2014). “Similar adaptation effects in primary visual cortex and
2233 area MT of the macaque monkey under matched stimulus conditions”. In: *Journal of Neu-
2234 rophysiology* 111.6. PMID: 24371295, pp. 1203–1213. DOI: [10.1152/jn.00030.2013](https://doi.org/10.1152/jn.00030.2013). eprint: <https://doi.org/10.1152/jn.00030.2013>. URL: <https://doi.org/10.1152/jn.00030.2013>.
- 2237 Pnevmatikakis, E.A. et al. (Jan. 2016). “Simultaneous Denoising, Deconvolution, and Demix-
2238 ing of Calcium Imaging Data”. In: *Neuron* 89.2, pp. 285–299. DOI: [10.1016/j.neuron.2015.11.037](https://doi.org/10.1016/j.neuron.2015.11.037). URL: <https://doi.org/10.1016/j.neuron.2015.11.037>.

- 2241 Pnevmatikakis, Eftychios et al. (Nov. 2013). “Bayesian spike inference from calcium imaging
2242 data”. In: *Conference Record - Asilomar Conference on Signals, Systems and Computers*.
2243 DOI: [10.1109/ACSSC.2013.6810293](https://doi.org/10.1109/ACSSC.2013.6810293).
- 2244 Pnevmatikakis, Eftychios et al. (Sept. 2014). “A structured matrix factorization framework
2245 for large scale calcium imaging data analysis”. In:
- 2246 Schneidman, Elad et al. (2006). “Weak pairwise correlations imply strongly correlated net-
2247 work states in a neural population”. eng. In: *Nature* 440.7087. 16625187[pmid], pp. 1007–
2248 1012. ISSN: 1476-4687. DOI: [10.1038/nature04701](https://doi.org/10.1038/nature04701). URL: <https://pubmed.ncbi.nlm.nih.gov/16625187>.
- 2249
- 2250 Shannon, C. E. (1948). “A Mathematical Theory of Communication”. In: *Bell System Techni-*
2251 *cal Journal* 27.3, pp. 379–423. DOI: [10.1002/j.1538-7305.1948.tb01338.x](https://doi.org/10.1002/j.1538-7305.1948.tb01338.x).
2252 eprint: <https://onlinelibrary.wiley.com/doi/pdf/10.1002/j.1538-7305.1948.tb01338.x>. URL: <https://onlinelibrary.wiley.com/doi/abs/10.1002/j.1538-7305.1948.tb01338.x>.
- 2253
- 2254
- 2255 Steinmetz, Nick, Matteo Carandini, and Kenneth D. Harris (2019). ”*Single Phase3*” and
2256 ”*Dual Phase3*” *Neuropixels Datasets*. DOI: [10.6084/m9.figshare.7666892.v2](https://doi.org/10.6084/m9.figshare.7666892.v2). URL: https://figshare.com/articles/dataset/_Single_Phase3_Neuropixels_Dataset/7666892/2.
- 2257
- 2258
- 2259 Stringer, Carsen et al. (2019). “Spontaneous behaviors drive multidimensional, brainwide ac-
2260 tivity”. In: *Science* 364.6437. ISSN: 0036-8075. DOI: [10.1126/science.aav7893](https://doi.org/10.1126/science.aav7893).
2261 eprint: <https://science.sciencemag.org/content/364/6437/eaav7893.full.pdf>. URL: <https://science.sciencemag.org/content/364/6437/eaav7893>.
- 2262
- 2263
- 2264 Tada, Mayumi et al. (2014). “A highly sensitive fluorescent indicator dye for calcium imag-
2265 ing of neural activity in vitro and in vivo”. In: *European Journal of Neuroscience* 39.11,
2266 pp. 1720–1728. DOI: [10.1111/ejn.12476](https://doi.org/10.1111/ejn.12476). eprint: <https://onlinelibrary.wiley.com/doi/pdf/10.1111/ejn.12476>. URL: <https://onlinelibrary.wiley.com/doi/abs/10.1111/ejn.12476>.
- 2265
- 2266
- 2267
- 2268
- 2269 Tian, Lin et al. (2009). “Imaging neural activity in worms, flies and mice with improved
2270 GCaMP calcium indicators”. eng. In: *Nature methods* 6.12. 19898485[pmid], pp. 875–
2271 881. ISSN: 1548-7105. DOI: [10.1038/nmeth.1398](https://doi.org/10.1038/nmeth.1398). URL: <https://pubmed.ncbi.nlm.nih.gov/19898485>.
- 2272
- 2273 Tkačík, Gašper et al. (2014). “Searching for collective behavior in a large network of sen-
2274 sory neurons”. eng. In: *PLoS computational biology* 10.1. 24391485[pmid], e1003408–

- 2275 e1003408. ISSN: 1553-7358. DOI: [10.1371/journal.pcbi.1003408](https://doi.org/10.1371/journal.pcbi.1003408). URL:
2276 <https://pubmed.ncbi.nlm.nih.gov/24391485>.
- 2277 Treves, Alessandro and Stefano Panzeri (1995). "The Upward Bias in Measures of Infor-
2278 mation Derived from Limited Data Samples". In: *Neural Computation* 7.2, pp. 399–407.
2279 DOI: [10.1162/neco.1995.7.2.399](https://doi.org/10.1162/neco.1995.7.2.399). eprint: <https://doi.org/10.1162/neco.1995.7.2.399>. URL: <https://doi.org/10.1162/neco.1995.7.2.399>.
- 2280 Vinh, Nguyen Xuan, Julien Epps, and James Bailey (Dec. 2010). "Information Theoretic
2281 Measures for Clusterings Comparison: Variants, Properties, Normalization and Correc-
2282 tion for Chance". In: *J. Mach. Learn. Res.* 11, 2837–2854. ISSN: 1532-4435.
- 2283 Vogelstein, Joshua T. et al. (Oct. 2010). "Fast nonnegative deconvolution for spike train infer-
2284 ence from population calcium imaging". In: *Journal of neurophysiology* 104.6, 295–300.
2285 DOI: [10.1152/jn.01073.2009](https://doi.org/10.1152/jn.01073.2009). URL: <https://doi.org/10.1152/jn.01073.2009>.
- 2286 Wierzynski, Casimir M. et al. ("2009"). ""State-Dependent Spike-Timing Relationships be-
2287 tween Hippocampal and Prefrontal Circuits during Sleep"". In: *"Neuron"* "61"."4", "587
2288 –596". ISSN: "0896-6273". DOI: <https://doi.org/10.1016/j.neuron.2009.01.011>. URL: <http://www.sciencedirect.com/science/article/pii/S0896627309000786>.
- 2289 Zou, Hui and Trevor Hastie (2005). "Regularization and variable selection via the Elastic
2290 Net". In: *Journal of the Royal Statistical Society, Series B* 67, pp. 301–320.